

**Ab initio study of magnetic anisotropy of  
M-type hexaferrite thin films**

Steven Robert Kirk  
S.R.Kirk@physics.org

Submitted for the degree of Doctor of Philosophy  
Institute of Materials Research, Joule Physics Laboratory  
University of Salford

2000

# Contents

<b>1</b>	<b>Introduction</b>	<b>1</b>
<b>2</b>	<b>Synopsis</b>	<b>3</b>
<b>3</b>	<b>Background</b>	<b>5</b>
3.1	Importance of hexaferrite materials in magnetic recording . . .	8
3.2	Production of thin hexaferrite films by pulsed laser deposition	9
<b>4</b>	<b>Magnetism with particular reference to insulating materials</b>	<b>13</b>
4.1	Basic concepts of magnetism . . . . .	13
4.2	Types of magnetic order . . . . .	14
4.2.1	Ferromagnetism . . . . .	15
4.2.2	Antiferromagnetism . . . . .	15
4.2.3	Ferrimagnetism . . . . .	16
4.3	Magnetic anisotropy . . . . .	19
4.3.1	Magnetocrystalline anisotropy . . . . .	20
4.3.2	Shape anisotropy . . . . .	22
4.3.3	Surface anisotropy . . . . .	23
4.3.4	Strain anisotropy . . . . .	24
4.3.5	Induced anisotropy . . . . .	25
<b>5</b>	<b>M-type hexaferrites</b>	<b>26</b>
5.1	Crystal structure . . . . .	26
5.2	Magnetic order and anisotropy . . . . .	30
5.3	Non-stoichiometric variants . . . . .	30

<b>6</b>	<b>Theoretical model of magnetic anisotropy in insulators</b>	<b>32</b>
6.1	Magnetic theory for bulk materials . . . . .	32
6.1.1	Quantum mechanical treatment of magnetism . . . . .	32
6.1.1.1	Energy levels of a free ion. . . . .	32
6.1.1.2	Splitting of energy levels by exchange, spin-orbit coupling and the crystal field . . . . .	32
6.1.1.3	Role of symmetry. . . . .	34
6.1.1.4	Concept of a spin Hamiltonian. . . . .	34
6.1.1.5	Calculation of the energy levels, the partition function, and the single-ion anisotropy using the Wolf procedure . . . . .	38
6.1.1.6	The Superposition Model of the crystal field . . . . .	40
6.1.2	The dipolar contribution to the anisotropy . . . . .	43
6.2	Extension of the magnetic theory for thin films . . . . .	49
6.2.1	Macroscopic expression for magnetic shape anisotropy of a thin film . . . . .	49
6.2.2	Definition and derivation of surface anisotropy . . . . .	50
6.2.3	Other necessary modifications of the bulk theory . . . . .	50
<b>7</b>	<b>Deposition theory</b>	<b>52</b>
7.1	Arrhenius law for surface diffusion . . . . .	52
<b>8</b>	<b>Simulation Techniques and Programs</b>	<b>54</b>
8.1	DEPOSIT - deposition modelling . . . . .	54
8.1.1	Geometrical definition . . . . .	55

8.1.2	Kinetic definition . . . . .	59
8.1.3	Determination of process parameters . . . . .	60
8.1.4	The deposition and growth algorithm . . . . .	61
8.1.5	The DEPOSIT program . . . . .	64
8.2	KFILM - anisotropy simulation . . . . .	65
8.2.1	The ‘mean-field’ model . . . . .	65
8.2.2	Unit cell data file . . . . .	69
8.2.3	Single-ion data file . . . . .	72
8.2.4	Evaluating the single-ion contributions . . . . .	72
8.2.5	Evaluating the dipolar contributions . . . . .	72
8.2.6	Effect of distorted sites and missing ligands . . . . .	73
8.2.7	Summation of anisotropy contributions over all ions in film . . . . .	74
8.3	FILMSTAT - extraction of film statistics . . . . .	74
8.3.1	Film statistics . . . . .	74
8.3.2	Output files for visualisation . . . . .	75
8.3.2.1	Geomview output . . . . .	75
8.3.2.2	Heightfield output . . . . .	77
<b>9</b>	<b>Results</b>	<b>79</b>
9.1	Magnetic anisotropy of the bulk crystal . . . . .	79
9.1.1	Single-ion contribution . . . . .	79
9.1.2	Dipolar contribution with convergence analysis . . . . .	80
9.1.3	Comparison with experimental values . . . . .	81
9.2	Magnetic anisotropy of an infinite perfect film . . . . .	83

9.2.1	Estimate of the magnetic shape anisotropy of a thin film	83
9.2.2	Estimating the dipolar contribution using a ‘tile’ model	83
9.2.2.1	Definition and theory for tile model.	83
9.2.2.2	Implementation, results and conclusion of tile model calculation.	86
9.2.3	Ion-by-ion calculation using KFILM	88
9.2.3.1	Calculation of dipolar anisotropy.	88
9.2.3.2	Calculation of surface anisotropy	89
9.2.3.3	Investigation of the effect of cell cutting	91
9.2.3.3.1	Surface and volume anisotropies of shifted variants	93
9.3	Magnetic anisotropy of a finite perfect film	93
9.4	High-memory vs. low-memory: a comparison of strategies for large-scale anisotropy simulations	100
9.4.1	Discussion of memory issues	100
9.4.2	Single-ion and dipolar strategy comparison	102
9.4.3	Single-ion only strategy comparison	102
9.5	Structural aspects of simulated deposited films	106
9.5.1	Time-related parameters	106
9.5.2	Energy-related parameters	107
9.5.3	Choosing a realistic energy barrier ratio $p$	109
9.5.4	Definition of the three test regimes for anisotropy simulation	111
9.5.5	Time evolution of the growth of the simulated films	112

9.5.5.1	Time evolution of average thickness and roughness . . . . .	113
9.5.5.2	Time evolution of layer coverage . . . . .	113
9.6	Comparison of simulated film with AFM measurements of a real film . . . . .	116
9.6.1	Description of model system, the heightfield output from FILMSTAT, and MATLAB script . . . . .	116
9.6.2	Pictures and description of simulated films . . . . .	119
9.6.3	Picture of experimental AFM data and comparison with simulations . . . . .	119
9.7	Application of the magnetic model to the simulated deposited films . . . . .	123
9.7.1	Methodology . . . . .	123
9.7.2	Magnetic anisotropy of ‘patterned’ films . . . . .	123
9.7.3	Results for volume and surface anisotropies for the three regimes . . . . .	125
<b>10</b>	<b>Discussion of results</b>	<b>132</b>
<b>11</b>	<b>Conclusions</b>	<b>136</b>
11.1	Original achievements and developments in this thesis . . . . .	137
11.2	Suggestions for further work . . . . .	138
<b>A</b>	<b>Crystal structure data for BaM</b>	<b>154</b>
<b>B</b>	<b>Presentations and publications arising from this work</b>	<b>157</b>

C Pseudocode for DEPOSIT program	158
D Pseudocode for KFILM program	160

## List of Figures

3.1	Schematic of the laser ablation deposition process. . . . .	11
4.1	The three main types of magnetic order. . . . .	17
5.1	Perspective view of conventional hexagonal unit cell of $\text{BaFe}_{12}\text{O}_{19}$ . The different Fe sublattices are listed by their Wyckoff symbols and the geometries of their local coordination polyhedra. The relative directions of the atomic spins are also shown. . . . .	27
5.2	The two possible interpretations of the structure of the bipyramidal Fe site;(a) as a single ‘central’ site with full occupancy, or (b) two ‘sub-sites’ , each with half occupancy, spaced equidistantly from the plane of the three equatorial oxygen atoms. The oxygen atoms are shown here as open circles. . . . .	29
6.1	Shapes of the $3d$ atomic orbitals. The orbitals are shown for a magnetic atom at an octahedral site in a crystal, surrounded by six oxygen atoms (open circles). . . . .	35
6.2	Energy level splittings associated with $3d$ ions in octahedral, tetrahedral and trigonal bipyramidal sites. . . . .	36
6.3	Geometrical definition of a system consisting of two interacting magnetic dipoles. . . . .	45
8.1	Model hierarchy . . . . .	56
8.2	The three allowed orientations of the growth units in the plane	57
8.3	‘Geometrical’ and ‘data structure’ representations of the simulation grid. Three growth units, denoted 1,2 & 3 are shown, with different locations and orientations in the simulation grid.	57

8.4	Schematic of the algorithm for choosing the type and site of the next event. . . . .	63
8.5	Excerpt from the initial section of a DEPOSIT film data file. Note the lines recording the ‘process parameters’ for each successive deposition run - these lines record the ‘processing history’ of a simulated deposited film. . . . .	66
8.6	An illustration of an alternative way of regarding the structure of a 2-D infinite lattice. The lower picture shows the infinite lattice, each site having unit occupancy (shown here as black filled circles). Alternatively (upper pictures), the lattice can be regarded as an assembly of independent cells, sites on the boundaries having partial occupancies as shown. . . . .	68
8.7	Example output of Geomview. The structure is that of a simulated grown film produced using DEPOSIT. . . . .	76
9.1	Convergence of the total dipolar contribution to the anisotropy with respect to the dipolar cutoff radius, plotted for the two cases of the Fe cations being at the 2b and 4e positions. Extrapolated values for each of these cases are also shown. . . .	82
9.2	Diagram of the geometry for the case of a square homogeneously magnetized platelet. . . . .	84
9.3	Fitted values of $K_D/K$ vs. $1/(\text{number of tiles } N)$ . . . . .	87
9.4	Dipolar contributions to the anisotropy as a function of the reciprocal of the cutoff radius for a number of different thicknesses of film. . . . .	90

9.5	Volume and surface contributions to the total anisotropy for a perfect crystalline thin film. . . . .	92
9.6	Dependence of the dipolar and single-ion anisotropy contributions on the position of the slicing plane for a 1-layer thick film. . . . .	94
9.7	Single-ion surface and volume anisotropy contributions for a number of shifted variants of the unit cell . . . . .	95
9.8	Dipolar anisotropy contributions for a finite slab and a range of slab thicknesses . . . . .	97
9.9	Individual and total anisotropy contributions over a range of slab thicknesses . . . . .	98
9.10	Execution time vs. system size for two computation schemes with differing memory requirements for the total anisotropy. .	103
9.11	Execution time vs. system size for two computation schemes with differing memory requirements for the single-ion contribution only. . . . .	104
9.12	Geometry for evaluation of barrier energies $E_{aa}$ and $E_{cc}$ . . . .	107
9.13	Variation of number of hopping/reorientation events with energy barrier ratio $p$ . . . . .	110
9.14	Ratio of average film thickness to number of monolayers deposited as a function of deposition time for a range of values of deposition flux $F_{dep}$ . Results are averaged over 300 runs except where indicated. . . . .	114

9.15	Average roughness as a function of average thickness for a range of values of deposition flux $F_{dep}$ . Results are averaged over 300 runs except where indicated. . . . .	115
9.16	Time evolution of layer coverages for ‘granular’ test case . . .	117
9.17	Time evolution of layer coverages for ‘smoother’ test case . .	118
9.18	3D view of heightfield corresponding to ‘granular’ test case . .	120
9.19	3D view of heightfield corresponding to ‘smoother’ test case .	121
9.20	3D view of heightfield data produced from AFM measurements of an M-type hexaferrite film grown using PLD techniques. .	122
9.21	Repeating units for ‘stripe’ and ‘chessboard’ patterns. . . .	124
9.22	Surface and volume anisotropies for ‘granular’ test case . . . .	126
9.23	Surface and volume anisotropies for ‘granular2’ test case . . .	127
9.24	Surface and volume anisotropies for ‘smoother’ test case . . .	128
9.25	Surface and volume anisotropies for ‘smoother2’ test case . .	129
9.26	Surface and volume anisotropies for ‘perfect’ test case . . . .	130

## List of Tables

5.1	Notation, coordination number and the magnetic moment of $\text{Fe}^{3+}$ cations in the elementary cell of $\text{BaFe}_{12}\text{O}_{19}$ . . . . .	28
6.1	Fitting parameters for the distance dependance of the $b_2^0$ spin Hamiltonian parameter for $\text{BaFe}_{12}\text{O}_{19}$ . . . . .	43
9.1	Single-ion contributions to the anisotropy from the five sublattices. . . . .	80
9.2	Calculated magnetic anisotropy contributions for bulk. . . . .	81
9.3	Anisotropy contributions and total anisotropy for two different surface patterns for a simulated film of average thickness 1.5 monolayers. The anisotropy values are given in units of $10^5 \text{ Jm}^{-3}$ . . . . .	124
9.4	Volume anisotropy for the three test cases in units of $10^5 \text{ Jm}^{-3}$ . . . . .	125
9.5	Extrapolated values for $1/(\text{thickness}) \rightarrow 0$ of the single-ion contribution to the surface anisotropy for the three test cases in units of $10^{-5} \text{ Jm}^{-2}$ . . . . .	131
10.1	Summary of <i>ab initio</i> calculated anisotropy contributions for perfect and simulated grown films of $\text{BaFe}_{12}\text{O}_{19}$ at $T=0\text{K}$ . Unless otherwise indicated, the results are shown for the bipyramidal Fe cations being in the 2b positions and the 12k sites on the corners of the unit cell. . . . .	133

## Acknowledgements

- Professor Richard Gerber, for acting as my supervisor for this project, for invaluable theoretical discussions and also providing me with additional funding when conventional sources ran out.
- Dr. Pavel Novak (Institute of Physics, Charles University, Prague, Czech Republic) for his advice and guidance both during and after my visit to the Institute. Also Prof. Zdenek Šimša and his group, for their hospitality.
- Samantha, for inspiration, advice and patience.
- Professor John A. Venables (CPES, University of Sussex and Arizona State University, USA) for his advice on thin film growth modelling and access to his vast store of thin-film related literature.
- Dr Ian Morrison, Department of Physics, University of Salford, for the use of the IBM SP2 system ‘dirac’ for almost all of my calculations.
- All of the staff, technicians and security staff at Salford University.
- The software authors who make their creations (easily the equal of, and often superior to, commercially produced software) freely available on the Internet.

## Abstract

Ferrites are a broad class of oxide materials with a wide range of technologically important applications. The M-type hexaferrites, of which  $\text{BaFe}_{12}\text{O}_{19}$  is taken as a prototype compound, show particular promise as very high density magnetic and magneto-optical data storage media. There are still serious gaps in the understanding of the fundamental origins of, and mechanisms governing, the magnetic properties of these materials. The detailed relationships between these properties and the material structure over nanometre length scales are also not fully understood. This thesis addresses both of these pressing issues. It describes first a detailed *ab initio* theoretical treatment of the origins and magnitudes of the two most important mechanisms which give rise to magnetic anisotropy, namely dipolar interactions and single-ion contributions. The thesis outlines the theory of these two types of magnetic interactions in solid insulating oxide materials. It also describes the theory of the deposition and growth of thin films, and the implementation of both branches of this theoretical study in a set of original computer programs developed and refined during this study, comprising tools for both calculation and visualization. A novel growth model and efficient Monte Carlo techniques are used to investigate and quantify the dependence on growth conditions of the structure of thin films of hexaferrite materials. The magnetic theory is also implemented in a flexible and powerful program, which is used in turn to comprehensively investigate the structural dependence of magnetic properties in the bulk crystalline material, idealized thin films, and finally by the simulated grown films. The influence of film structure on volume and surface contributions to the anisotropy of thin films is thereby quantified and discussed.

# 1 Introduction

Ferrites are a broad class of oxide materials with a number of technologically important applications. They have been used extensively in the construction of microwave devices, but have also become very important in recent years as magnetic recording media. One of the most promising sub-classes of the ferrites for the latter application is the M-type hexagonal ferrites [1]. In spite of having been studied since the 1950s and their potential for technological applications, there are still serious gaps in knowledge regarding the origins and magnitudes of the magnetic anisotropy exhibited by this class of materials. In particular, there has been very little fundamental *ab initio* investigation of their magnetic properties.

This thesis addresses these gaps by describing the *ab initio* calculation of the magnetic anisotropy of the prototype M-type ferrite  $\text{BaFe}_{12}\text{O}_{19}$ . The analysis performed is equally applicable to other M-type ferrites, and commences with an examination of the bulk material, focussing on *ab initio* evaluations of the intrinsic contributions to the anisotropy from two candidate physical mechanisms, namely single-ion anisotropy and dipole-dipole anisotropy. The calculated values are compared with, and complement, the results of experimental measurement. Precise experimental evaluation of the anisotropy is difficult - most values tabulated in the literature have been derived from measurements of magnetic hysteresis loops, rather than more direct and accurate torque-based measurements. In this way the thesis stands as a useful and timely complement to the existing body of experimental knowledge.

In addition, the thesis also addresses the problem of the theoretical investigation of magnetic anisotropy in thin films of these materials, a field which has little or no pre-existing representation in the literature and which has direct and timely relevance to existing and proposed technological applications. Combined with a novel model for the deposition and growth of ferrite thin films developed in parallel with the magnetic investigations, the interplay between the structure and the magnetic anisotropy of thin ferrite films is elucidated using the same powerful *ab initio* techniques developed for treatment of the bulk material. The results of these comprehensive studies are then presented and discussed, along with ideas for future development.

The SI Kennelly system of magnetic units will be used in this thesis. The magnetization  $M$  used in the SI Sommerfeld convention will also be used - this is just an alternative way of stating the intensity of magnetization  $I$ , using the relation  $I = \mu_0 M$  [2].

## 2 Synopsis

This work is concerned with the investigation of two fundamental aspects of thin-film hexaferrite media.

The first of these is the *ab initio* calculation of the contributions to the uniaxial magnetic anisotropy of both bulk samples and thin films arising from two different microscopic mechanisms - the single-ion contribution and the dipole-dipole interaction.

It has long been known [3] that hexaferrite materials have a very strong uniaxial magnetic anisotropy. This has been attributed largely to the presence of a short-range ‘single-ion’ mechanism, in which each magnetic ion contributes additively to the anisotropy, the contribution from each ion depending on the geometry of its immediate atomic environment, with particularly strong contributions coming from the bipyramidal 2b(4e) sites (see later). These ‘single-ion’ contributions have been calculated by applying the superposition model [4] to bulk material structures and then for the first time also to those of thin films.

Furthermore, each ion with non-zero spin in the material can also be considered as having an associated magnetic dipole moment. By treating these dipoles as being effectively classical point dipoles, the anisotropy contribution of the long-range dipole-dipole interaction was evaluated using a ‘complete’ summation procedure, allowing the evaluation of the dipolar anisotropy of both isolated nanoscale particles and, using appropriately applied periodic boundary conditions, continuous thin films and the bulk material.

The second aspect of this work concerns the modelling of the deposition

and growth of thin hexaferrite films, with particular attention to the effects of the growth conditions on the morphology of the grown film. This was achieved by applying an efficient Monte Carlo algorithm to a novel growth model for hexagonal materials, which allows for both an in-plane orientational degree of freedom and for the presence of voids in the growing film. The effects of the growth parameters on the morphology of the simulated film have been examined.

Finally, these two aspects of the work have been united, by using the output of the growth simulations as the input for the calculation of the uniaxial magnetic anisotropy of barium ferrite thin films, as described above. In this way, the magnetic characteristics of the simulated films have been related to their physical growth conditions. This holds out the prospect of tailoring a film with well-defined magnetic characteristics by a careful control choice of growth conditions to produce the desired microstructure. The magnetic anisotropy of a number of such ‘grown’ films has been calculated as a function of their thickness using the methods described above, and the results compared to those for perfect uniformly oriented single-crystal films. Particular attention was paid to the dependence of the surface anisotropy associated with the films on their surface topography.

### 3 Background

The first magnetic recording device (the ‘Telegraphone’) was invented by Danish scientist Valdemar Poulsen in 1898 [5]. A century of development has seen great advances: magnetic recording is one of the key technologies which have fuelled the explosive development of information technology. In parallel with the rapid advances achieved in computer power using developments in semiconductor technology and very large scale integration, the capacity and speed of data storage devices based on magnetic recording technologies have continued to rise, offering an extremely reliable high-density information storage medium at a cost which is approaching that of paper. The vast majority of the data currently stored in electronic form is held on devices using magnetic storage techniques, and the future markets for all forms of magnetic recording are expected to grow substantially as areal storage densities (i.e. the amount of data stored per unit surface area of the storage medium) increase by orders of magnitude, and data rates and access times also improve.

One of the key challenges faced by the developers of magnetic storage devices is to increase the areal storage density of magnetic recording media. After spectacular growth in the last four decades, the industry has recently reached one of its long-sought goals of 10 Gb/in<sup>2</sup>, and devices meeting this specification are now reaching production. Reaching the next major goal, that of 100 Gb/in<sup>2</sup>, will require a far-reaching rethink as to how magnetic recording is done.

Much research effort is now being focussed on the development of record-

ing media based on thin films of magnetic materials. Thin films are inherently denser than traditional magnetic media based on dispersions of magnetic particles, and so can be made to have the highest possible magnetization (to give adequate signal voltages in the sensors by which the information is read from the medium) whilst remaining extremely thin, a property which allows the transitions between the magnetic domains recorded on the medium to be as sharp as possible [6].

Much attention is now being concentrated on the development of *perpendicular magnetic recording* [7, 8, 9, 10]. This technique, like conventional (or *longitudinal*) recording, relies on the ability to ‘write’ very small magnetic domains on the recording medium. The difference lies in the direction of the magnetization in the pattern of domains. In longitudinal recording, magnetic domains are formed which have their magnetization lying in the plane of the recording medium. In perpendicular recording, the magnetic domains are formed such that their magnetization is parallel (or antiparallel) to the normal to the surface of the thin film medium. The smaller magnetic interactions between the latter type of domains means that they can be packed more closely together before the demagnetizing effect of neighbouring oppositely magnetized domains causes significant destabilization.

Another fundamental problem is that of *superparamagnetism* [11] - the thermal destabilization of a magnetic domain when the magnetic energy stored in the domain becomes comparable to the thermal energy in the material. The probability of a magnetic domain undergoing a spontaneous change in the direction of its magnetization is proportional to  $\exp(-KV/k_B T)$ ,

where  $k_B$  is the Boltzmann factor,  $T$  is the absolute temperature,  $V$  is the volume of the domain and  $K$  is the uniaxial magnetic anisotropy of the material in which the domain exists. The effects of superparamagnetism can be minimised in perpendicular recording media, since domains can extend through the entire thickness of the film, allowing  $V$  to be kept reasonably large whilst simultaneously allowing the domain to become smaller in the plane of the film. Such domains may therefore be packed more closely together than is possible with longitudinal recording techniques.

The microstructure of the recording medium also plays a crucial part in determining its magnetic properties. Inside a domain, the magnetic moments are strongly coupled to each other by short-range exchange forces (see later) whose magnitude depends strongly on local atomic order. Practical magnetic recording media are polycrystalline, and the local atomic order is strongly disrupted at the boundaries between grains - the greater the local disorder, the less the exchange coupling between neighbouring grains. The magnetic state of one grain is then less likely to affect the magnetic states of neighbouring grains, a situation which again allows magnetic domains to be packed more closely together. Decreased inter-grain exchange coupling also has favourable effects on the signal-to-noise ratio obtainable in practical recording systems [12, 13, 14, 15, 16, 17].

These factors, taken together, suggest that an ideal microstructure for a high-density perpendicular recording medium consists of closely packed, magnetically decoupled ‘columns’ which extend through the entire thickness of the film medium. The study of how to achieve this microstructure

through careful choice of film growth methods, film substrate materials and the physical parameters controlling the film growth process is therefore of major importance to the magnetic recording industry.

### **3.1 Importance of hexaferrite materials in magnetic recording**

M-type hexaferrite materials have been advanced as candidates for perpendicular magnetic recording media [18, 19, 20, 21, 22], based on a number of criteria, outlined below.

**High uniaxial anisotropy.** M-type ferrites have a very strong intrinsic uniaxial anisotropy, reducing the destabilizing effects of superparamagnetism and magnetostatic interactions between neighbouring domains.

**Chemical stability.** Hexaferrite media are chemically inert. This can be contrasted with widely-used rare-earth/transition metal alloy media e.g. GdTbCo and TbFeCo, which are susceptible to corrosion and hence require protective overlayers to protect against attack from even common atmospheric chemical species.

**Mechanical stability and tribological properties.** Hexaferrite media are extremely hard and wear-resistant, allowing long media lifetimes. In addition, they can be made extremely smooth, eliminating the need for lubricating overlayers. The distance between the recording head and the recording medium can therefore be reduced, which allows smaller domains to be written, increasing the areal data density.

## 3.2 Production of thin hexaferrite films by pulsed laser deposition

A very important method for the production of thin films of semiconductors and oxide materials is Laser Ablation Deposition (LAD). The possibility of using lasers to deposit thin films has been known for over three decades [23], but the technique only became widespread with the advent of high- $T_c$  superconductors, when it was found that the technique could produce high-quality films of stoichiometric composition of such materials [24]. In this method, the desired film material is ablated from a target of stoichiometric composition by a powerful laser which is focussed onto a small spot on the target surface, giving energy flux densities of the order of  $10^8 W cm^{-2}$ . The energy flux from the laser is absorbed by the surface layers of the target, causing the structure of the material to be explosively disrupted in a region around the impact point of the beam. The ablated material, consisting of a mixture of neutral and ionized species, is ejected from the target in a plume normal to the target surface. This plume of ablated material then impinges on a substrate (usually a few centimetres from the target) to form the desired film (see Figure 3.1). The process is carried out in an enclosed chamber under varying degrees of low partial pressures of oxygen and other gases, the laser beam entering the chamber through a (usually quartz) window. Continuous lasers have been used, but a more common variant of the process involves pulsed lasers (Pulsed Laser Deposition or PLD). The equipment requirements of this technique are therefore modest, and the fact that multi-component targets

can be used and the material stoichiometry is preserved gives a substantial advantage over other deposition techniques. The latter may require multiple single-component targets, which may all have different vapour pressures and hence evaporation rates, requiring a much more complicated deposition apparatus. Despite these advantages, deposition using lasers has not yet been widely adopted commercially, but it remains an extremely useful laboratory-scale method for depositing thin films of a very wide range of materials.

The best type of laser to use varies with the target material, and is largely determined by the thermal constants of the material and the laser wavelength. For the ferrite materials discussed in this thesis, an excimer UV ( $\lambda = 248$  nm) laser gives better results [25] (a deposited film with a specular surface and a low level of particulate contamination) than a Nd:YAG ( $\lambda = 1.06 \mu$  m) laser. This has been attributed to the ferrite having a greater absorption at UV than at infrared wavelengths, so that the energy is absorbed in a shallow region in the outermost layers of the target. By contrast, the infrared energy from the Nd:YAG laser is absorbed less efficiently, and hence a much deeper region under the surface is affected. As the explosive decomposition then takes place deeper into the target, undisassociated particles and molten droplets of the outermost surface layers can be thrown into the plume. This process, known as ‘splashing’, causes the deposited film to contain particulates, spoiling the uniformity and the surface of the films which is rather important for their applications. The effect can often be all but eliminated, however, by polishing the target, rotating the target during deposition and using an off-axis deposition geometry [26].

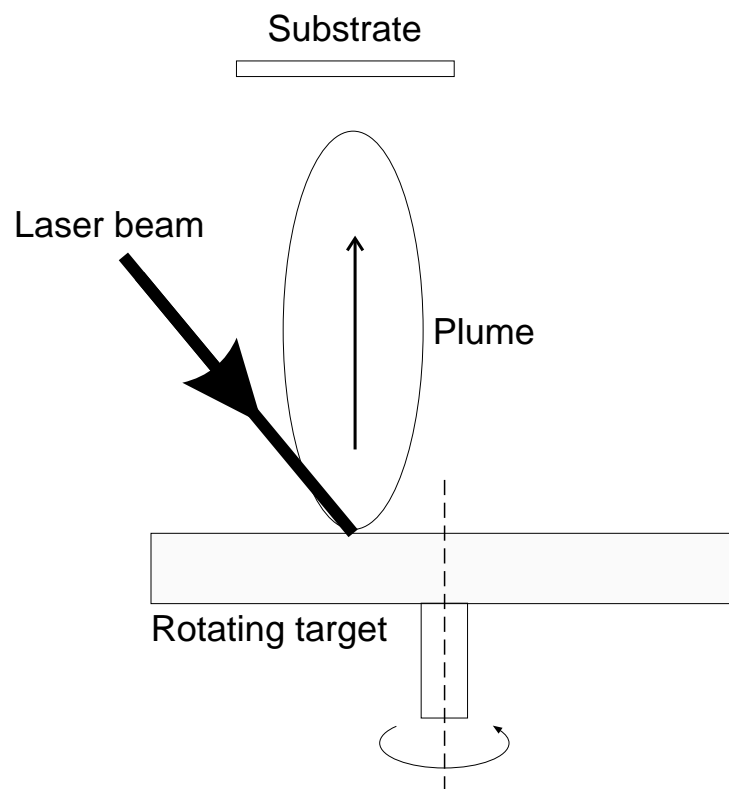


Figure 3.1: Schematic of the laser ablation deposition process.

High-quality films of M-type hexaferrite materials have been grown using PLD [27, 28, 29, 30, 31, 32, 33]. In the first of these references, the substrate used was the (0001) face of sapphire ( $Al_2O_3$ ). Using a substrate temperature of 840° C and introducing a slight partial pressure (0.1 mbar) of oxygen into the deposition chamber yielded films of stoichiometric composition which were very strongly c-axis oriented.

## 4 Magnetism with particular reference to insulating materials

### 4.1 Basic concepts of magnetism

Magnetism is caused by the motion of carriers of electric charge. In solid materials, these charge carriers may be free to move throughout the material (e.g., electrons in metals) or they may be localized (e.g. around an atom in insulating materials), depending on the nature of the material and its temperature. In the case of insulating materials, e.g., most metal oxides and ferrites, the electrons, being predominantly confined to the regions surrounding the atoms making up the material, are counterbalanced by the formation of ions. Depending on the detailed electronic structure of an ion, it may possess an effective magnetic dipole moment, arising from the orbital and intrinsic spin angular momenta of the electrons. This dipole moment will depend on the detailed interactions between the angular momenta of all of the electrons associated with the ion, the intrinsic spin momenta of these electrons, and interactions between one electron and another, whether on the same ion or a neighbouring ion.

If a magnetic dipole  $\mathbf{m}$  is placed in a uniform magnetic field  $\mathbf{H}$ , the potential energy,  $E$ , of the dipole is given by the scalar product

$$E = -\mathbf{m} \cdot \mathbf{H}. \quad (4.1)$$

The magnetization  $\mathbf{M}$  of an assembly of  $N$  colinear magnetic dipoles is defined

[34] as the net magnetic moment per unit volume. When the dipoles are not colinear, the component of the mean magnetization in the  $j$  direction is given by

$$\mathbf{M}_j = \frac{1}{V} \sum_{i=1}^N \mathbf{m}_i \cdot \mathbf{e}_j, \quad j = x, y, z \quad (4.2)$$

where  $V$  is the volume occupied by the assembly,  $\mathbf{m}_i$  is the magnetic moment associated with the  $i$  th dipole and  $\mathbf{e}_j$  is a unit vector in the  $j$  direction.

A related quantity, the *intensity of magnetization*  $\mathbf{I}$  is used in the SI Kennelly convention for magnetic units [2]. It is defined by

$$\mathbf{I} = \mu_0 \mathbf{M}. \quad (4.3)$$

## 4.2 Types of magnetic order

The degree of magnetic order in a magnetic insulator may be discussed in terms of the relative alignments of the overall angular momentum vectors associated with a set of points in the structure, usually the magnetic atom sites. It is conventional to refer to these points by their associated spin (even though the orbital angular momentum may also contribute). Each point therefore may be considered to have an associated magnetic moment, which is taken to be a local property of that point. Exchange interactions act between these localized spins (either directly or via an intervening atom) in such a way that the spins become colinear at zero temperature. The magnetic order can then be classified according to the relative magnitude, number and orientations of the spins.

### 4.2.1 Ferromagnetism

Ferromagnetic materials are characterized by having one unique type of spin site, with all of the magnetic moments on the sites equal in magnitude and parallel to each other at zero temperature (see Figure 4.1). These materials therefore have their maximum magnetization when  $T = 0K$ , and the magnetization falls to zero at a certain critical temperature  $T_C$  (the *Curie temperature*) which is determined by the composition of the material. Ferromagnetic insulators are relatively rare (EuS being an example).

### 4.2.2 Antiferromagnetism

In antiferromagnetic materials there are only two sublattices, on which the moments are antiparallel and equal in magnitude. There is therefore no net magnetization at zero temperature, but there is a critical temperature  $T_N$  (the *Néel temperature*) above which the sublattice moments no longer cancel each other out and take random directions. This critical point exhibits itself as a kink in the graph of magnetic susceptibility vs. temperature. Antiferromagnetic insulators are much more common than ferromagnetic insulators - most simple oxides of transition metals are antiferromagnetic. In these materials, the magnetic moments associated with the metal cations interact strongly with each other via the mechanism of indirect exchange or *superexchange*, acting via the  $p$ -orbitals of the intervening  $O^{2-}$  ion. The effective exchange coupling is strongly dependent on the Me-O-Me (Me = metal) angle, and is strongest when this angle is  $180^\circ$  (e.g., [35] for further information and references). One example of an antiferromagnetic substance

is the mineral goethite ( $\alpha$ -Fe<sub>2</sub>O<sub>3</sub>).

### 4.2.3 Ferrimagnetism

In ferrimagnetic materials, there may be more than one type of spin site, possibly with different numbers of sites of each type. All of the sites of any given type are said to make up a *sublattice*. The magnetic moments associated with the sublattices are either parallel or antiparallel to each other at zero temperature, but do not all have equal magnitudes (see Figure 4.1). These substances therefore have a net magnetization at zero temperature. Antiferromagnetism may also then be regarded as a special case of the more general phenomenon of ferrimagnetism.

The magnetic properties of ferrimagnetic substances can show a very wide variety of temperature dependences, since the temperature dependences associated with the different sublattices can be very different, and can act to reinforce or oppose each other. In particular, ferrimagnetic substances may have *two* critical temperatures at which the magnetization falls to zero - as the temperature passes through the lower of these (the so-called *compensation* temperature  $T_{\text{comp}}$ ), the net magnetization of the substance falls to zero and then changes direction. This property is particularly useful when these materials are used in magneto-optical recording devices. Heating the material locally to near its compensation temperature using a laser allows the magnetic state of a very small region of the recording medium to be ‘flipped’ using an externally applied magnetic field, a fact which allows very small magnetic domains to be written on the recording medium. The magnetiza-

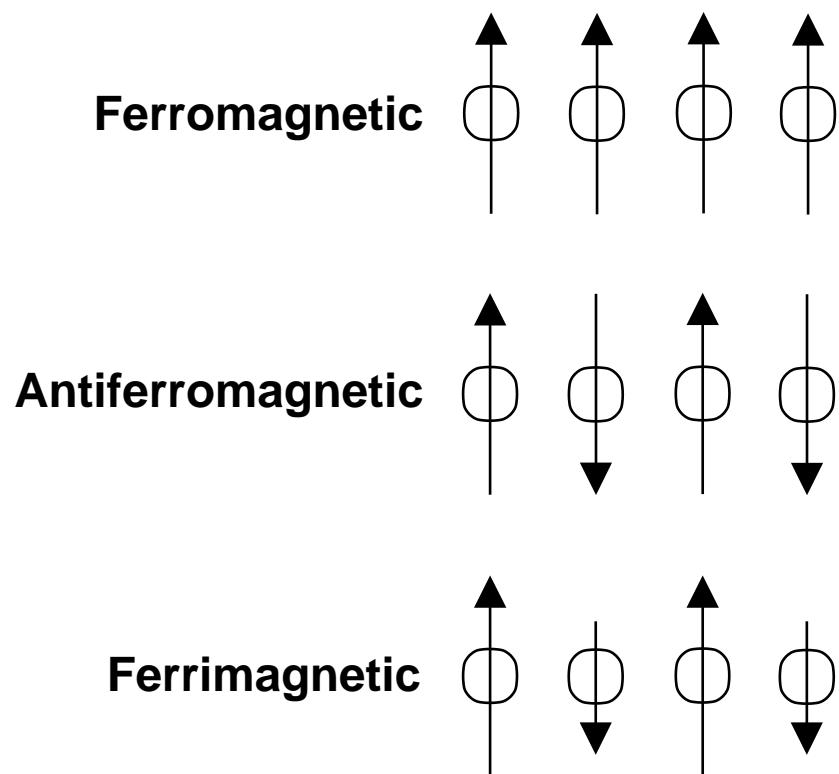


Figure 4.1: The three main types of magnetic order.

tion distribution in ferrimagnets can be very complex, since the presence of a number of geometrically distinct sublattices can generate a very wide variety of superexchange interactions. The most important ferrimagnets from the point of view of magnetic recording are rare-earth garnets (the most widely investigated being gadolinium gallium garnet ['GGG']) and hexagonal ferrites, such as the M-type hexaferrites which are the subject of this thesis.

### 4.3 Magnetic anisotropy

A body is said to possess magnetic anisotropy if it has a net magnetization (either intrinsic or induced by an external magnetic field) and the free energy associated with the body depends on the direction of the magnetization with respect to some body-fixed axes. The preferred directions for the magnetization will be those which minimize the free energy of the system (so-called ‘easy’ directions). If the magnetization is to lie in any other direction, energy must be supplied from outside the system. The so-called ‘hard’ directions are those for which this additional energy requirement is a maximum.

Magnetic anisotropies are usually stated in terms of the angular dependence of the free energy per unit volume, expressed in terms of functions of the angles between the direction of magnetization and the body-fixed axes. In crystalline materials the body-fixed axes are usually taken to be the crystallographic axes. The functions used to describe the angular dependence can take a number of forms, usually chosen for mathematical simplicity, but also largely based on historical and experimental precedent. A number of attempts have been made to advocate the adoption of sets of *orthogonal* angular functions for the description of magnetic anisotropies (e.g. [36]). These descriptions, in principle superior to all others, have been all but ignored by most of the magnetism community. This is partly because of the vast amount of experimental data already in existence using the traditional schemes, and partly because most experiments seem to require only two or three terms under the traditional schemes to fit experimental data to within the limits of reliable measurement. The exception seems to be in the description of sur-

face and interface anisotropies - Néel’s original paper on surface anisotropy [37] used orthogonal Legendre polynomials, and more recent work (e.g. [38]) has continued in this tradition. The latter paper also contains a prescription for transforming a traditional set of *anisotropy constants* (shown in the next section) into a set of *anisotropy coefficients* for use with Legendre polynomials. In this thesis, however, the traditional forms of the angular functions, which may be derived through symmetry operations [35], will be used.

#### 4.3.1 Magnetocrystalline anisotropy

Magnetocrystalline anisotropy is that part of the magnetic anisotropy which depends on the microscopic properties of the magnetic ions in their crystal lattice sites. We can imagine a non-magnetic host crystal, into which magnetic ions are substituted for non-magnetic ions, perhaps by some doping process. Different mechanisms for the magnetic anisotropy will become important as the concentration of magnetic ions is increased. These mechanisms are outlined below.

- Single-ion contributions

Each magnetic ion may contribute a ‘single-ion’ anisotropy to the overall anisotropy which expresses the dependence of the free energy of the ion on the relative orientation of its overall magnetic moment. This type of anisotropy is characterised by a linear dependence of the measured anisotropy on the concentration of magnetic ions, and can be considered to exist across the entire possible range of concentrations.

- Collective contributions

The aforementioned dependence of the measured anisotropy on the concentration of magnetic ions becomes non-linear at all but low concentrations, as contributions from collective interactions between ions begin to have a substantial effect. One such interaction is the dipolar interaction. In an assembly of classical magnetic dipoles, any particular dipole may be considered to sit in an effective magnetic field which is the vector sum of contributions from the dipolar fields created by all the other dipoles in the assembly. Another mechanism which is particularly important in magnetic alloys is exchange anisotropy, caused by the existence of preferred local atomic ordering patterns between neighbouring different metal atoms (see, e.g. [35]).

In cubic materials, the free energy per unit volume may be stated as [34, 35]

$$F = F_0 + K_1(\alpha_1^2\alpha_2^2 + \alpha_2^2\alpha_3^2 + \alpha_3^2\alpha_1^2) + K_2\alpha_1^2\alpha_2^2\alpha_3^2 + \dots \quad (4.4)$$

where  $\alpha_{1,2,3}$  are the direction cosines of magnetization relative to the cubic crystallographic axes and  $K_i$  are the cubic anisotropy constants, with  $F_0$  being the part of the free energy which is independent of the direction of the magnetization. In materials having a hexagonal crystal structure, the corresponding expression is [35]

$$F = F_0 + K_{u1}\sin^2\theta + K_{u2}\sin^4\theta + K_{u3}\sin^6\theta + K_3^*\sin^6\theta\cos^6\psi + \dots \quad (4.5)$$

where  $\theta$  and  $\psi$  are respectively the polar and azimuthal angles of magnetization relative to the hexagonal axes. The expressions above contain only even powers of the angular functions due to the requirement that the free energy be invariant under time-reversal symmetry.

### 4.3.2 Shape anisotropy

The shape of a magnetic sample is an important (extrinsic) source of magnetic anisotropy. If a particle is non-spherical, and in the absence of other stronger anisotropy effects, the magnetization will tend to lie along the longest axis of the sample. This behaviour is due to the fact that a strongly magnetic (ferromagnetic or ferrimagnetic) finite sample will have uncompensated magnetic ‘poles’ on its surface. The ‘poles’ create a demagnetizing field which opposes the magnetization of the sample. In ellipsoidal specimens, the demagnetizing field  $H_d$  is given by

$$H_d = -N_d I / \mu_0 \quad (4.6)$$

where  $I$  is the intensity of magnetization and  $N_d$  is a parameter known as the *demagnetizing factor* or *shape factor*. This (dimensionless) quantity is anisotropic since it depends on the direction in which the magnetization is measured and also on the exact shape of the sample. In addition, the demagnetizing field is only constant inside a sample when its shape is an ellipsoid of revolution. General formulae exist for  $N_d$  (e.g. in [35, 39]) given the lengths of the principal axes of the ellipsoid. In the case of an infinite flat plate which is magnetized perpendicularly to its wide surface, the demagnetizing factor

$N_d = 1$ . The demagnetizing field therefore strongly opposes the magnetization being perpendicular to the plate, and will cause the magnetization to rotate into the plane of the plate unless opposed by other stronger anisotropy mechanisms. This situation is particularly relevant in the case of thin films. By contrast, a thin needle-like specimen magnetized along its length will experience a negligible demagnetizing field, and hence in this case  $N_d \approx 0$ . Consequently, for an ellipsoid of revolution, the shape anisotropy energy can be expressed [34] as

$$F = \frac{1}{2}(N_B - N_A)I^2 \sin^2(\theta) \quad (4.7)$$

where  $N_B$  and  $N_A$  are the demagnetizing factors along the short and long principal axes of the ellipsoid respectively, and  $\theta$  is the angle between the magnetization intensity  $I$  and the long ellipsoid axis.

### 4.3.3 Surface anisotropy

On or near a surface, the local environment of an atom is different from that deep inside the bulk material, giving rise to an effective magnetic surface anisotropy. This fact was first noted and examined by Néel [37]. The degree to which the presence of the surface will affect the overall anisotropy contribution from a given atom or atoms will depend on the relative sizes of the distances from the atom or atoms to the surface and the length scales of the different types of magnetic interaction. Lattice distortions due to relaxation of the structure close to the surface may also contribute to this effect.

#### 4.3.4 Strain anisotropy

Strain anisotropy arises from the phenomenon of *magnetostriction* (where the dimensions of a magnetic material change with its magnetization). Conversely, the magnetization of a magnetic sample can change as a result of being subjected to strain (the *magnetomechanical* effect), which may be either externally applied or arise from inclusions, defects in the crystal lattice, or lattice mismatch at interfaces, such as the boundary between a thin film and a substrate. The magnetostriction  $\lambda$  of a sample is given by [35]

$$\lambda = \frac{\Delta l}{l} \quad (4.8)$$

where  $\Delta l$  is the change in length induced in a sample of original length  $l$ . When magnetostriction is isotropic, the energy stored in a sample due to magnetostrictive strain (the *magnetoelastic energy*,  $E_{me}$ ) is given by

$$E_{me} = \frac{3}{2} \lambda_S \sigma \sin^2 \theta \quad (4.9)$$

where  $\lambda_S$  is the value of  $\lambda$  at magnetic saturation,  $\sigma$  is the applied stress and  $\theta$  is the angle between the applied stress and the direction of magnetization. Comparing Equations (4.9) and (4.5), we can therefore define a stress anisotropy constant

$$K_\sigma = \frac{3}{2} \lambda_S \sigma. \quad (4.10)$$

If  $K_\sigma$  is positive, the stress axis is an easy direction of magnetization, while if  $K_\sigma$  is negative the plane normal to the stress direction is an easy plane of magnetization.

#### **4.3.5 Induced anisotropy**

The magnetic anisotropy of a substance may also be affected by mechanical processing, and by the thermal history of the sample. This type of anisotropy is usually referred to as induced anisotropy, and it can play a small part (usually no more than a few percent) in determining the overall anisotropy of the sample. An overview of some different types of induced anisotropy is given by Chikazumi ([35]).

## 5 M-type hexaferrites

### 5.1 Crystal structure

The M-type hexaferrites are ferrimagnetic materials whose chemical composition can be represented by the general formula  $MFe_{12}O_{19}$  ( $\equiv MO \cdot 6Fe_2O_3$ ), where M represents a large divalent cation such as  $Ba^{2+}$ ,  $Sr^{2+}$  or  $Pb^{2+}$ . When  $M = Pb^{2+}$ , the structure corresponds to that of the natural mineral magnetoplumbite [40]. The conventional unit cell is hexagonal ( $\alpha = \beta = 90^\circ, \gamma = 120^\circ$ ), and a number of structural studies exist in the literature [41, 42] (note, however that the description given in [41] is in error, a fact pointed out and corrected in [43]). For this study we have used the structural data given by [42], which gives the lattice parameters as  $a = b = 5.892 \text{ \AA}$ ,  $c = 23.182 \text{ \AA}$ .

The conventional unit cell is shown in Figure 5.1, comprising 2 formula units, with space group  $P6_3/mmc$ . The structure may be regarded as consisting of close-packed layers of  $O^{2-}$  ions with Fe ions in some of the interstices of the oxygen lattice (a more detailed description may be found in [43]).

There are five symmetry-nonequivalent Fe sublattices (as shown in Figure 5.1 and listed in Table 5.1), in three different types of oxygen coordination polyhedron : tetrahedral, octahedral and a trigonal bipyramid. The trigonal bipyramidal site (see Figure 5.2) has been given two different classifications by experimental studies: either 2b (with the Fe ion in the same plane as the equatorial oxygen atoms) or 4e (with the Fe ion effectively being split into two sites, each with half occupancy and equidistant from the plane of

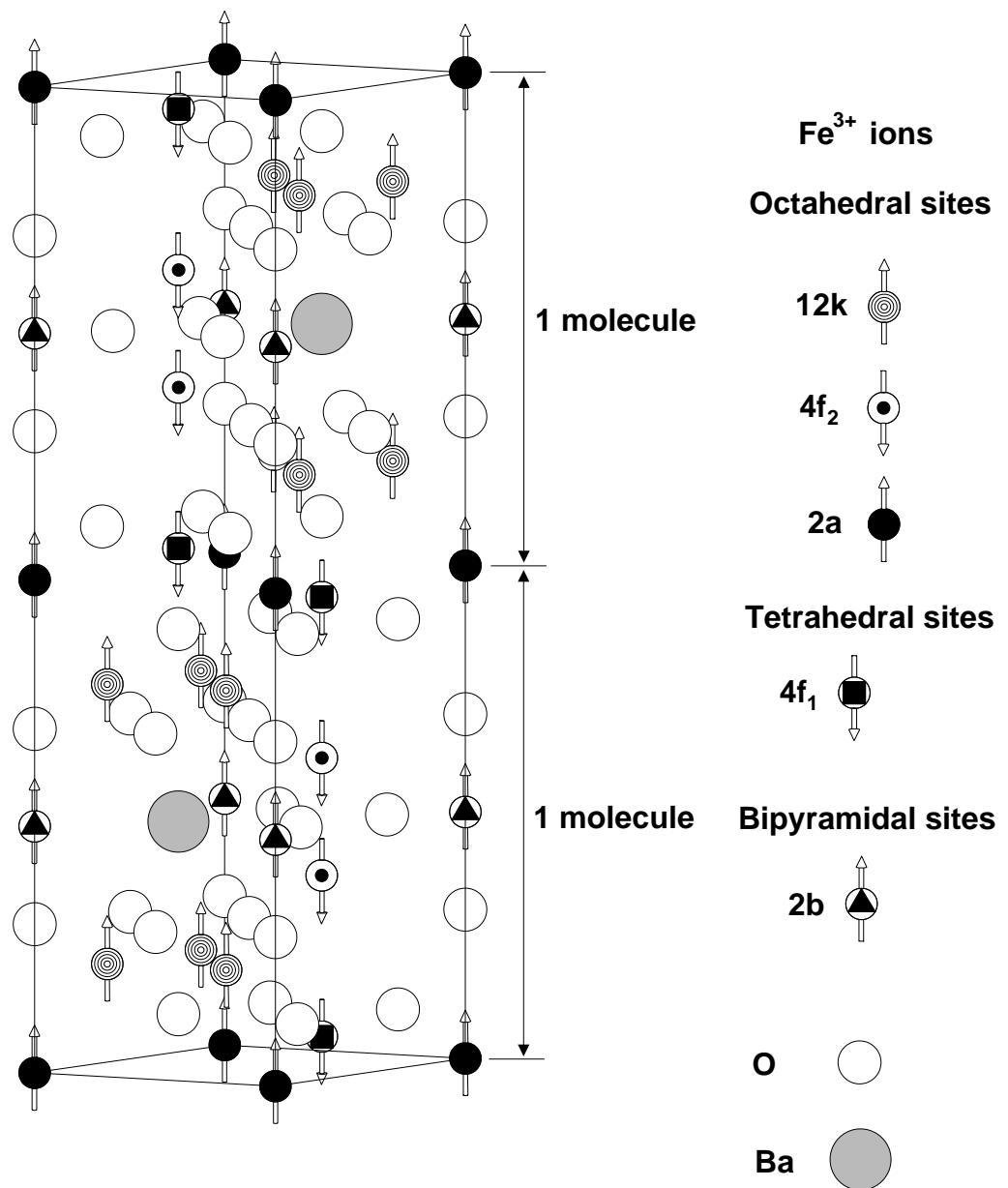


Figure 5.1: Perspective view of conventional hexagonal unit cell of BaFe<sub>12</sub>O<sub>19</sub>. The different Fe sublattices are listed by their Wyckoff symbols and the geometries of their local coordination polyhedra. The relative directions of the atomic spins are also shown.

Number of positions	Wyckoff's notation	Coordination number	Type of site	Magnetic moment per formula unit
12	k	6	octahedral	6 $\uparrow$
4	f2	6	octahedral	2 $\downarrow$
4	f1	4	tetrahedral	2 $\downarrow$
2	a	6	octahedral	1 $\uparrow$
2	b	5	bipyramidal	1 $\uparrow$

Table 5.1: Notation, coordination number and the magnetic moment of  $\text{Fe}^{3+}$  cations in the elementary cell of  $\text{BaFe}_{12}\text{O}_{19}$ .

the equatorial oxygen atoms). A careful experimental study [42] has shown that the latter arrangement is correct, with the Fe ion on each bipyramidal site effectively ‘frozen’ randomly (with equal probability) in either the ‘up’ or ‘down’ position below  $T=70\text{K}$ , and dynamically disordered (each ion effectively spending half its time in each position) above this temperature. This study also puts the distance of each ‘sub-site’ from the equatorial plane at  $0.17 \text{ \AA}$ . If both such sites in the conventional unit cell are in the same position (‘up’ or ‘down’), then the inversion symmetry of the unit cell is lost, so that the space group becomes  $P6_322$ .

The structure may also be described using the notation  $RSR^*S^*$  describing the stacking sequence in the unit cell. The letters  $R$  and  $S$  denote structural sub-units, where the  $R$  blocks consists of everything in and between the close-packed oxygen layers immediately adjacent to the plane of the M atoms, and the  $S$  blocks consist of Fe and O atoms in a spinel structure.

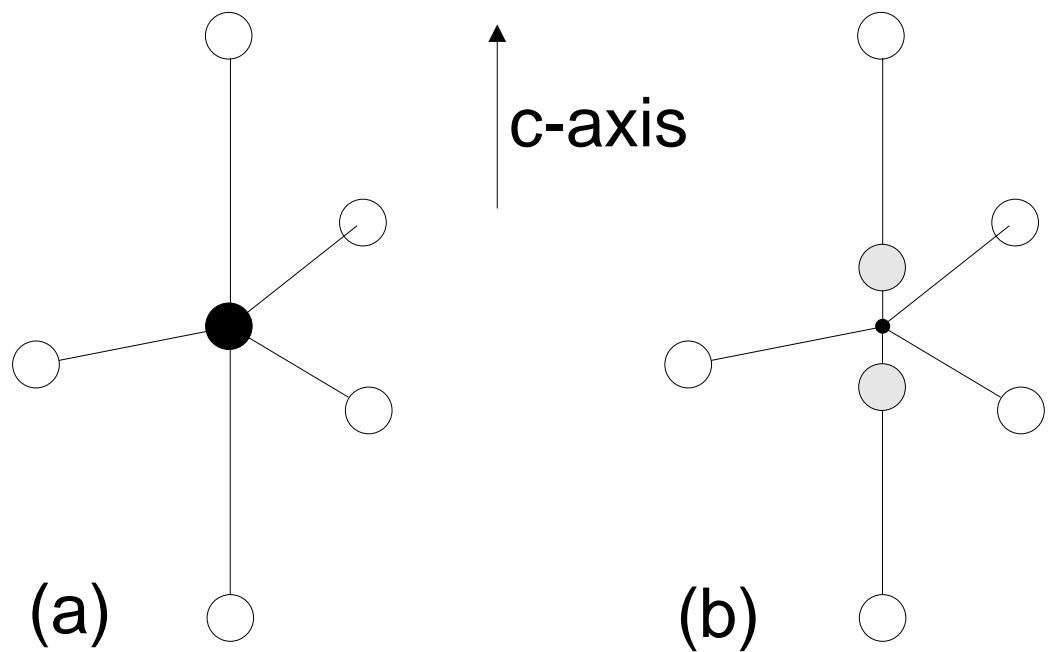


Figure 5.2: The two possible interpretations of the structure of the bipyramidal Fe site; (a) as a single ‘central’ site with full occupancy, or (b) two ‘sub-sites’, each with half occupancy, spaced equidistantly from the plane of the three equatorial oxygen atoms. The oxygen atoms are shown here as open circles.

The asterisk is used to denote the fact that the block in question is rotated through  $180^\circ$  about the *c*-axis with respect to its un-asterisked counterpart. This ‘layered’ arrangement has important consequences for the ease of formation of the overall structure - recent work [44] has shown that because the bonding between the  $M^{2+}$  ion and its surrounding oxygen ions is an order of magnitude weaker than that between the  $Fe^{2+}$  ions and the oxygens, the  $M^{2+}$  ion exhibits high mobility through the *R* and *R\** layers.

## 5.2 Magnetic order and anisotropy

The Fe ions are all nominally in the  $Fe^{3+}$  charge state, and at  $T=0K$  all of the spins (corresponding to  $S=5/2$ ) are colinear with the *c*-axis of the crystal structure, which is also the ‘easy’ axis for the overall uniaxial magnetic anisotropy. Cubic contributions to the overall anisotropy are negligible, since the individual cubic contributions of the octahedral sites cancel each other out. The distribution of ‘up’ and ‘down’ spins was first proposed by Gorter [45], and is shown in Figure 5.1. The nominal net magnetization per unit cell at  $T=0K$  is  $20 \mu_B$ , where  $\mu_B$  is the Bohr magneton. This value is very close to those found by experiments [46, 47].

## 5.3 Non-stoichiometric variants

Much research has been carried out on M-type hexaferrites which have had some of their Fe ions replaced by single trivalent ions such as Al ([48, 49]), Ga ([48, 50]), In ([50]) and Sc ([50]). Also, ferrites in which equal numbers of  $Co^{2+}$  and  $Ti^{2+}$  have been substituted for pairs of Fe ions have been extensively

studied ([51, 52, 53]) due to their particularly advantageous magneto-optical properties. Other studied substitutions include non-stoichiometric (Ni-Zr) [54] and [Ir-Me; Me=Co, Zn] [55] - many other studies are referenced in [1].

## 6 Theoretical model of magnetic anisotropy in insulators

### 6.1 Magnetic theory for bulk materials

#### 6.1.1 Quantum mechanical treatment of magnetism

**6.1.1.1 Energy levels of a free ion.** The electronic configuration of the  $\text{Fe}^{3+}$  ion is  $[\text{Ar}] (3d^5)$ , i.e. equivalent to that of an argon atom with 5 additional valence electrons in the 3d shell. The 3d orbitals ( $n=3, l=2$ ) are degenerate in the free ion and in the absence of an external magnetic field, except for the zero-field splitting, giving an effective ground state of  ${}^6\text{S}_{5/2}$ . The shapes of the 3d wavefunctions are shown in Figure 6.1.

**6.1.1.2 Splitting of energy levels by exchange, spin-orbit coupling and the crystal field** In a crystal, the electron wavefunctions associated with the ion will be modified from their free-ion forms, along with their energy levels. The dominant effect will be that of exchange, acting between atomic spins. The part of the Hamiltonian of the system associated with exchange may be written in the conventional form due to Heisenberg [56]:

$$H_{ex} = 2 \sum_{i < j} J_{ij} \mathbf{S}_i \cdot \mathbf{S}_j \quad (6.1)$$

This effect, however, is to all intents and purposes spherically symmetric for  ${}^6\text{S}_{5/2}$  ions. The energy levels will be shifted from their free-ion values by the effects of exchange, but there will be no additional splitting created

between the levels. Exchange therefore plays no part in determining the single-ion anisotropy [57, 58].

The presence of nearby atoms also removes the spherical symmetry of the free ion and hence alters the relative energy associated with states with different orbital angular momentum (assuming L-S coupling). The spin on each ion can then ‘feel’ the effect of the local atomic environment through the mechanism of spin-orbit coupling, which is usually taken to have a contribution to the overall Hamiltonian of the form

$$H_{so} = \lambda_{so}(L \cdot S) \quad (6.2)$$

where  $\lambda_{so}$  is the *spin-orbit coupling constant*, and  $L$  and  $S$  are the total orbital and spin angular momenta respectively. The overall effect on the spin can be thought of as being that of a ‘crystal field’ created by the surrounding atoms. In early work [59] this crystal field was taken to be a purely electrostatic phenomenon, but it is now known that many mechanisms contribute to the crystal field effect, most importantly the overlap of atomic wavefunctions and covalency effects [60].

In the 3d transition metals, the magnitudes of the energies associated with the exchange ( $E_{ex}$ ), spin-orbit coupling ( $E_{so}$ ) and the crystal field ( $E_{cf}$ ) follow the order:

$$E_{ex} > E_{cf} > E_{so} \quad (6.3)$$

This is generally referred to [61] as the *intermediate* crystal field case. In order to obtain an expression for the energy levels in the presence of the crystal fields and spin-orbit coupling, perturbation theory must be used. Although

the total angular momentum  $L$  for a free S-state ion is zero ('quenched'), and hence from (6.2) spin-orbit coupling might be expected to have no effect on the splitting of the energy levels, it does appear as a non-zero second-order term in the perturbation expansion [61, 62, 63].

**6.1.1.3 Role of symmetry.** The local symmetry of the Fe site plays a crucial role in determining the relative energy and multiplicity of the energy levels [34, 35, 61]. For a  $\text{Fe}^{3+}$  ion in an octahedral site (i.e. surrounded by six oxygen ions - see Figure 6.1), the energy levels are split into a doublet ( $d_{x^2-y^2}$  and  $d_{z^2}$ ) and a triplet ( $d_{xy}$ ,  $d_{xz}$  and  $d_{yz}$ ) with the doublet being higher in energy. This pattern may be understood using the observation that the electron clouds associated with the  $d_{xy}$ ,  $d_{xz}$  and  $d_{yz}$  orbitals are directed 'between' the neighbouring oxygen ions, whereas the  $d_{x^2-y^2}$  and  $d_{z^2}$  orbitals are directed towards neighbouring oxygen ions - the latter orbitals will have a higher energy due to the greater electrostatic repulsion from the oxygen ions. The relative positions of the doublet and triplet are reversed if the site has tetrahedral symmetry (see Figure 6.2). In the case of the trigonal bipyramidal site in BaM, the energy levels are similar to those for the tetrahedral site, except that the  $d_{z^2}$  orbital is lowered in energy relative to the upper doublet due to the fact that the apical oxygen atoms (i.e. those lying in the c-direction) are substantially further away from the ion than the equatorial oxygen atoms [25, 64].

**6.1.1.4 Concept of a spin Hamiltonian.** Rather than write the full Hamiltonian in terms of all of the five valence electron spins, because the

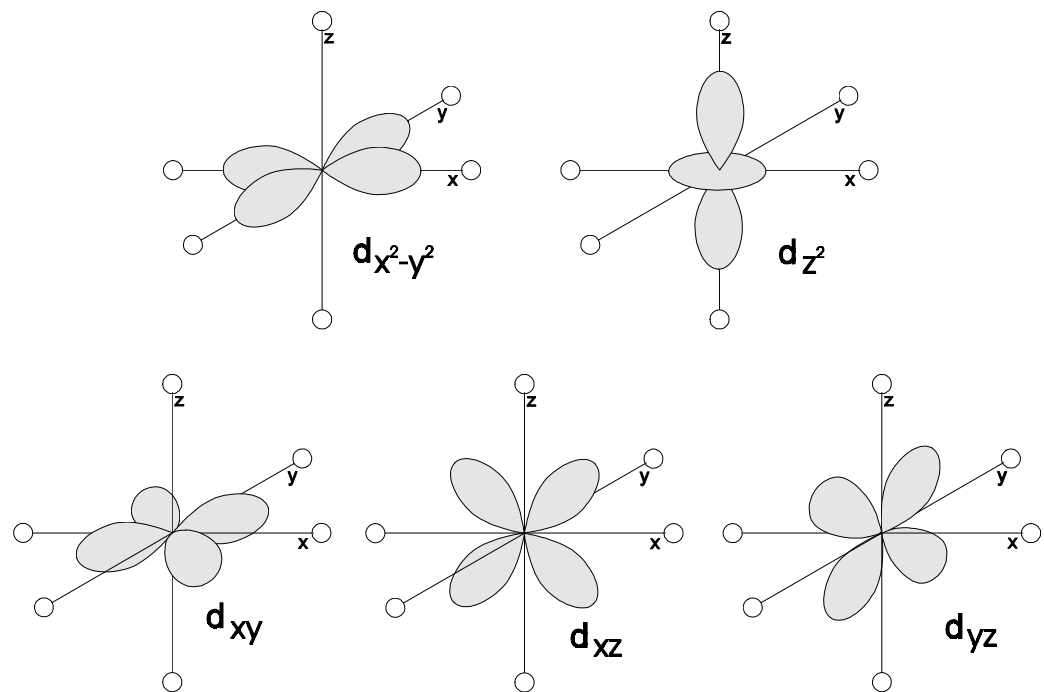


Figure 6.1: Shapes of the  $3d$  atomic orbitals [34]. The orbitals are shown for a magnetic atom at an octahedral site in a crystal, surrounded by six oxygen atoms (open circles).

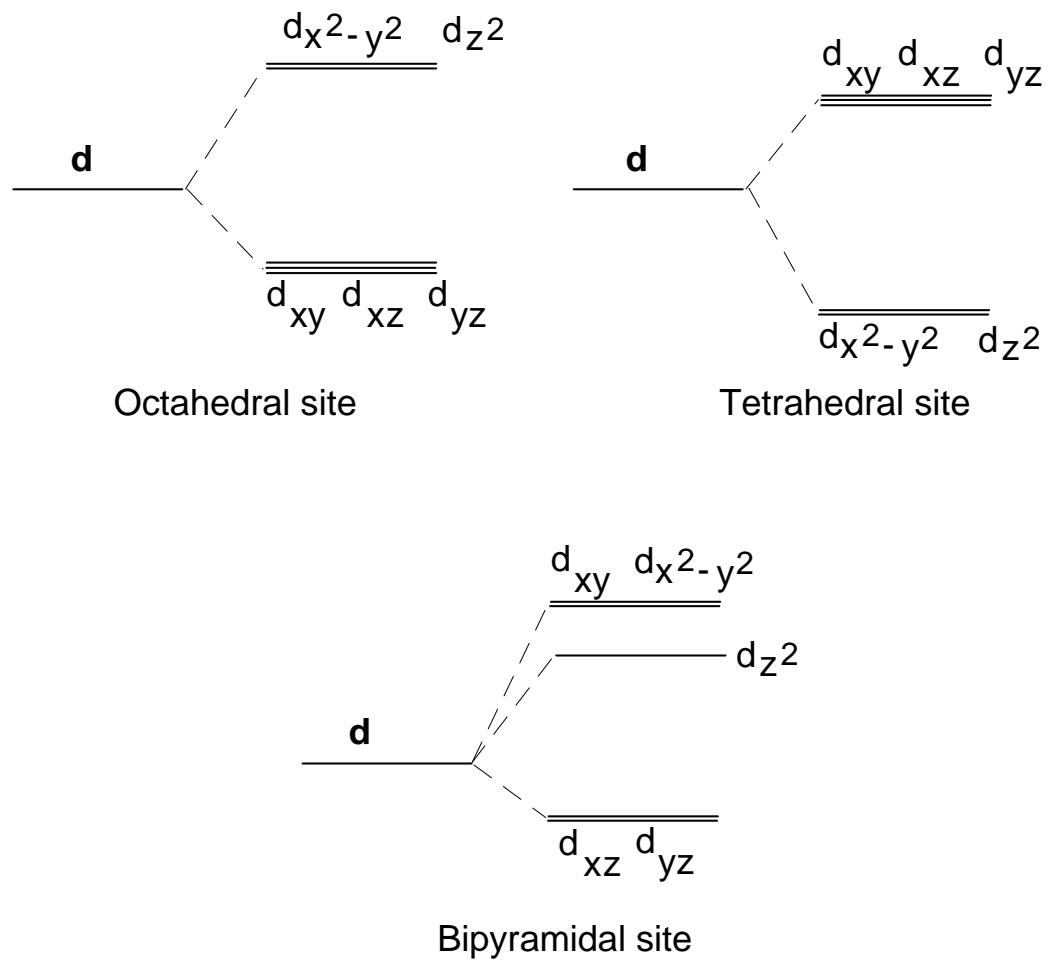


Figure 6.2: Energy level splittings associated with  $3d$  ions in octahedral, tetrahedral and trigonal bipyramidal sites.

Fe ion is effectively in its ground state with all spins parallel and the energy gap between the ground state and the first excited state is large compared with the small splitting, we can assign an effective spin  $S' = 5/2$  to the ion as a whole. This allows us to use a much simpler *spin Hamiltonian* [65, 66] to describe the ion energy levels. All of the following discussion uses this effective spin, and in order to simplify the notation, the prime signifying the effective nature of the spin will be dropped.

The single-ion part of the spin Hamiltonian used to describe the Fe ions is given by

$$H_{si} = DS_z^2 + \dots \quad (6.4)$$

where only the term corresponding to uniaxial anisotropy has been shown,  $D$  being a constant and  $S'_z$  being the projection of the effective spin in the uniaxial direction. An alternative way to state the spin Hamiltonian is as an expansion in so-called extended Stevens operators [67, 68]

$$\begin{aligned} H &= \sum_{kq} B_k^q O_k^q(S_x, S_y, S_z) \\ &= \sum_{kq} f_k b_k^q O_k^q(S_x, S_y, S_z) \end{aligned} \quad (6.5)$$

where the  $B_k^q, b_k^q$  and  $f_k$  are constants,  $O_k^q$  are operators as tabulated in [69], and the  $f_k$  take values of  $1/3$ ,  $1/60$  and  $1/1260$  for  $k = 2, 4$ , and  $6$  respectively. It may therefore be seen from (6.4) and (6.5) that

$$D = 3B_2^0 = b_2^0. \quad (6.6)$$

The history of the conventions and notations used to describe spin Hamiltonians (particularly with respect to their experimental determination using

electron paramagnetic resonance experiments) has been very confused, a fact which has greatly hindered the development of a single unified treatment of the subject. A very comprehensive review article has been written by Rudowicz [69] clarifying and correcting the misapprehensions and notational inconsistencies prevalent in the existing (vast) body of published literature on the subject. Rudowicz has also made substantial progress in the development of a systematic scheme for tabulating spin Hamiltonian coefficients, a consistent notation and a computer program for standardization of old experimental data [70, 71]. It is hoped that this formalism will become the standard in future studies.

**6.1.1.5 Calculation of the energy levels, the partition function, and the single-ion anisotropy using the Wolf procedure** Wolf [72] expressed the general spin Hamiltonian for a spin  $S \leq 5/2$  on a site of approximately cubic symmetry as

$$H = \beta \mathbf{H} \cdot g \cdot \mathbf{S} + \frac{1}{6} a (S_x^4 + S_y^4 + S_z^4) + D S_\alpha^2 + f S_\alpha^4. \quad (6.7)$$

where  $\mathbf{H}$  is the effective magnetic field at the site,  $g$  is the gyromagnetic ratio,  $\beta$  is the Bohr magneton and  $a$  and  $D$  are constants quantifying the cubic and uniaxial components of the spin Hamiltonian respectively. The deviation from cubic symmetry is assumed to be axial (along an arbitrary distortion direction denoted by the subscript  $\alpha$ ) and quantified using the constant  $f$ . This Hamiltonian, after diagonalization, gives the following energy levels for

$S = 5/2$  [61]:

$$E_{\pm 5/2} = \pm \frac{5}{2}g\beta H_{eff} + \frac{1}{2}a(1 - 5\phi) + \frac{5}{3}D(3 \cos^2 \theta - 1) \quad (6.8)$$

$$\pm \frac{D^2}{4g\beta H_{eff}} [5 + 70 \cos^2 \theta - 75 \cos^4 \theta]$$

$$E_{\pm 3/2} = \pm \frac{3}{2}g\beta H_{eff} - \frac{3}{2}a(1 - 5\phi) - \frac{1}{3}D(3 \cos^2 \theta - 1) \quad (6.9)$$

$$\pm \frac{D^2}{4g\beta H_{eff}} [9 - 66 \cos^2 \theta + 57 \cos^4 \theta]$$

$$E_{\pm 1/2} = \pm \frac{1}{2}g\beta H_{eff} + a(1 - 5\phi) - \frac{4}{3}D(3 \cos^2 \theta - 1) \quad (6.10)$$

$$\pm \frac{D^2}{4g\beta H_{eff}} [4 - 40 \cos^2 \theta + 36 \cos^4 \theta]$$

where the effective field  $H_{eff}$  makes a direction  $(l, m, n)$  with the cubic axes and an angle  $\theta$  with the distortion direction  $\alpha$ , and where  $\phi = l^2m^2 + m^2n^2 + n^2l^2$ . These expressions are only true provided  $a < D \ll g\beta H_{eff}$ , as is true in our case.

Once the expressions for the  $i$  energy levels  $E_i$  have been arrived at, one can calculate the thermodynamic partition function  $Z$ , defined by

$$Z = \sum_{i=1}^{N_{levels}} \exp\left(\frac{-E_i}{k_B T}\right). \quad (6.11)$$

for a single ion, where  $k_B$  is the Boltzmann constant and  $T$  is the temperature.

The partition function is related to the free energy  $F$  by the equation

$$F = -k_B T \ln Z. \quad (6.12)$$

If we therefore expand Equation (6.12) using the definition of  $Z$  and the expressions (6.8), (6.9), (6.10) for the energy levels containing the crystal field

parameters, and retaining only leading terms, we arrive at the expression

$$F = F_0(y) + D \cos^2 \theta p(y) + \text{terms in } \cos^4 \theta \quad (6.13)$$

where

$$y = \exp(-g\beta H_{eff}/kT), \quad (6.14)$$

$$p(y) = (1/Z_0)(5 - y - 4y^2 - 4y^3 - y^4 + 5y^5), \quad (6.15)$$

$$Z_0 = 1 + y + y^2 + y^3 + y^4 + y^5. \quad (6.16)$$

Considering only anisotropic terms, Equation (6.13) may then be compared directly with Equation (4.5). It may be seen that the first uniaxial anisotropy constant of a structure containing  $N_{sub}$  sublattices can be written as

$$K = \sum_i^{N_{sub}} N_i D_i p_i(y_i) \quad (6.17)$$

where the  $i$ th sublattice contains  $N_i$  ions. At  $T=0K$ , this simplifies to

$$K = 5 \sum_i^{N_{sub}} N_i D_i \quad (6.18)$$

**6.1.1.6 The Superposition Model of the crystal field** The Superposition Model (SM) of the crystal field [73, 74] is based on four postulates:

1. The crystal field acting on the open-shell electrons of a paramagnetic ion is the resultant of a sum of contributions coming from individual ions in the crystal.

2. Only contributions from the neighbouring ions (commonly referred to as *ligands*) are taken into account.
3. Each single-ion contribution in the sum is axially symmetric about the line joining its centre to that of the paramagnetic ion.
4. Single-ligand contributions are dependent only on the nature of the ligand and its distance from the paramagnetic ion, and do not depend on other properties of the host crystal.

Using the superposition model, therefore, the parameters  $b_n^m$  of the spin Hamiltonian (6.5) may be written as a sum over contributions from  $N$  ligands thus:

$$b_n^m = \sum_{i=1}^N b_n(r_i) Z_n^m(\mathbf{r}_i) \quad (6.19)$$

where  $\mathbf{r}_i \equiv (x_i, y_i, z_i)$  is the position vector joining the magnetic ion to the  $i$ th ligand ion, the  $b_n$  are so-called *intrinsic* parameters which depend only on the type of ligand and the ion-ligand distance  $r_i$ , and the functions  $Z_n^m$  are functions only of the orientation of the ligand (which are tabulated in [73]), e.g.

$$Z_2^0 = \frac{1}{2} \left( \frac{3z_i^2}{r_i^2} - 1 \right) \quad (6.20)$$

$$Z_2^2 = \frac{3}{2} \left( \frac{x_i^2}{r_i^2} - \frac{y_i^2}{r_i^2} \right). \quad (6.21)$$

By separating off the geometrical dependence in this way, the spin Hamiltonian parameters may be calculated for a site with arbitrary geometry. The functions  $b_n(r)$  are determined by comparing known values of the spin Hamiltonian parameters in different systems and/or by analysing their dependence

on pressure. The values are assumed to decrease with increasing  $r$ , and are usually fitted to a function of the form

$$b_n(r) = b_n(r_0) \left( \frac{r_0}{r} \right)^{t_n} \quad (6.22)$$

where  $r_0$  and  $t_n$  are used as the fitting parameters. Novak and Vosika [75] measured and analysed the electron paramagnetic resonance spectra of  $\text{Fe}^{3+}$  ions in a number of garnets and found quantitatively different dependences for octahedrally- and tetrahedrally-coordinated  $\text{Fe}^{3+}$  ions in these compounds, although their results showed considerable scatter. A more recent study by Yeung [76] used experimental results from a larger number of compounds, as well as experiments made under hydrostatic pressure. In his analysis, Yeung also made allowances for local deformation around the  $\text{Fe}^{3+}$  ions and proposed a universal dependence for all types of sites, which has the form of Equation (6.22) with the parameters given in Table 6.1. In a later paper [4] Novak compared the parameters of Yeung's universal dependence and those obtained from his earlier paper [75] when applied to the determination of the single-ion contribution to the uniaxial magnetic anisotropy of  $\text{BaFe}_{12}\text{O}_{19}$ . He found that these two sets of parameters gave broadly similar dependences, but neither could account for the single-ion contribution from the  $2b$  bipyramidal site. Noticing that the Fe-O and O-O distances for the three equatorial Fe-O ligands around the bipyramidal site were small compared with other types of sites (and with the apical Fe-O distances on the same site), he suggested a modified set of parameters (also given in Table 6.1) which specifically apply to the equatorial Fe-O ligands on the bipyramidal site. The parameter values specified in Table 6.1 have therefore been adopted for all of the

	$r_0$ (Å)	$b_2(r_0)$ (cm <sup>-1</sup> )	$t_2$
Yeung's 'universal' dependance	2.0	-0.1552	14.4
Novak's suggested modified parameters for equatorial $2b$ Fe-O ligands	2.0	0.4600	14.4

Table 6.1: Fitting parameters for the distance dependance of the  $b_2^0$  spin Hamiltonian parameter for BaFe<sub>12</sub>O<sub>19</sub>.

following single-ion anisotropy calculations described in this thesis.

Further details of the implementation and the algorithm used may be found in Section 8.2.4, and the results of calculations may be found in Section 9.

### 6.1.2 The dipolar contribution to the anisotropy

The potential energy of a magnetic dipole  $\mathbf{m}_i$  in the magnetic field created by another dipole  $\mathbf{m}_j$  separated from the first by a displacement  $\mathbf{r}_{ij} = r_{ij} \hat{\mathbf{r}}_{ij}$ , where  $r_{ij} = |\mathbf{r}_{ij}|$ , may be written [35] as

$$U_{ij} = \frac{1}{4\pi\mu_0 r_{ij}^3} [\mathbf{m}_i \cdot \mathbf{m}_j - 3(\mathbf{m}_i \cdot \hat{\mathbf{r}}_{ij})(\mathbf{m}_j \cdot \hat{\mathbf{r}}_{ij})]. \quad (6.23)$$

If  $\mathbf{m}_i$  and  $\mathbf{m}_j$  are colinear, then they may be written as  $\mathbf{m}_i = s_i \mathbf{m}$  and  $\mathbf{m}_j = s_j \mathbf{m}$ , where  $s_i, s_j = \pm 1$ . By also writing  $\hat{\mathbf{m}} = \mathbf{m}/m$ , where  $m = |\mathbf{m}|$ ,

Equation (6.23) can be further simplified to

$$U_{ij} = \frac{3s_i s_j m^2}{4\pi\mu_0 r_{ij}^3} \left[ \frac{1}{3} - (\hat{\mathbf{m}} \cdot \hat{\mathbf{r}}_{ij})^2 \right] \quad (6.24)$$

Using the angles defined in Figure 6.3, we can write

$$\hat{\mathbf{m}} = [\sin \theta \cos \phi, \sin \theta \sin \phi, \cos \theta], \quad (6.25)$$

$$\hat{\mathbf{r}}_{ij} = [\sin \theta_{ij} \cos \phi_{ij}, \sin \theta_{ij} \sin \phi_{ij}, \cos \theta_{ij}], \quad (6.26)$$

and hence

$$\begin{aligned} (\hat{\mathbf{m}} \cdot \hat{\mathbf{r}}_{ij})^2 &= \sin^2 \theta \cos^2 \phi \sin^2 \theta_{ij} \cos^2 \phi_{ij} & (6.27) \\ &+ \sin^2 \theta \sin^2 \phi \sin^2 \theta_{ij} \sin^2 \phi_{ij} \\ &+ \cos^2 \theta \cos^2 \theta_{ij} \\ &+ 2 \sin^2 \theta \sin \phi \cos \phi \sin^2 \theta_{ij} \sin \phi_{ij} \cos \phi_{ij} \\ &+ 2 \sin \theta \cos \theta \cos \phi \sin \theta_{ij} \cos \theta_{ij} \cos \phi_{ij} \\ &+ 2 \sin \theta \cos \theta \sin \phi \sin \theta_{ij} \cos \theta_{ij} \sin \phi_{ij}. \end{aligned}$$

The total dipolar energy associated with a system of  $N$  dipoles is given by:

$$U = \frac{1}{2} \sum_{\substack{i,j \\ i \neq j}}^N U_{ij} \quad (6.28)$$

where the factor of 1/2 is introduced to avoid counting the interaction between dipoles  $i$  and  $j$  twice. If we consider that the  $N$  dipoles making up the system are distributed throughout a sphere of material of radius  $R$ , then the dipole anisotropy energy density  $E$  in the sphere may be written as:

$$E = \lim_{R \rightarrow \infty} \frac{3U}{4\pi R^3}. \quad (6.29)$$

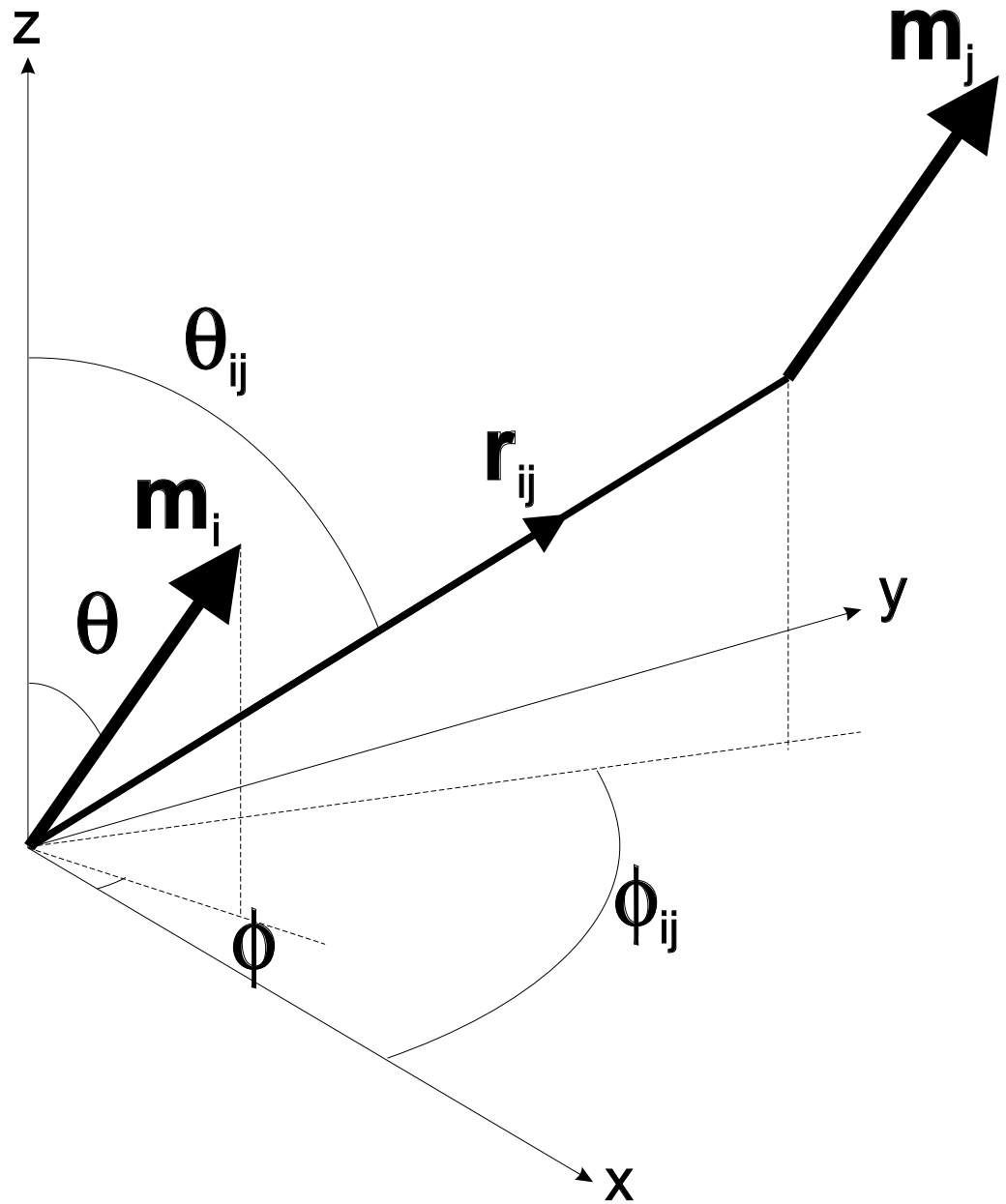


Figure 6.3: Geometrical definition of a system consisting of two interacting magnetic dipoles.

In order to make a ‘complete’ summation for  $E$  computationally feasible, it is necessary to make some approximations. The first is to reduce the number of arithmetic operations needed from  $O(N^2)$  to  $O(N)$  by reducing the first summation from a sum over all  $N$  dipoles to the product of a sum over the  $n$  dipoles enclosed in the volume of a unit cell of the material  $V_u$  and the number of unit cells in the sphere, thus

$$U' = \frac{1}{2} \cdot \frac{4\pi R^3}{3V_u} \sum_i^n \sum_j^N U_{ij} \quad (6.30)$$

with the added condition that

$$R \gg \sqrt[3]{V_u}. \quad (6.31)$$

Substituting (6.30) for  $U$  in (6.29), Equation (6.29) may then be approximated as

$$E' = \lim_{R \rightarrow \infty} \frac{1}{2V_u} \sum_i^n \sum_j^N U_{ij}. \quad (6.32)$$

We chose to place our representative unit cell at the centre of the sphere, while in reality it may be anywhere in the sphere. We can justify this choice by observing that the error in Equation (6.30) is proportional to the ratio of the number of unit cells lying on the surface of the sphere to the number within the sphere, and this ratio drops off as  $1/R$  as  $R \rightarrow \infty$ . The second approximation replaces the infinite limit of  $R$  with a finite cutoff radius  $R_c$  which is chosen such that increasing  $R_c$  does not lead a significant change in the calculated value of  $E''$ , where

$$E'' = \frac{1}{2V_u} \sum_{i \in V_u}^n \sum_{\substack{j, \\ r_{ij} < R_c}} U_{ij} \quad (6.33)$$

and  $r_{ij}$  is the distance between dipoles  $i$  and  $j$ .

Other work [77, 78, 79, 80] along these lines has also tended to introduce another approximation, namely that of replacing the sum over the  $n$  dipoles in the unit cell with a weighted sum of the contributions from one representative dipole in each magnetic sublattice, the weighting factors being the number of dipoles in each of the sublattices. It has been shown, however [81], that the value of the dipolar anisotropy calculated using this method gives the wrong value in M-type (and other) ferrites due to the fact that the calculated anisotropy contribution  $k_{ij}$  from sublattice  $i$  due to sublattice  $j$  does not equal  $k_{ji}$ . For this reason we will carry out the summation over all the dipoles in the unit cell individually.

We can therefore calculate  $E''$  by combining Equations (6.33), (6.24) and (6.27) and performing the summations. If the system that we are considering is an ideal crystal platelet, it may be seen that the centre and axial symmetry will cause the contributions to the summation from the linear terms (odd functions of angle) on the RHS of Equation (6.27) to vanish. These terms will also vanish approximately in the case of a textured film with the  $c$ -axis parallel or perpendicular to the film plane. Equation (6.27) then becomes

$$(\hat{\mathbf{m}} \cdot \hat{\mathbf{r}}_{ij})^2 = \sin^2 \theta \sin^2 \theta_{ij} [\cos^2 \phi \cos^2 \phi_{ij} + \sin^2 \phi \sin^2 \phi_{ij}] + \cos^2 \theta \cos^2 \theta_{ij}. \quad (6.34)$$

The summation over  $j$  in Equation (6.33) also takes place over a large number

of ions in a sphere of radius  $R_c$ , and hence  $\phi_{ij}$  can take any value between 0 and  $2\pi$ . Therefore, for fixed values of  $\theta$ ,  $\phi$  and  $\theta_{ij}$ , we may replace  $\cos^2 \phi_{ij}$  and  $\sin^2 \phi_{ij}$  in Equation (6.34) with their average values, i.e.  $1/2$ . Hence

$$(\hat{\mathbf{m}} \cdot \hat{\mathbf{r}}_{ij})^2 = \frac{1}{2} \sin^2 \theta \sin^2 \theta_{ij} + \cos^2 \theta \cos^2 \theta_{ij} \quad (6.35)$$

which reduces to

$$(\hat{\mathbf{m}} \cdot \hat{\mathbf{r}}_{ij})^2 = \cos^2 \theta_{ij} - \frac{1}{2}(3 \cos^2 \theta_{ij} - 1) \sin^2 \theta \quad (6.36)$$

We may therefore now express the angular dependence of the dipolar energy density by combining Equations (6.33), (6.24) and (6.36), thus

$$E'' = E_0 + \frac{3M^2 \sin^2 \theta}{16\pi\mu_0 V_c} \sum_{i \in V_u}^n \sum_{\substack{j, \\ r_{ij} < R_c}} \frac{s_i s_j}{r_{ij}^3} (3 \cos^2 \theta_{ij} - 1) \quad (6.37)$$

where all the constant terms have been absorbed into the isotropic part of the free energy density  $E_0$ . Comparing this expression with the phenomenological expression for the free energy given in Equation (4.5), we can finally express the dipolar contribution to the uniaxial anisotropy constant  $K_{u1}$  as

$$K_{u1,\text{dip}}'' = \frac{9M^2}{16\pi\mu_0 V_c} \sum_{i \in V_u}^n s_i \sum_{\substack{j, \\ r_{ij} < R_c}} \frac{s_j}{r_{ij}^3} \left( \cos^2 \theta_{ij} - \frac{1}{3} \right). \quad (6.38)$$

We will use this equation later in the computational evaluation of the dipolar contribution to  $K_{u1,\text{dip}}$ . Further details of the implementation and the algorithm used may be found in Section 8.2.5, and the results of calculations may be found in Section 9.

## 6.2 Extension of the magnetic theory for thin films

### 6.2.1 Macroscopic expression for magnetic shape anisotropy of a thin film

The expression for the demagnetizing energy  $U_D$  of a magnetized body of volume  $V$  may be written [35] as an integral over the dot product of the intensity of magnetization  $\mathbf{I}$  and the demagnetizing field  $\mathbf{H}_D$ . In the case of a homogeneously magnetized flat plane, in which the magnetization points perpendicularly out of the plane (and hence the demagnetizing field points perpendicularly *into* the plane) this becomes

$$\begin{aligned} U_D &= -\frac{1}{2} \int_V I H_D dV \\ &= -\frac{1}{2} I \left( -\frac{N}{\mu_0} \right) IV \\ &= \frac{I^2}{2\mu_0} V \end{aligned} \tag{6.39}$$

since the demagnetizing factor  $N = 1$  for an infinite flat plane. If the demagnetizing energy density is then written as

$$E_D(\theta) = U_D(\theta)/V = K_D \sin(\theta) + E_0 \tag{6.40}$$

where  $\theta$  is the angle between the normal to the plane and the direction of the magnetization, it is seen that  $E_D$  take its maximum value ( $= I^2/2\mu_0$ ) when the magnetization is perpendicular to the plane ( $\theta = 0$ ) and its minimum value ( $= 0$ ) when the magnetization lies in the plane ( $\theta = \pi/2$ ). Substituting these values into the previous equation gives the expression for the anisotropy  $K_D$  due to the demagnetizing field

$$K_D = -E_0 = -\frac{I^2}{2\mu_0}. \tag{6.41}$$

### 6.2.2 Definition and derivation of surface anisotropy

The total free energy associated with a flat ferrite platelet of surface area  $S$  and thickness  $t$  (and hence volume  $V = St$ ) is given [82, 83] by

$$E = K_V V + 2K_S S \quad (6.42)$$

where  $K_V$  and  $K_S$  are the ‘volume’ and ‘surface’ contributions to the anisotropy, and the factor 2 arises from the fact that we must count the contributions from both the ‘upper’ and ‘lower’ surfaces, making the implicit assumption that these two contributions are equal. We also assume that  $t \ll \sqrt{S}$ , i.e. that the edges of the platelet do not contribute to the anisotropy. Dividing this equation through by the volume of the platelet gives

$$K_{total} = E/V = K_V + 2K_S/t. \quad (6.43)$$

The volume and surface anisotropies may then be extracted from the intercept and gradient of a straight line fitted to the values of total anisotropy plotted against  $(1/t)$ .

### 6.2.3 Other necessary modifications of the bulk theory

The environments of magnetic ions at or near a material interface will be different from those of ions in the bulk crystal due to the broken symmetry and possible structural distortions associated with local relaxation and/or reconstruction. While it is possible within the framework of the Superposition Model to take account of variations in the relative geometrical arrangement of ligands around magnetic ions, this work has been carried out using the

assumption that no such distortions take place. On the other hand, *missing* ligands at surfaces and interfaces are accounted for by simply neglecting their contribution to the single-ion anisotropy of the site in question.

Further details of the algorithms used to calculate the contributions to the anisotropy can be found in Section 8.2, and the corresponding pseudocode is given in Appendix D.

## 7 Deposition theory

### 7.1 Arrhenius law for surface diffusion

The rate at which a stochastic process occurs (in this case the thermally-activated hopping of growth units on a surface ) may be thought of as being governed by the probability of overcoming an energy barrier  $E_{barrier}$ . Using the Arrhenius formulation, this dependence may be written as

$$R_{hop} = \nu_0 \exp\left(\frac{-E_{barrier}}{k_B T}\right) \quad (7.1)$$

where  $k_B$  is the Boltzmann constant,  $T$  is the temperature of the substrate in Kelvin, and  $\nu_0$  is an ‘attempt frequency’. It is then common practice [84] to consider that the energy barrier is made up of additive contributions which depend on the local environment of the growth unit. In other solid-on-solid (SOS) model simulations (see next Section) these contributions to the barrier energy for a given growth unit have been taken as coming from the layer under the growth unit, from each immediately neighbouring growth unit in the same layer, and also, in the case of the growth of terraces on semiconductor surfaces, from the edges of the terraces [84]. We have adopted the first two types of barrier contribution in this study, with an additional constant term which only applies to growth units in the first layer (as a simple first approximation to the effect of film-substrate structure mismatch).

The expression used for the contributions to the energy barrier for a given growth unit is therefore

$$E_{\text{barrier}} = \left\{ \begin{array}{c} E_{cc} \\ E_{sub} \end{array} \right\} + nE_{aa} \quad (7.2)$$

where  $E_{cc}$  and  $E_{sub}$  are the ‘surface’ contributions if the layer underneath consists of film or substrate material respectively,  $E_{aa}$  is the contribution from each immediately neighbouring growth unit in the same layer, and  $n$  is the number of these neighbours. The use of the distinct energies  $E_{cc}$  and  $E_{sub}$  allows for the possibility that the interaction between the film material and the substrate material may be different from that between growth units of the film material, possibly due to interfacial strain caused by lattice mismatch or irregularities on the substrate surface.

## 8 Simulation Techniques and Programs

### 8.1 DEPOSIT - deposition modelling

The problem of simulating the deposition and growth of materials has traditionally been approached using one of two broad classes of methods. The first class of methods [85] treats the growing system as a continuum, the boundaries of the growing system being defined by continuous analytic functions of some spatial variable(s) and of time. The time evolution of these functions is determined by a stochastic differential equation. The second class of methods (which we will use) regards the growing system as an assembly of discrete growth units. The set of methods of interest to us are concerned with the random sequential adsorption of new growth units onto the surface of the growing system. The most widely-studied of these methods in the context of thin films are based on the *solid-on-solid* (SOS) model ([86, 87] and references within). In this model, growth units sit on a regular (usually square) grid in the plane of the film, newly-deposited units stacking on top of old such that the thickness of the growing film at any location on the grid can simply be represented by the number of growth units making up the ‘column’ sitting at that grid location. In such models growth units may stick where they originally fall, or they may be allowed to ‘hop’ to a neighbouring location by a random diffusion process, or even be allowed to desorb completely from the surface again.

Although the approach taken in our simulations is based on the SOS model, we have improved the model by adding important novel features.

Each growth unit in our model is allowed to have not only a location but also one of three possible orientations. This raises the difficulty that such a scheme requires an irregular grid. We have solved this problem by defining two interlocking grids, with half of each growth unit lying on each of the grids (see Section 8.1.1). This allows us to keep all the computational benefits of a regular grid while also allowing orientational disorder. Each growth unit is also individually tracked, rather than considering the number of growth units stacked at a particular location in the grid. This allows us to have voids in the growing film, so mimicking more closely the structure of a real physical film.

### 8.1.1 Geometrical definition

The fundamental *growth unit* in the simulation is a prism in the shape of a crystallographically hexagonal unit cell. These growth units are introduced into the *simulation cell*, which has the same shape as the growth units, and which is divided into a regular ( $N_a \times N_b \times N_c$ ) grid, each grid cell being the same size as a growth unit (see Figure 8.1). Growth units may stack together side-by-side and one on top of the other, taking up one of three possible orientations in the plane relative to the simulation cell axes (see Figure 8.2), while the c-axis of the growth unit remaining always parallel to the c-axis of the simulation cell. Periodic boundary conditions are also applied, such that a growth unit leaving the simulation cell through one side re-enters the simulation cell through the opposite side. Growth units in the lowest layer of the simulation cell are taken to be sitting on the substrate,

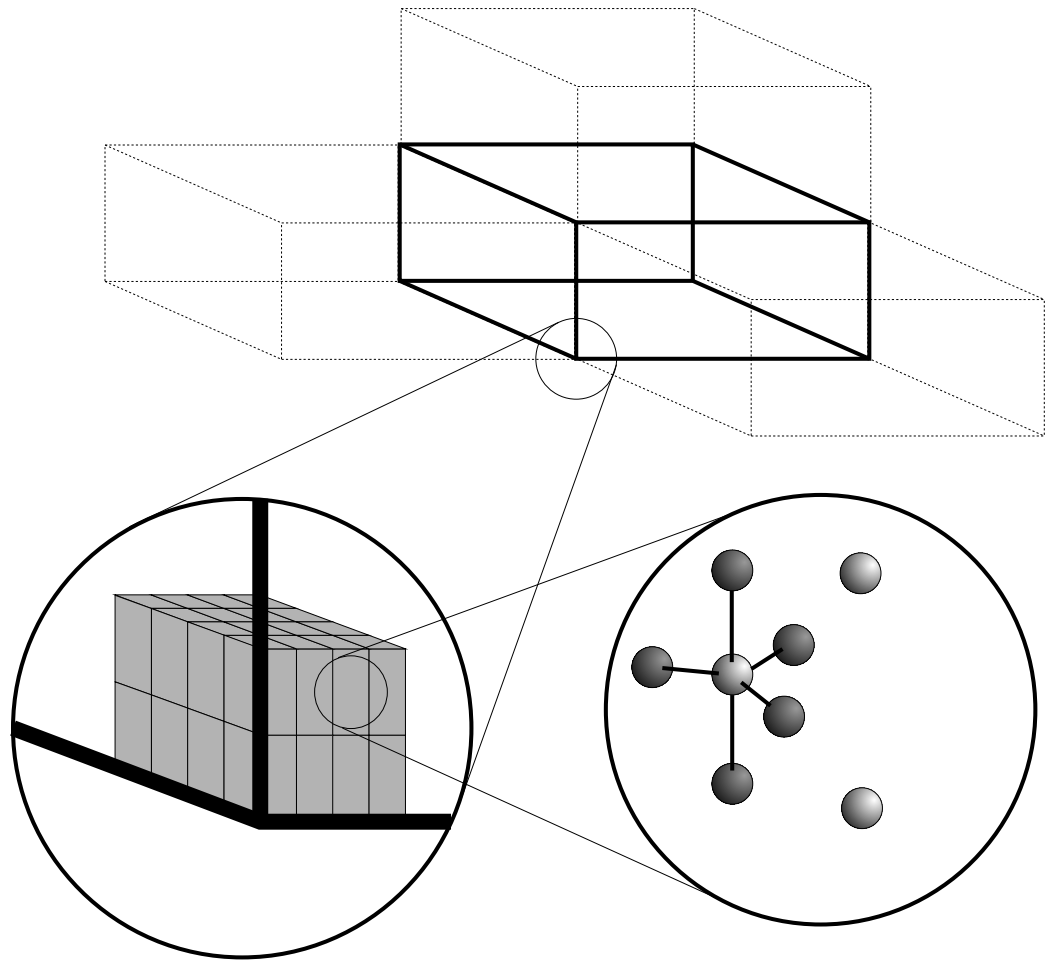


Figure 8.1: Model hierarchy

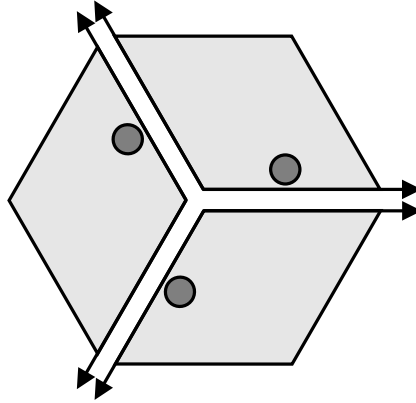


Figure 8.2: The three allowed orientations of the growth units in the plane

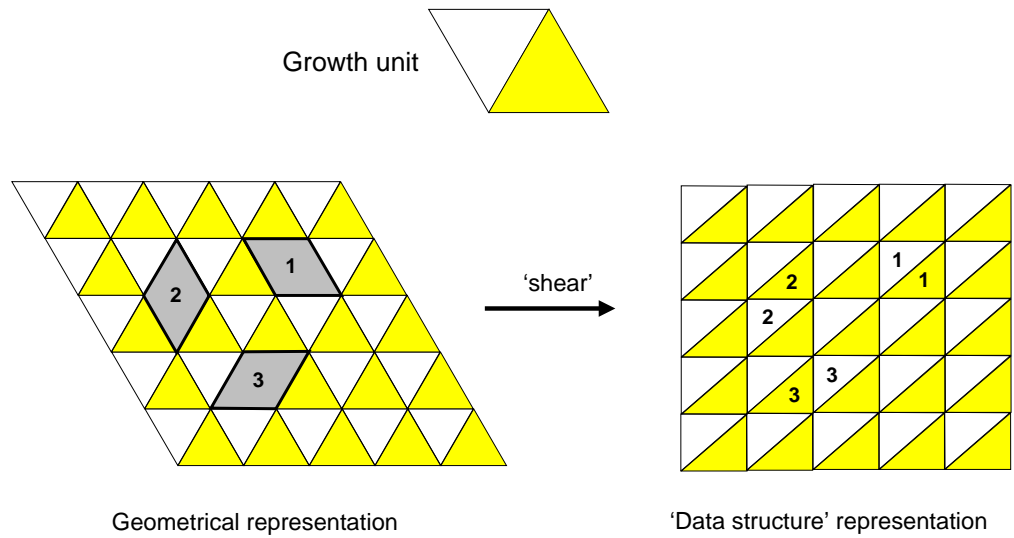


Figure 8.3: 'Geometrical' and 'data structure' representations of the simulation grid. Three growth units, denoted 1,2 & 3 are shown, with different locations and orientations in the simulation grid.

which is assumed to be perfectly smooth, but nevertheless giving rise to the contribution ,  $E_{sub}$ , to the energy barrier due to lattice mismatch.

Figure 8.3 illustrates how the geometrical model is represented as a data structure in the simulation programs. Each growth unit is considered to be composed of a ‘head’ and a ‘tail’ (shown in Figure 8.3 as open and filled triangles)- these two parts are effectively triangular prisms which share a common face to make a complete growth unit. The simulation cell can thus be divided up into two interlocking triangular grids, one of which can only contain ‘heads’ and the other ‘tails’. Every possible location and orientation of a growth unit can be represented by the presence of a ‘head’ in one triangular grid and the presence of a ‘tail’ in a neighbouring cell in the other triangular grid (Figure 8.3 illustrates this concept, showing three growth units, denoted 1,2 & 3, in different locations and orientations). The efficiency of this approach is demonstrated when the ‘geometrical representation’ in Figure 8.3 is ‘skewed’ - the ‘head’ and ‘tail’ grids can be seen to be representable by regular arrays in memory. The storage locations in these arrays can either be empty or contain an integer ‘ID number’ which identifies the particular growth unit to which the ‘head’ or ‘tail’ belongs. Using this data structure incurs a small computational overhead, as the program must ensure that the ‘head’ and ‘tail’ of any particular growth unit stay in adjacent cells in each of the grids as the growth unit migrates through the simulation cell or changes orientation, but this overhead is very small when compared to the time taken by other aspects of the growth model.

### 8.1.2 Kinetic definition

The time evolution of the system is assumed to take place as a sequence of discrete events. Two types of event can occur in the system - a new growth unit can be deposited, or an existing unit in the system may change its position and/or orientation. Re-evaporation of growth units from the surface, whilst usually included in previous similar Monte-Carlo simulations of the growth of metals, semiconductors etc., is not considered to be a significant factor since the growth unit contains a relatively large number of atoms. Both types of event included in the simulation are assumed to take place instantaneously.

New growth units are added to the system at a chosen constant deposition rate, starting at the top of the simulation cell at a random position and dropping vertically until they reach the bottom or land on top of another growth unit, hence modelling a constant spatially uniform flux of material impinging on the substrate. In addition, a newly-arrived growth unit is allowed a ‘transient’ mobility, such that it can immediately hop down into a laterally adjacent vacant site in the layer below if such a site exists. If several of such adjacent lower sites exists one is chosen randomly, each candidate site being allocated equal probability.

Growth units can hop around and change their orientation on the surface of the film, the hopping rate of any particular growth unit on the surface being determined by the number of immediately adjacent growth units using Equations (7.1) and (7.2). A growth unit can hop down into the underlying layer if a viable site exists there, but cannot hop upwards into a higher

layer. No additional (Ehrlich - Schwoebel type) energy barrier contribution, associated with such a hop down over a ‘ledge’ is considered here (unlike that which has been included in a number of similar MC studies of the growth of vicinal surfaces of semiconductors - see [88] for examples). It is difficult to justify the inclusion of such a barrier in our case, given the large number of atoms in the growth unit - the exact mechanism would be a complicated one, possibly even involving a substantial displacement of atoms in the underlying layer.

The substrate-film system is considered to be kept at a constant uniform temperature in order to simplify the simulation. This has the added benefit of allowing all of the exponentials to be calculated once at the beginning of the simulation, thus removing the need for a relatively time-intensive arithmetic operation in the ‘inner loop’ of the simulation.

### **8.1.3 Determination of process parameters**

The determination of the energy barriers to motion of the growth units is a difficult issue. Ideally these energies would be determined from a detailed experimental STM study of island growth at very low coverages on a perfect single-crystal ferrite substrate. To my knowledge, no such study has yet been carried out. The computational cost of all-electron *ab initio* total energy calculations using modern electronic structure codes would also be prohibitive. In view of these difficulties, a calculation scheme involving summation of the Coulomb energy contributions from pairs of point charges has been implemented (see Section 9.5.2 of this thesis).

In the interests of establishing the behaviour of the film growth model, both the attempt frequency  $\nu_0$  and the temperature factor  $k_B T$  in Equation (7.1) are taken to be unity (the latter then effectively rendering the barrier energy contributions dimensionless). The incoming flux of deposited growth units  $F$  is also taken to have units of (number of growth units per unit area per unit simulation time) and hence the overall deposition rate  $R_{dep}$  is given by

$$R_{dep} = N_a N_b F \quad (8.1)$$

where the unit of area is taken to be the area of the  $\{001\}$  face of a single growth unit.

#### 8.1.4 The deposition and growth algorithm

The algorithm used to model the evolution of the thin film belongs to the class of variable-timestep Monte Carlo methods. It is based on the assumption that the evolution takes place as a sequence of discrete events, each of which occurs instantaneously, and that the system does not change in the time between these events. In this work it is also assumed that only two types of event are possible; the arrival on the film of a new growth unit, and the ‘hopping’ of an existing growth unit from one site in the film to another, possibly accompanied by a change in orientation of the growth unit. It is also possible in this simulation that growth units may simply reorient themselves ‘in place’ - this is considered to be a hop of zero length. In addition, the growth units are allowed to touch but not overlap.

We therefore define total rates of deposition and hopping by summations

over all the eligible sites as

$$R_{dep} = \sum_i d_i \quad (8.2)$$

$$R_{hop} = \sum_i h_i \quad (8.3)$$

where  $d_i$  and  $h_i$  are respectively the probabilities per unit time of a deposition or hopping event taking place at site  $i$ . One can define a total rate of events for the whole system as

$$R_{tot} = R_{dep} + R_{hop} \quad (8.4)$$

Elementary probability theory states that the distribution of time intervals  $\tau$  between events is given by

$$P(\tau) = R_{tot} \exp(-R_{tot}\tau) d\tau \quad (8.5)$$

The variable  $u = \exp(-R_{tot}\tau)$  is randomly distributed between 0 and 1, and hence the time between successive events may be chosen by solving the equation

$$r = \exp(-R_{tot}\tau) \quad (8.6)$$

where  $r$  is a random number uniformly distributed between 0 and 1. We now know when the next event will occur, and the further task is to decide on the type and location of the event. The method used to do this is shown in schematic form in Figure 8.4, where the conditional probabilities are arranged along a line segment, whose length is given by  $R_{tot}$ . A second random number  $r_2$  is chosen from a uniform distribution between 0 and 1, and the type of event is chosen to be a deposition if  $R_{tot}r_2 < R_{dep}$ , or a hop if  $R_{dep} \leq R_{tot}r_2 <$

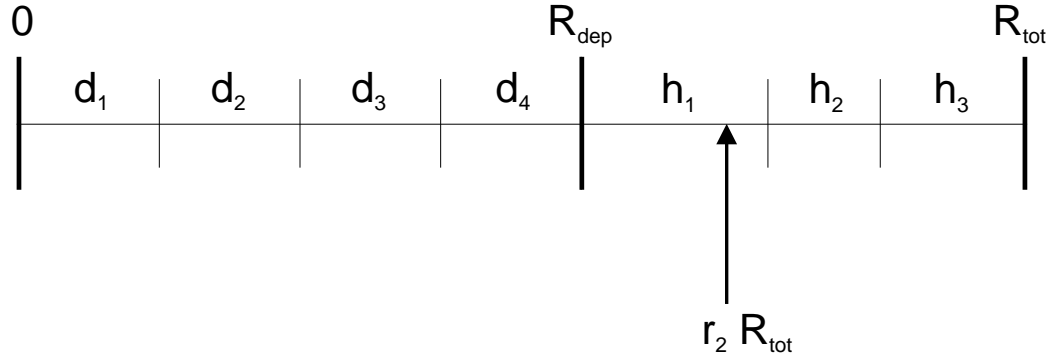


Figure 8.4: Schematic of the algorithm for choosing the type and site of the next event.

$R_{tot}$ . The location of the event is decided in a similar way. For example, if the event is a hop, then the site  $i$  affected is chosen by finding the largest  $i$  such that

$$R_{tot}r_2 - R_{dep} \geq \sum_{j=1}^{i-1} h_j. \quad (8.7)$$

The evolution of the system thus proceeds by examining the current state of the system, calculating from this state the overall rates of the different types of events, then using these rates to select the time, location and type of the next event. The rates are then updated for the new configuration of the system, and cumulative rate sums are computed for all the sites. The whole process is repeated until the simulation is complete.

Reference [89] extended this technique (for which the time per event scales as the total number of sites  $N$ ) by dividing the sites into groups and maintaining separate cumulative sums for the groups. For the optimal choice of the size of a group, the time per event scales as  $\sqrt{N}$ . It is also then possible to recursively divide these groups into sub-groups in such a way that the

scaling approaches  $\ln_2 N$  [90].

In our simulations, the flux of incoming growth units is considered to be constant and spatially uniform. Deposited growth units are dropped vertically into the simulation cell at random positions.  $R_{dep}$  is therefore constant during the course of a simulation run, and does not have to be computed using Equation (8.2) at each step - Equation (8.1) is used instead. Similarly, we maintain cumulative hopping rate tables for all *growth units* in the system, not for all *sites*. This avoids the need to update hopping rates (and hence cumulative hopping rates) for sites on which no growth unit yet exists.

#### 8.1.5 The DEPOSIT program

The DEPOSIT program takes as input a film data file and a set of growth conditions, and produces an output film data file corresponding to the processed film, along with an output file summarizing some of the film statistics (see Section 8.3). The program can also be set to produce ‘checkpoint’ film data files periodically during the simulation run, representing the interim state of the partially-completed simulation run. These checkpoint files can be very useful in cases when the simulation runs are very time-intensive - they can be used to ‘restart’ a simulation run if the calculations are terminated prematurely by a system crash, or even by simply running up against a per-job CPU time limit such as may be imposed by some job queueing software. The process parameters specified at the beginning of a deposition run remain in force for the duration of that simulation run. Multiple simulation runs with different process parameters may be performed however, as

the final output file from one deposition simulation run can be used as the input file (starting conditions) for the next. The entire ‘processing history’ of every film data file is recorded (in the form of ‘comments’ describing the process parameters used) at the beginning of the film data file (see Figure 8.5 for an example).

Pseudocode for the DEPOSIT program can be found in Appendix C.

## **8.2 KFILM - anisotropy simulation**

The anisotropy program KFILM takes as input an ASCII file which contains all the structural details of the simulated film, such as that produced by the deposition program DEPOSIT described above. This section describes the overall ‘mean-field’ approach taken to the anisotropy calculations, followed by descriptions of the calculation of the single-ion and dipolar contributions.

### **8.2.1 The ‘mean-field’ model**

In the growth model described earlier, the growth units stack together like solid prisms, sharing edges and faces with other growth units. Bringing this geometrical description of the simulated film together with the simulation of the magnetic properties requires that the positions of the ions in each growth unit be known. The easiest way to approach this task (and the approach adopted in the remainder of this thesis unless stated otherwise) is to equate one growth unit with one conventional unit cell.

An approach has been adopted where atoms which lie on any boundary of the unit cell are duplicated and given partial occupancies which reflect the

```

%
% Film created by MakeSlab
%
% Initial time = 0.000000000000000000E+00
% Simulation cell dimensions 10 10 25
% Total number of growth units = 1
%
% Interaction energies
% Eaa = 1.000000000000000000
% Ecc = 5.000000000000000000
% Ecs = 5.000000000000000000
%
% Number of groups = 1
% Initial orientation = 1
%
%
% PROCESS RECORD
% Process duration:      1.00000
% Deposition rate was:  100.00000
% Substrate temperature was:  1.00000
% No. of deposition events =      98
% No. of hopping events   =       1
%
%
% PROCESS RECORD
% Process duration:      1.00000
% Deposition rate was:  100.00000
% Substrate temperature was:  1.00000
% No. of deposition events =      97
% No. of hopping events   =       1
%

```

Figure 8.5: Excerpt from the initial section of a DEPOSIT film data file. Note the lines recording the ‘process parameters’ for each successive deposition run - these lines record the ‘processing history’ of a simulated deposited film.

nature of their position on the boundary. The simplest example of this would be an atom lying at the origin of the unit cell. In an infinite crystal, ‘copies’ of this atom lie at every corner of every unit cell due to the lattice periodicity. A single atom on this site could then be considered to be ‘shared’ between adjacent unit cells. In order, therefore, to avoid any ambiguity about which boundary atom belongs to which unit cell (and hence growth unit), it is convenient to regard the contents of every unit cell as independent entities in the following way. Instead of considering each growth unit to have a single site of occupancy  $x$  at the origin, the growth unit is taken to contain 8 distinct sites, each with occupancy  $x/8$ , situated at each of its corners. In an analogous way, sites of occupancy  $x$  situated on the edges or corners of the unit cell are replaced with multiple sites with occupancy  $x/4$  and  $x/8$  respectively in each growth unit, preserving the ‘overall’ number of sites of these types in the unit cell. Figure 8.6 illustrates this idea with a two-dimensional lattice.

The main advantage of this approach is that the contents of every growth unit can be considered to be unique to that unit. Any quantity which is regarded as being the sum of contributions between pairs of sites must then be constructed as the sum of terms which are the basic pair contribution weighted by the product of the occupancies of each site making up the pair. Both the single-ion and dipolar contributions to the anisotropy which are of interest to us are the sum of pair contributions in this way: for the single-ion anisotropy, each pair consists of an Fe site and an O site, and for the dipolar anisotropy the interactions are between two Fe sites. In the case of

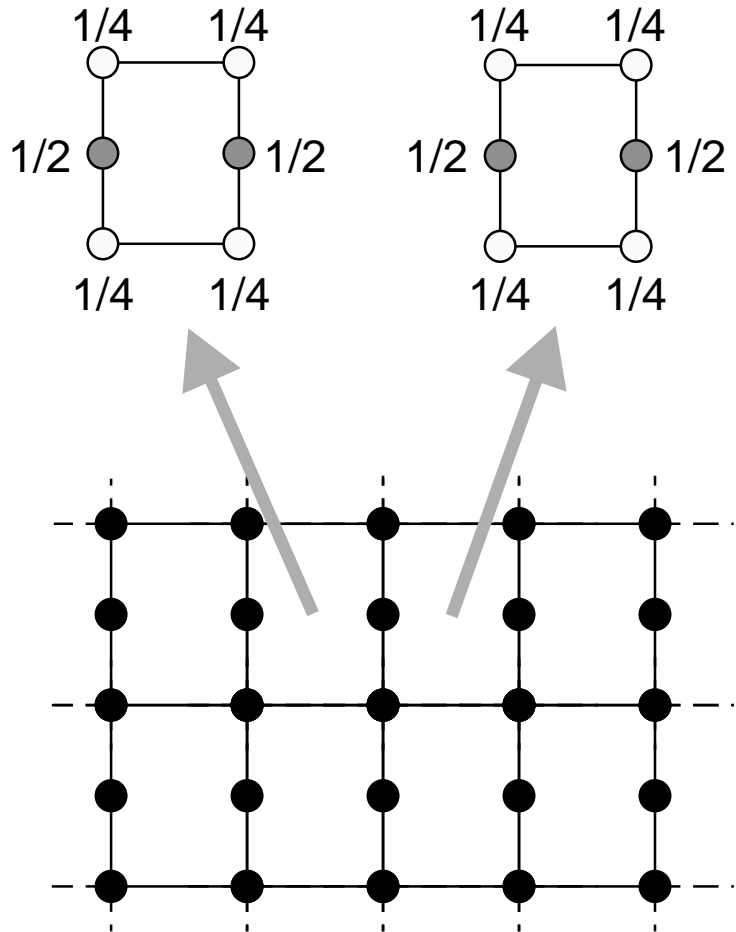


Figure 8.6: An illustration of an alternative way of regarding the structure of a 2-D infinite lattice. The lower picture shows the infinite lattice, each site having unit occupancy (shown here as black filled circles). Alternatively (upper pictures), the lattice can be regarded as an assembly of independent cells, sites on the boundaries having partial occupancies as shown.

the dipolar anisotropy, additional care must be taken to avoid calculating the interaction between two partial Fe sites (possibly from different growth units) which lie at exactly the same position in space, as the result would be infinite: such pairs are ignored in the construction of the dipolar sum.

Using this ‘mean-field’ approach has several consequences, both favourable and unfavourable. From a purely computational perspective, more work is required, as there are now more ‘effective’ sites to be considered than with the conventional approach. On the positive side, however, no special provision needs to be made to preserve the overall stoichiometry of the system at boundaries between a growth unit and the empty space in the simulation cell. Such boundaries naturally generate sites with uncompensated partial occupancies, e.g. at the surface of the film or at voids in the interior of the film, which will have different single-ion and dipolar contributions to sites deep in the film or in regions with perfect local crystalline order. In this way, the effect of the presence of material interfaces in the system is transparently taken into account.

### **8.2.2 Unit cell data file**

Each growth unit in the simulation is taken to correspond to one unit cell of the deposited material. After the file describing the hexaferrite structure has been read in, the program reads in a user-specified file containing the fractional coordinates of all of the Fe and O ions in the unit cell, using a slightly modified (and greatly simplified) version of the file format used by the crystallographic program SHELX [91]. This format was chosen because

it consists of human-readable (and hence easily editable) ASCII data with a very clear layout, and has provision for allocating each atom a fractional occupancy. This latter facility is essential for the operation of the KFILM code. In addition, many software packages designed to aid the visualization and editing of crystal structures can import and export files in the SHELX format, considerably simplifying the task of preparation of input files.

The unit cell data file starts with a header consisting of three lines. The first line of the header consists of the SHELX keyword TITL, followed by an alphanumeric string corresponding to a user-chosen title for the file. The program KFILM only reads the first 80 characters of this line. The second line of the header consists of the SHELX keyword CELL, followed by seven numbers separated by spaces. The first number is used in a conventional SHELX file to represent the wavelength in Angstroms of the radiation (such as X-rays) used in a diffraction experiment to discover the cell parameters and atom positions. This quantity is not relevant in our case, so we set it to zero. The remaining six numbers represent the values, in order, of the lattice parameters ( the distances  $a$ ,  $b$ , and  $c$  given in Angstroms, and the cell angles  $\alpha$ ,  $\beta$  and  $\gamma$  given in degrees). The third line of the header consists of the SHELX keyword LATT followed by the letter P to indicate that this is the *primitive* unit cell.

Following the header there are a number of atom records, each record consisting of a single line and corresponding to the data for a single atom in the structure. There is no provision for symmetry operators in the file, as in standard SHELX files: each individual atom in the whole unit cell has its

own record, regardless of any symmetry present. The atom records have the following format

**Label** **NotUsed** **FracX** **FracY** **FracZ** **Occupancy** **Spin**

where the fields are defined as follows

**Label** is an alphanumeric string of 5 characters, indicating the type of the atom. In this application the label will start with the letters ‘BA’, ‘FE’ or ‘O’, indicating barium, iron and oxygen atoms respectively.

**NotUsed** This field is present in conventional SHELX files, and is only used here for compatibility reasons. Always set to ‘0’.

**FracX** Fractional coordinate of atom in *a*-direction

**FracY** Fractional coordinate of atom in *b*-direction

**FracZ** Fractional coordinate of atom in *c*-direction

**Occupancy** Fractional occupancy of site

**Spin** This field is only non-zero (and hence significant) for Fe sites. It encodes two pieces of information. The sign is used to specify that the net spin on the ion is ‘up’ or ‘down’ i.e. parallel or antiparallel to the crystallographic *c*-axis. The magnitude denotes which of the five crystallographic sublattices the site belongs to.

The unit cell data file is terminated by a line containing only the string ‘END’, again for SHELX compatibility. An example unit cell data file may be found in Appendix A of this thesis.

### 8.2.3 Single-ion data file

After the unit cell data file, the program then requests the name of a single-ion data file. This file consists of two lines, the first containing the values of the  $r_0$ ,  $b_2$  and  $t_2$  superposition model parameters used to calculate the contribution for every ligand in the structure except the equatorial oxygen ligands associated with the  $2b$  sites. The parameters for the latter ligands are given on the second line (see Section 6.1.1.6 and Table 6.1 for numerical values and descriptions of these parameters).

### 8.2.4 Evaluating the single-ion contributions

The calculation of the single-ion contributions require the evaluation of the ligand-ion distances and the geometrical factor  $Z_2^0$  (using Equation (6.20) )for every magnetic ion in the simulation cell. This requires a search for neighbouring O ions around every Fe site in every growth unit, taking into account the periodicity of the simulation cell. The intrinsic parameters (previously read in from a data file) are then used to evaluate and sum the contributions to the spin Hamiltonian parameter from each ligand of each ion.

### 8.2.5 Evaluating the dipolar contributions

The dipolar contribution is evaluated by summing the interactions between every ion  $i$  and every other ion  $j$  (along with all of its periodic copies which lie within the cutoff radius) in the simulation cell. A number of measures are taken to avoid wherever possible evaluating the distance  $r_{ij}$ , which involves the relatively computationally expensive evaluation of a square root. Firstly,

if any component of  $r_{ij}$  exceeds the cutoff radius, the program immediately moves on to consider the next  $(i, j)$  pair. The square of the magnitude of  $r_{ij}$  is then compared with the square of the cutoff radius to accept or reject the candidate  $(i, j)$  pair. The number of square root operations is therefore minimized.

### 8.2.6 Effect of distorted sites and missing ligands

The model described and used in this work to calculate the magnetic properties of a ferrite thin film makes the assumption that the crystal structure of growth units at interfaces between the growing film and its environment (such as the substrate material or the near-vacuum in the growth chamber) is the same as for the bulk crystal. For a real film, this is unlikely to be true, as there will most likely be a degree of reconstruction associated with the interfaces. The underlying physical model used to calculate the single-ion contribution to the anisotropy, however, has the capability to accommodate small local geometrical changes, although this has not been implemented in the current version of the code. The other main difference between the structure at interfaces and in the bulk will be that Fe ions at the interfaces may have 'missing' oxygen ligands - these missing ligands should be fairly well simulated by the uncompensated partial occupancies on oxygen sites permitted by the 'mean-field' model used by the code and described in Section 8.2.1 of this thesis.

### 8.2.7 Summation of anisotropy contributions over all ions in film

The single-ion and dipolar contributions are added, and the result divided by the overall volume of *material* in the simulation cell (i.e. neglecting the volume of any voids) to give the total uniaxial anisotropy energy per unit volume of the simulated film.

Pseudocode for the KFILM program may be found in Appendix D.

## 8.3 FILMSTAT - extraction of film statistics

The program FILMSTAT was written to extract some statistics from a simulated deposited film, and also produce some output allowing visualisation of the grown film.

### 8.3.1 Film statistics

A number of statistical measures are calculated from each input structure. These are:

- Average thickness, defined as

$$\text{Average thickness} = \frac{1}{N_a N_b} \sum_i^{N_a} \sum_j^{N_b} h_{ij} \quad (8.8)$$

where  $h_{ij}$  is the  $z$ -coordinate of the highest growth unit associated with the grid location  $(i, j)$  in the plane of the film.

- Averages of deviation and absolute deviation from the average thickness
- Roughness, defined as the root mean square deviation from the average thickness.

- Percentage of voids by volume
- Average nearest-neighbour coordination. The quantity is calculated as the average number of growth units surrounding a given growth unit in the same layer. This gives a measure of the ‘clumpiness’ of the film.

### 8.3.2 Output files for visualisation

The FILMSTAT program can also optionally produce data files which may be used to visualise the structure of the grown film. These files may be of two different types, described in the next two sections.

**8.3.2.1 Geomview output** The first type consists of data describing a set of polygons in 3D space, using an ordered list of the coordinates of the vertices of each polygon. One polygon is produced for each side of every growth unit making up the simulated film structure. The data is written in the QUAD format, which is read by the free general geometry visualisation program Geomview [92]. This program allows the resulting collection of polygons to be viewed interactively from any angle and at any magnification. An example of the output of the Geomview program is shown in Figure 8.7 - this is the Geomview representation of the structure of a film generated using DEPOSIT.

This form of output suffers from the drawback that the file containing the QUAD data is often tens of megabytes in size, even for small simulation cells. Apart from the time needed to load and render such a large amount of polygon data, storage of large numbers of these files presents a

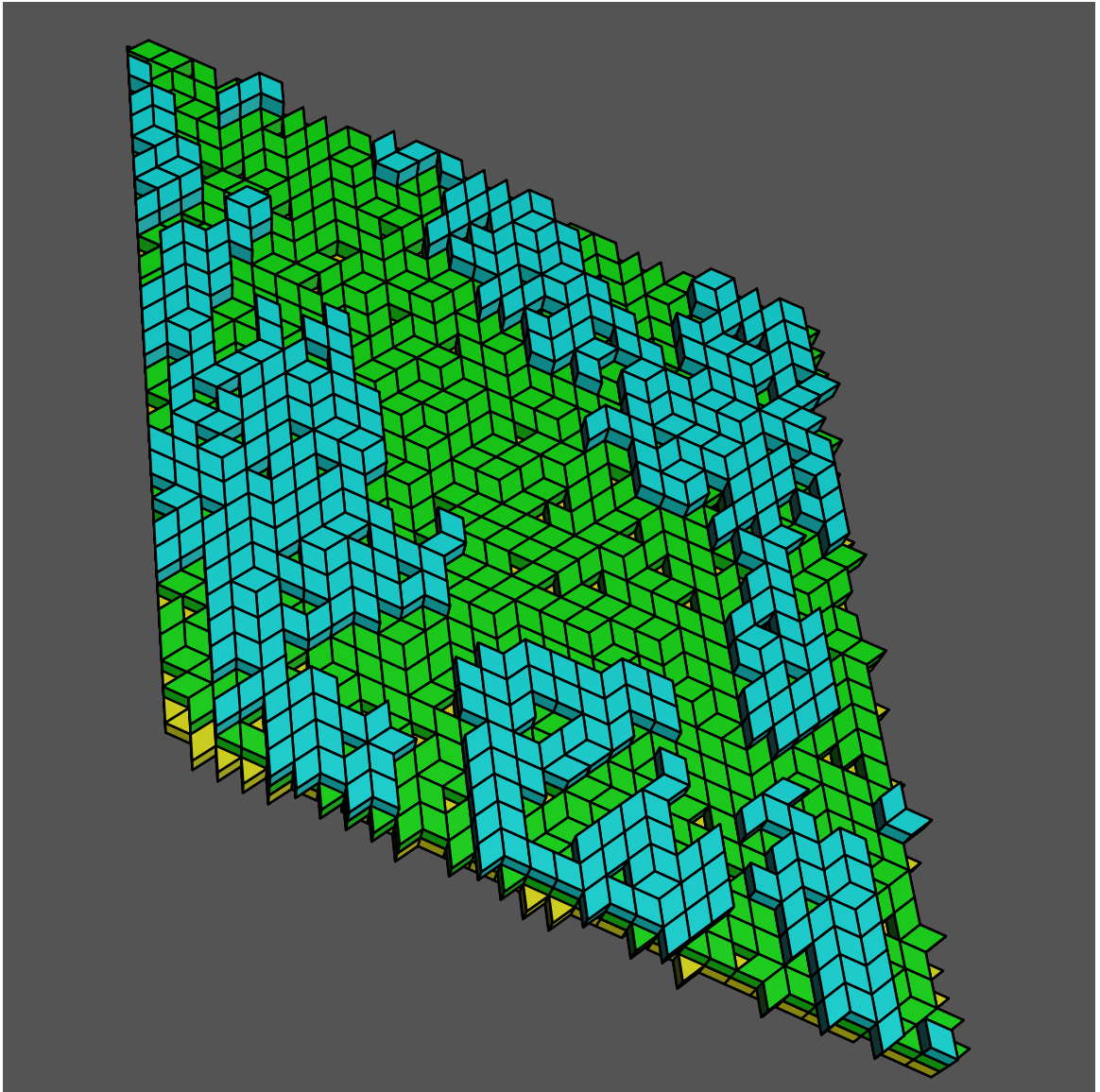


Figure 8.7: Example output of Geomview. The structure is that of a simulated grown film produced using DEPOSIT.

problem due to their size. A number of steps may be taken to alleviate these problems. Ordering the vertices of each polygon in a consistent manner allows Geomview to distinguish between the ‘inside’ and the ‘outside’ of each polygon making up the faces of each growth unit, and any polygon which is presenting its ‘inside’ to the viewer can be removed from the list of polygons to be drawn before any drawing is performed, a process known as *back-face culling*. Data in the QUAD format can also be converted from an ASCII format to the alternative binary OFF format, which gives a substantial reduction in file size. Furthermore, redundant and multiply-defined vertices, lines and polygons can be eliminated from the OFF file, reducing the file size even more. Auxiliary programs provided as part of the Geomview package provide these capabilities to convert and eliminate redundancies in QUAD and OFF files.

**8.3.2.2 Heightfield output** This is a simpler form of output, consisting of the position coordinates of the centre of the uppermost face of the uppermost growth unit (effectively the height of the column of material) at every distinct lateral location in the plane of the film. An assembly of such coordinates is known in computer graphics terms as a *heightfield*. These data files, representing the ‘envelope’ of surface of the film, are of a much more manageable size. A small script for the general-purpose mathematics package MATLAB was specially written to read and draw heightfields, allowing the results of the deposition simulations to be qualitatively examined. The graphical output from the MATLAB script may be seen in Section 9.6 in this

thesis (Figures 9.18 and 9.19).

## 9 Results

Unless otherwise stated, all of the calculations described in this chapter were performed on the 24-processor IBM SP2 computer ‘dirac’ in the Department of Physics, University of Salford.

### 9.1 Magnetic anisotropy of the bulk crystal

The program KFILM was used to determine the dipolar and single-ion anisotropies of an infinite 3-D crystal of BaM. Full use was made of the periodic boundary conditions by specifying a  $(1 \times 1 \times 1)$  simulation cell which was occupied by a single unit cell of BaM, whose environment was then effectively identical to the bulk crystal. Two cases were considered: the first with the bipyramidal sites being considered as 2b sites, and the second as 4e sites where the bipyramidal Fe ions were taken to be ‘frozen’ in the ‘up’ position. An additional calculation was performed where one site was ‘up’ and the other ‘down’ - this yielded identical results to the ‘both up’ case. Similarly, the summation algorithms were tested by using completely filled  $(2 \times 2 \times 2)$  and  $(4 \times 4 \times 4)$  simulation cells - again these calculations yielded identical results to the  $(1 \times 1 \times 1)$  case.

#### 9.1.1 Single-ion contribution

This was calculated using the SM parameters given in Table 6.1 and [93] for the case of  $T = 0K$ , and the results are shown in Table 9.1. As expected, the largest contribution came from the bipyramidal sites. The two possible

configurations of these sites (either as 2b or 4e) gave contributions which differed by about 7 percent.

Sublattice	No. of ions per unit cell	$D_i$ parameter ( $\text{cm}^{-1}$ )	Single-ion contribution to $K_1$ per one ion ( $\times 10^5 \text{ Jm}^{-3}$ )	Sublattice total ( $\times 10^5 \text{ Jm}^{-3}$ )
12k	12	0.076414	-0.10877	-1.30646
4f2	4	0.043619	-0.06215	-0.24861
4f1	4	0.026871	-0.03828	-0.15315
2b(4e)	2	-2.02451 (-1.8921)	2.88477 (2.69611)	5.76955 (5.39222)
2a	2	-0.040597	0.05784	0.11569
			Total single-ion contribution	4.17701 (3.79968)

Table 9.1: Single-ion contributions to the anisotropy from the five sublattices.

### 9.1.2 Dipolar contribution with convergence analysis

The calculated dipolar contribution showed slow convergence with increasing cutoff radius, with large oscillations at small values of the cutoff radius. The slow convergence is probably to be expected, since the dipolar interaction energy between two dipoles drops off as  $r^{-3}$  but the number of dipoles interacting with any given dipole also goes up as  $r^3$ . The large oscillations at small cutoff radii can be explained in terms of the partial cancellation of the

relatively large contributions from successive ‘shells’ of dipoles contributing to the sum. Figure 9.1 shows the convergence of the ‘central’ (2b) and the ‘both up’(4e) cases. Actual calculated values are shown in Figure 9.1, along with corresponding values obtained by linear extrapolation from the previous two values. The calculated value of the total dipolar anisotropy contribution for the case that bipyramidal Fe cations are in 2b sites was determined to be approximately  $1.738 \times 10^4 Jm^{-3}$ , while the value for the bipyramidal Fe cations being in 4e sites was slightly higher ( $1.762 \times 10^4 Jm^{-3}$ ).

### 9.1.3 Comparison with experimental values

The sum of the dipolar and single-ion contributions to the bulk anisotropy shown in Table 9.2 is close to the experimental value, i.e.  $4.4 \times 10^5 Jm^{-3}$  at T=0K [1].

	Bipyramidal 2b ( $\times 10^5 Jm^{-3}$ )	Bipyramidal 4e ( $\times 10^5 Jm^{-3}$ )
Single-ion	4.17701	3.79968
Dipolar	0.17380	0.17620
TOTAL	4.35081	3.97588

Table 9.2: Calculated magnetic anisotropy contributions for bulk.

The total for the bipyramidal site being classified as a 2b site is closer to the experimental value than for the 4e classification. This may indicate that at 0K the correct classification for the site is 2b.

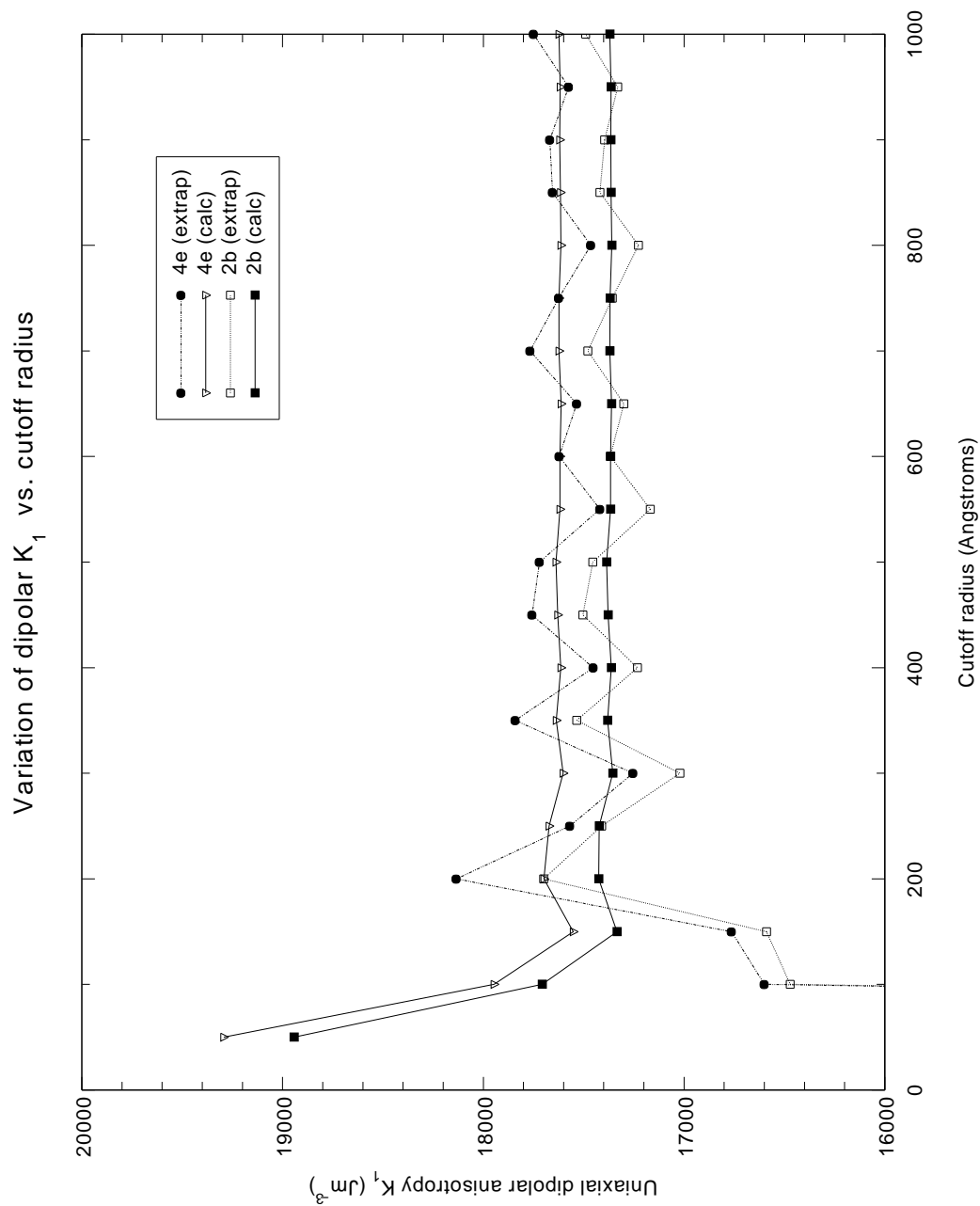


Figure 9.1: Convergence of the total dipolar contribution to the anisotropy with respect to the dipolar cutoff radius, plotted for the two cases of the Fe cations being at the 2b and 4e positions. Extrapolated values for each of these cases are also shown.

## 9.2 Magnetic anisotropy of an infinite perfect film

This case corresponds to a perfect crystal which is infinite in two perpendicular directions but finite in a third. For our purposes this third direction will be the vertical axis, and the crystal is such that the crystallographic c-axis also lies along this direction.

### 9.2.1 Estimate of the magnetic shape anisotropy of a thin film

Substituting the tabulated experimental value of  $I$  for  $\text{BaFe}_{12}\text{O}_{19}$  into Equation (6.41) in Section 6.2.1 gives the value  $K_D = -1.78 \times 10^5 \text{Jm}^{-3}$ . This serves as the phenomenological value for the shape anisotropy of a thin film of  $\text{BaFe}_{12}\text{O}_{19}$ .

### 9.2.2 Estimating the dipolar contribution using a ‘tile’ model

**9.2.2.1 Definition and theory for tile model.** We can independently make an estimate of the dipolar contribution to the anisotropy of a thin film by considering a thin square platelet of magnetic material, of side  $a$  and thickness  $t$ , divided into a regular square grid of  $(N \times N)$  ‘tiles’ of side  $h = a/N$ , each labelled by a pair of integers  $(i, j)$  giving their position in the grid (see Figure 9.2). The total magnetic moment of each element is therefore  $M = Ih^2t$ . We can then (using Equation (6.24)) treat, in the first approximation, each element as being close to an elementary dipole, with all the dipoles assumed to be parallel to each other ( $s_i = s_j = 1$ ) and perpendicular to the plane of the platelet. This then gives the expression for the interaction energy of the element at  $(i, j)$  with that at  $(k, l)$  as

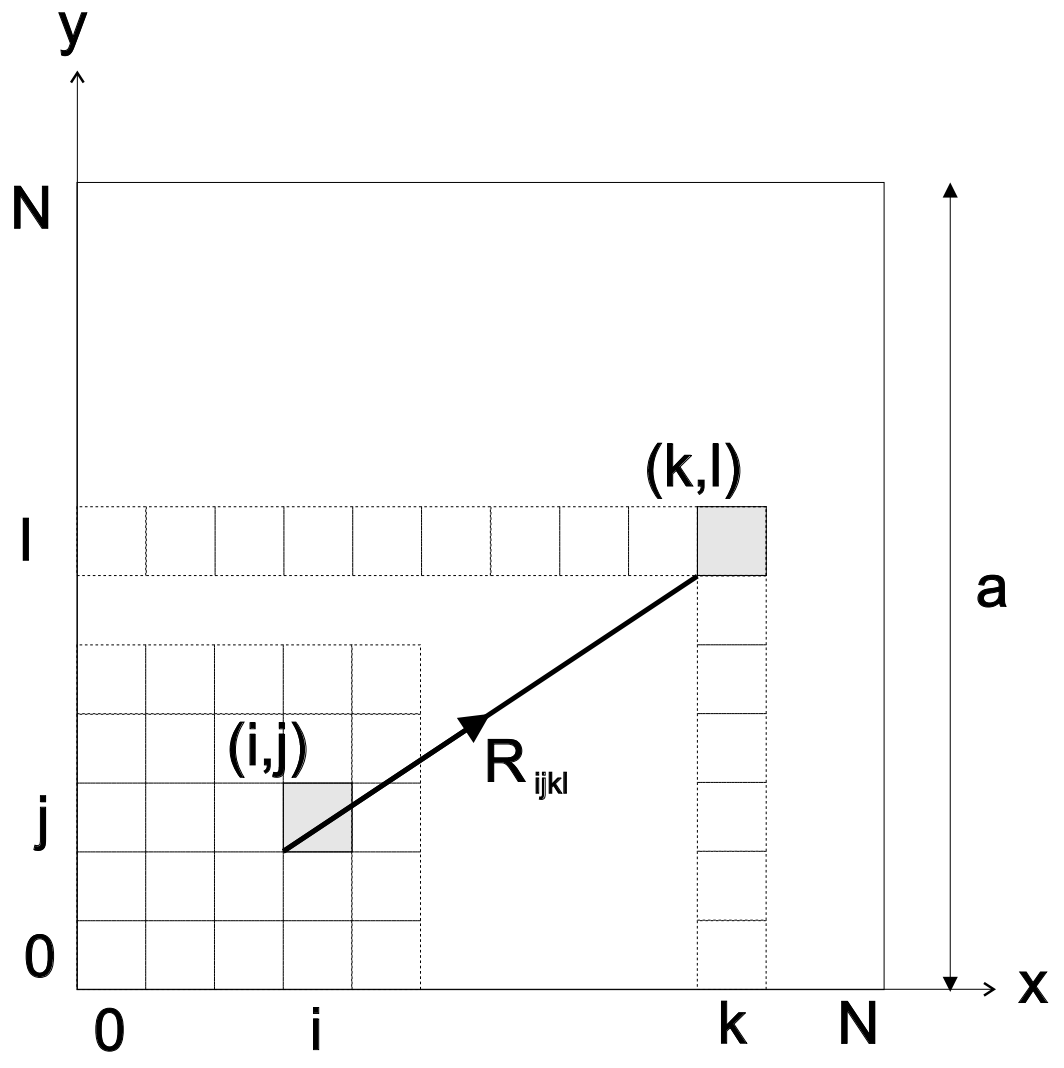


Figure 9.2: Diagram of the geometry for the case of a square homogeneously magnetized platelet.

$$\begin{aligned}
U_{ijkl}^{\perp} &= \frac{M^2}{4\pi\mu_0 r_{ijkl}^3} \\
&= \frac{I^2 h^4 t^2}{4\pi\mu_0 [(kh - ih)^2 + (lh - jh)^2]^{3/2}}.
\end{aligned} \tag{9.1}$$

One can write a similar expression for the case when the magnetization lies parallel to the plane in the x-direction. Using Equation (6.24) again, this gives

$$\begin{aligned}
U_{ijkl}^{\parallel} &= \frac{-3M^2}{4\pi\mu_0 r_{ijkl}^3} \left( \frac{x_{ijkl}^2}{r_{ijkl}^2} - \frac{1}{3} \right) \\
&= \frac{-3M^2 x_{ijkl}^2}{4\pi\mu_0 r_{ijkl}^5} + U_{ijkl}^{\perp}.
\end{aligned} \tag{9.2}$$

This expression may be expanded as

$$U_{ijkl}^{\parallel} = \frac{-3I^2 h^4 t^2 (kh - ih)^2}{4\pi\mu_0 [(kh - ih)^2 + (lh - jh)^2]^{5/2}} + U_{ijkl}^{\perp}. \tag{9.3}$$

Substituting  $t = h$ , this yields the expression

$$U_{ijkl}^{\parallel} = \frac{-3I^2 h^8 (k - i)^2}{4\pi\mu_0 h^5 [(k - i)^2 + (l - j)^2]^{5/2}} + U_{ijkl}^{\perp}. \tag{9.4}$$

The total energy for the platelet may then be calculated by summing over all  $i, j, k$  and  $l$  ( $i \neq k, j \neq l$ ) thus:

$$\begin{aligned}
U^{\parallel} &= \frac{1}{2} \sum_{\substack{i, j, k, l = 0 \\ i \neq k, j \neq l}}^{N-1} U_{ijkl}^{\parallel} \\
&= -\frac{3I^2 h^3}{8\pi\mu_0} \sum_{\substack{i, j, k, l = 0 \\ i \neq k, j \neq l}}^{N-1} \frac{(k - i)^2}{[(k - i)^2 + (l - j)^2]^{5/2}} + U^{\perp}
\end{aligned} \tag{9.5}$$

where

$$U^\perp = \frac{1}{2} \sum_{\substack{i, j, k, l = 0 \\ i \neq k, j \neq l}}^{N-1} U_{ijkl}^\perp \quad (9.6)$$

and therefore the energy density may be obtained by dividing through by the volume of the platelet  $V = a^2t = N^2h^3$  to give

$$E^\parallel = -\frac{3I^2}{8\pi\mu_0} \left( \frac{1}{N^2} \right) \underbrace{\sum_{\substack{i, j, k, l = 0 \\ i \neq k, j \neq l}}^{N-1} \frac{(k-i)^2}{[(k-i)^2 + (l-j)^2]^{5/2}}}_{W_1} + E^\perp. \quad (9.7)$$

From Equation (6.40) we see that

$$E^\parallel - E^\perp = E(\pi/2) - E(0) = K \quad (9.8)$$

and hence we can write our final expression for K as

$$K = -\frac{3I^2}{8\pi\mu_0} W_1. \quad (9.9)$$

where  $W_1$  is the term indicated in Equation (9.7).

**9.2.2.2 Implementation, results and conclusion of tile model calculation.** The ratio of  $K_D/K$  is given as

$$\frac{K_D}{K} = \frac{I^2}{2\mu_0} \cdot \frac{8\pi\mu_0}{3I^2W_1} = \frac{4\pi}{3W_1}. \quad (9.10)$$

Using a Fortran-77 program running on a Pentium 150 MHz PC under MS-DOS 6.22 and Salford FTN77 to perform the explicit summations for  $W_1$

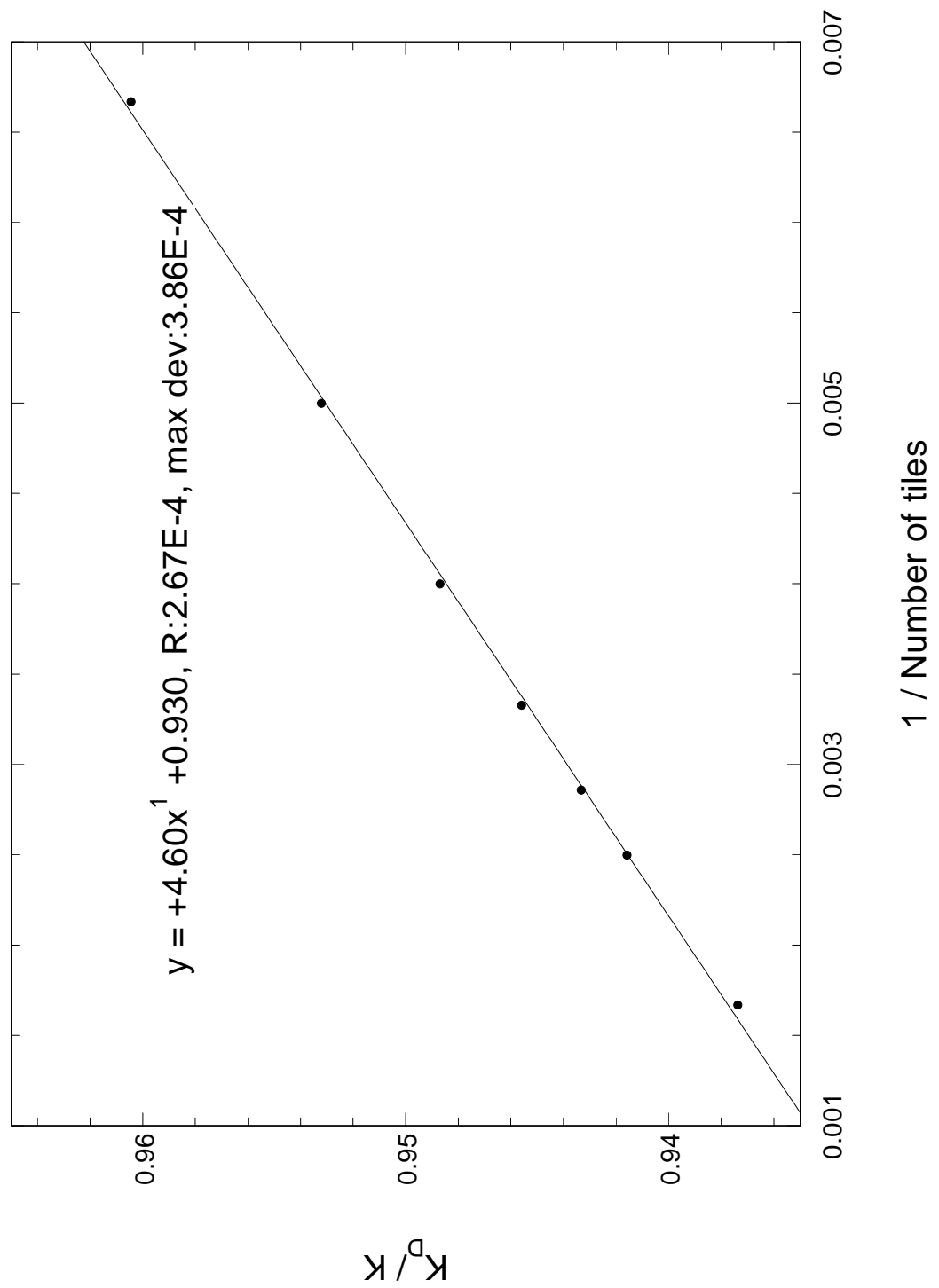


Figure 9.3: Fitted values of  $K_D/K$  vs.  $1/(\text{number of tiles } N)$

at a number of values of  $N$  over the range of values  $N=150 \dots 600$ , results for  $K_D/K$  are obtained and summarized in Figure 9.3. It may be seen from Figure 9.3 that the asymptotic value as  $N \rightarrow \infty$  of  $K_D/K$  is about 0.93, corresponding to a value for  $K$  of  $-1.65 \times 10^5 Jm^{-3}$ . This is a very satisfactory result, since Equation (6.24), which is in general use in magnetism, is in fact only the first term in an infinite series expansion of  $U_{ijkl}$  for small but finite dipoles, some of them touching each other [94].

### 9.2.3 Ion-by-ion calculation using KFILM

The program KFILM was used to calculate the dipolar and single-ion contributions to the uniaxial magnetic anisotropy constant  $K_1$  using explicit ion-by-ion summation for a perfect infinite single-crystal film. The computational effort involved was minimized by using a simulation cell which was as small as possible in the plane of the film ( $n_a = n_b = 1$ ), thereby taking maximum advantage of the periodic boundary conditions. The height of the simulation cell was chosen to be large enough ( $n_c = 40$ ) to avoid interactions between the film and its periodic copies in the c-direction by making this height considerably larger than the maximum cutoff radius used in the summation for the dipolar contribution. All of the tests outlined in this section were performed in this simulation cell.

**9.2.3.1 Calculation of dipolar anisotropy.** A set of explicit ion-by-ion summation calculations were performed using the KFILM program for films whose thickness was an integer number of unit cells, stacked on top

of each other with c-axis perpendicular to the film plane (thickness of one layer =  $c = 23.182 \text{ \AA}$ ). As expected for a film of finite thickness, the calculated extrapolated value for the dipolar anisotropy does not vary with film thickness as the cutoff radius tends to infinity (see Figure 9.4). The graph shows that all of the curves are tending towards a value of  $K_1$  of about  $-1.60 \times 10^5 Jm^{-3}$  as the cutoff radius tends to infinity. The rate of convergence of the result with respect to the cutoff radius is much faster than in the bulk case. The value itself,  $K_1 = -1.60 \times 10^5 Jm^{-3}$ , is very close to the value of  $K = -1.65 \times 10^5 Jm^{-3}$  obtained from the ‘tile’ model.

While it may be argued that this calculation suffers from the same potential problem with the validity of the approximation implicit in Equation (6.23) as the ‘tile’ model, in this method the distance between the dipoles is *fixed* by the crystal structure and hence cannot become arbitrarily small. The explicit summation therefore provides a better estimate of the dipolar contribution.

**9.2.3.2 Calculation of surface anisotropy** The single-ion contribution to the anisotropy of an infinite perfect film was calculated for a range of film thickness (in a similar way to the dipolar calculations described in the previous section). The results were then plotted as a function of ( $1/\text{film thickness}$ ), along with the corresponding dipolar contribution and the total anisotropy (Figure 9.5).

The values for the single-ion anisotropy fit a straight line very well over the entire tested range of film thicknesses. The dipolar contributions showed

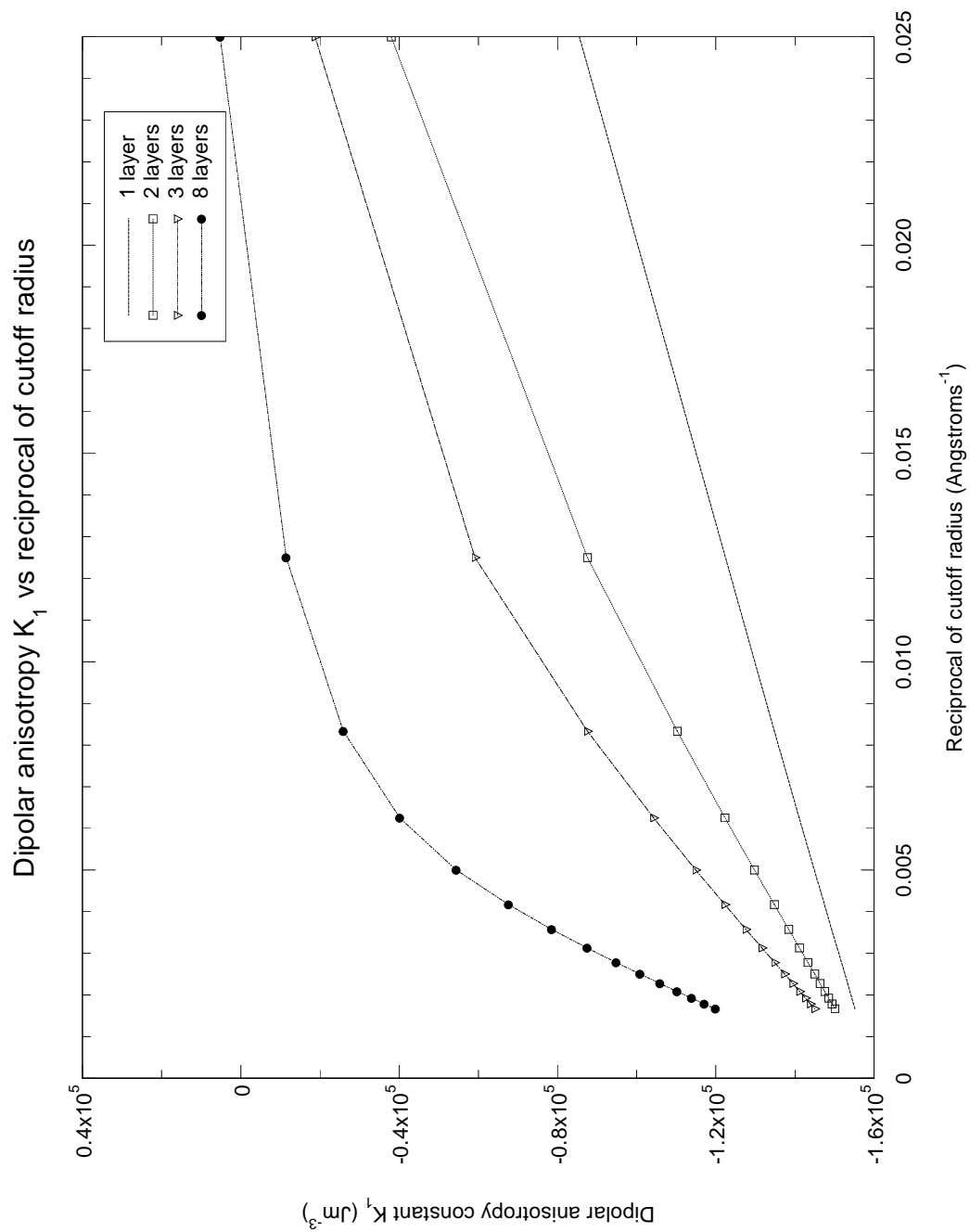


Figure 9.4: Dipolar contributions to the anisotropy as a function of the reciprocal of the cutoff radius for a number of different thicknesses of film.

a non-linear dependence on thickness. This may be understood by recognising that the calculated dipolar contribution of the anisotropy itself has two contributions: that arising from the magnetostatic shape anisotropy of the film (negative), and that arising from the intrinsic properties of the hexagonal crystal structure (positive). It may be seen from Figure 9.5 that for very thin films, the magnetostatic shape anisotropy ( $-1.6 \times 10^5 Jm^{-3}$ ) is dominant (marked on the graph by a dotted line). With increasing thickness of the film, the hexagonal structure-based bulk anisotropy increasingly contributes, and in the limit of infinite thickness should approach the bulk value (calculated in Section 9.1.2 as  $+1.738 \times 10^4 Jm^{-3}$ ). This is confirmed by a least-squares straight-line fit to the leftmost five points on the dipolar curve in Figure 9.5, which gives the extrapolated intercept to be  $+2.1 \times 10^4 Jm^{-3}$ , which broadly in agreement with the expected value.

**9.2.3.3 Investigation of the effect of cell cutting** The dipolar and single-ion contributions to the total anisotropy of a single layer of a perfect film (effectively ‘cut’ from a larger crystal) were calculated and plotted as a function of where in the structure the layer was cut. The strategy used was to create a number of possible unit cells, each one differing from the next by exactly where in the structure the origin of the unit cell was chosen to be. In practice, this was achieved by shifting the contents of the conventional unit cell (for which the origin lies on the 2a site) in the c-direction by varying amounts and ‘wrapping round’ those atoms which moved through the { 0001 } faces of the unit cell. The variation of the dipolar and single-ion

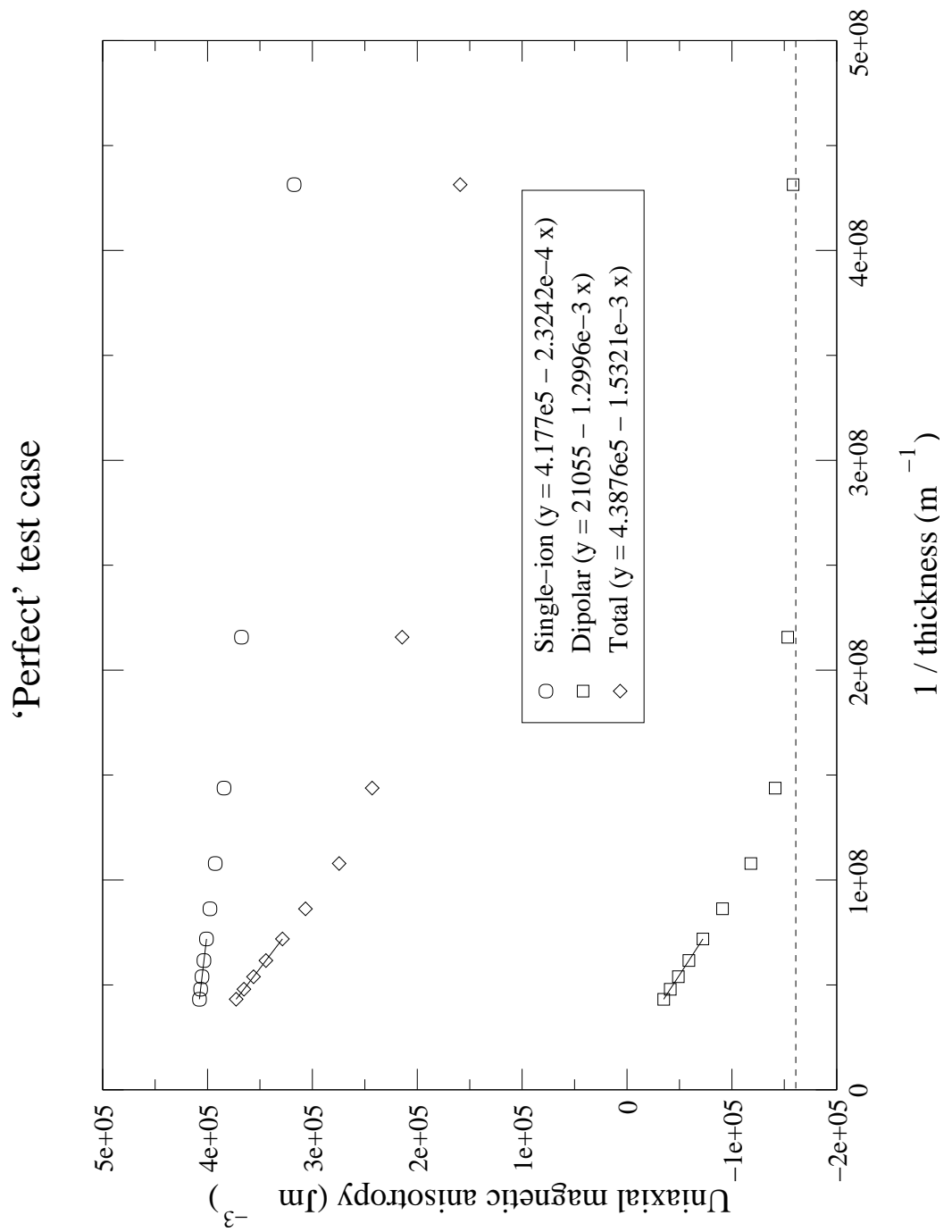


Figure 9.5: Volume and surface contributions to the total anisotropy for a perfect crystalline thin film.

contributions with the amount of shifting is shown in Figure 9.6.

Note that of the two types of contribution, the single-ion anisotropy shows the most sensitive dependence on shift, with a shift corresponding to putting the 2b and 12k sites on the surface giving the smallest and largest anisotropies respectively. The dipolar anisotropy appears to show less variation with shift, peaks appearing when the 2a and 12k sites are on the surface, with all other possible shifts giving very similar values.

It was also observed that the calculated anisotropies showed less variation with shift as the thickness of the slab was increased. This is expected, since the surface to volume ratio decreases as the thickness increases.

#### **9.2.3.3.1 Surface and volume anisotropies of shifted variants**

This analysis was performed over a range of film thicknesses (using just the single-ion contribution) for a number of different shifted variants of the unit cell. The values of the surface anisotropy  $K_S$  varied over quite a range (see Figure 9.7), and were mostly negative, but one was found to be positive (2b sites on surface). Also, all of the cases gave a value for the single-ion contribution to the volume anisotropy of  $K_V = 4.18 \times 10^5 Jm^{-3}$ , which is in excellent agreement with the previous results calculated for the bulk.

### **9.3 Magnetic anisotropy of a finite perfect film**

The effect of having a film which is finite in the plane of the substrate was examined. This was achieved using the optional ability of KFILM to set additional non-spherical cutoffs for the dipolar summation in the form of

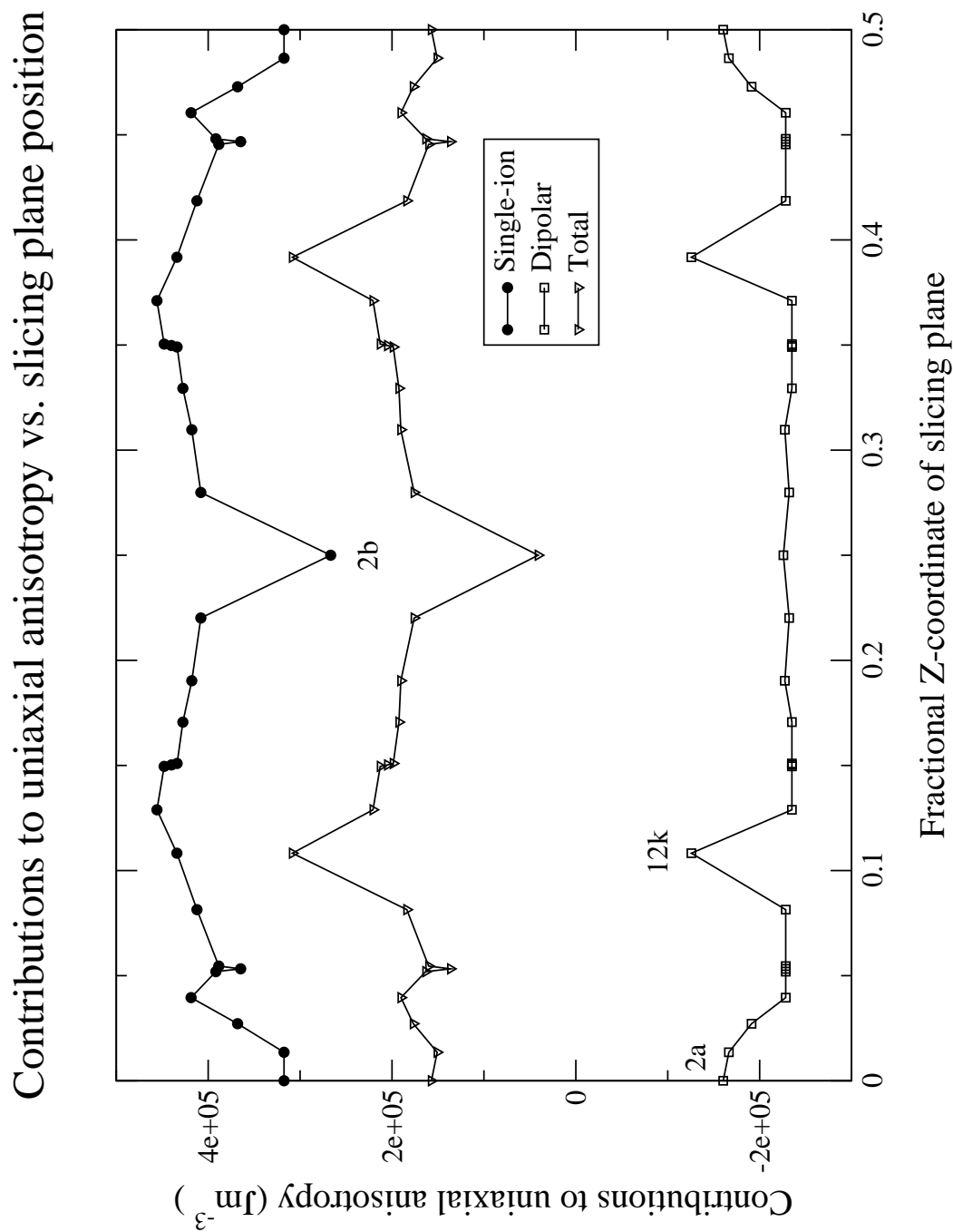


Figure 9.6: Dependence of the dipolar and single-ion anisotropy contributions on the position of the slicing plane for a 1-layer thick film.

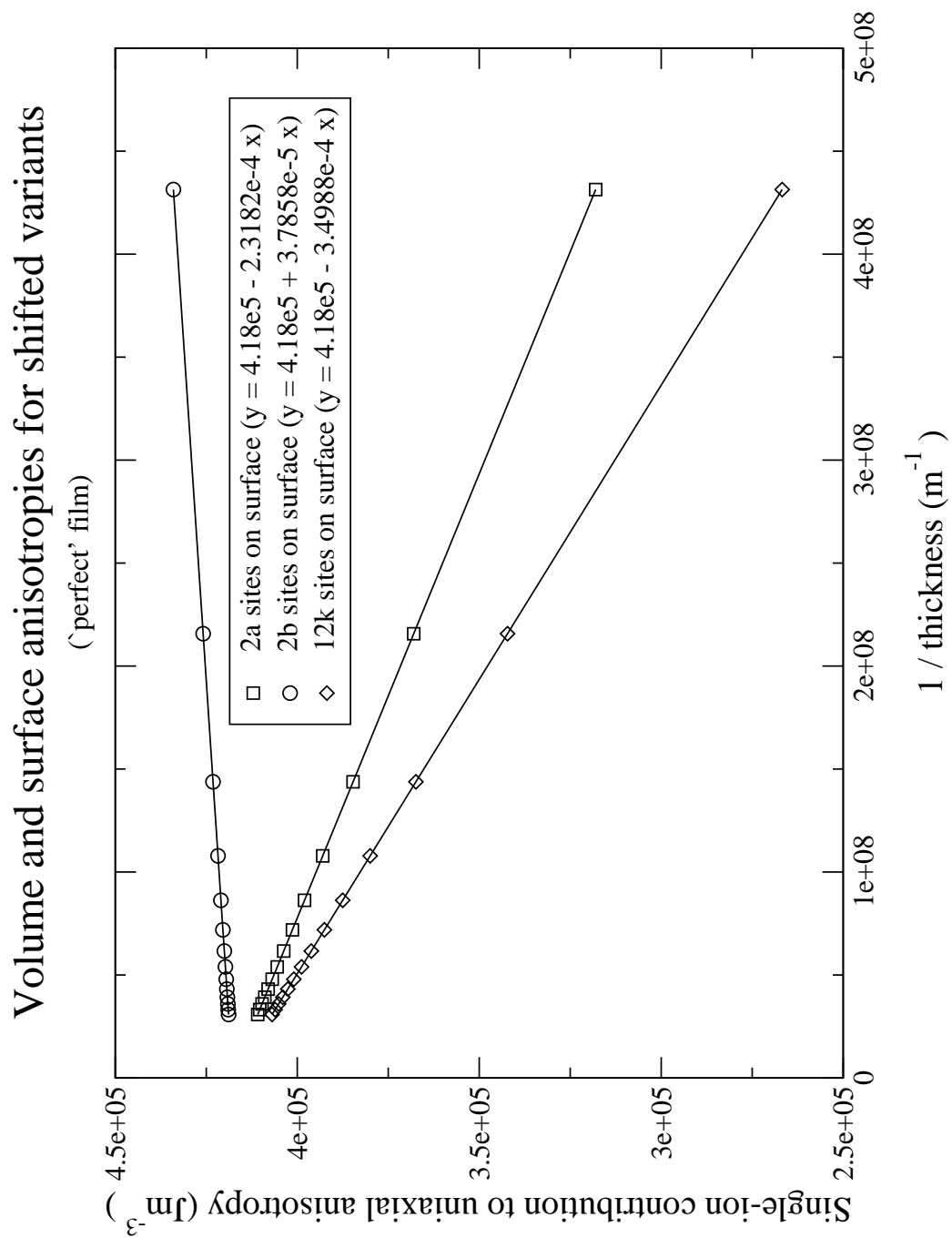


Figure 9.7: Single-ion surface and volume anisotropy contributions for a number of shifted variants of the unit cell

minimum and maximum values (in Å) of  $x$ ,  $y$  and  $z$  (representing the position of dipole  $j$  in the summation formula), where these coordinates form an *orthogonal* Cartesian frame with the origin at the centre of the simulation cell. In effect, this provides the ability to confine the dipolar summation to a cuboidal volume centred on the simulation cell. Care must be taken, however, that the outer (spherical) dipolar cutoff radius is set large enough so as not to reject any candidate interactions within the cuboidal volume.

Cutoffs were chosen in the plane of the film so as to model a square platelet of side 300 Å, and the film thickness was varied over the range  $n_{\text{layers}} = 1 \dots 14$ , the simulation cell being of size  $(1 \times 1 \times 40)$ . The outer dipolar cutoff radius was also set to 1000 Å so as to include the whole of the platelet in the dipolar summation sphere. The dipolar contributions to the anisotropy are shown in Figure 9.8, and the variation of both contributions and the total anisotropy with increasing slab thickness is shown in Figure 9.9.

It may be seen from Figure 9.9 that while the single-ion contribution is always positive, the dipolar contribution starts off negative for thinner layers and only becomes positive when the thickness of the slab is greater than or equal to 14 layers. This corresponds to a square platelet which is as thick as it is wide, i.e. a cube of material. This behaviour can be compared with that of the infinite perfect film described earlier - in the limit of a very thin film, the dipolar contribution tends towards the predicted value for the magnetostatic shape anisotropy in the same way as for the infinite perfect film. As the platelet gets thicker, the intrinsic component of the

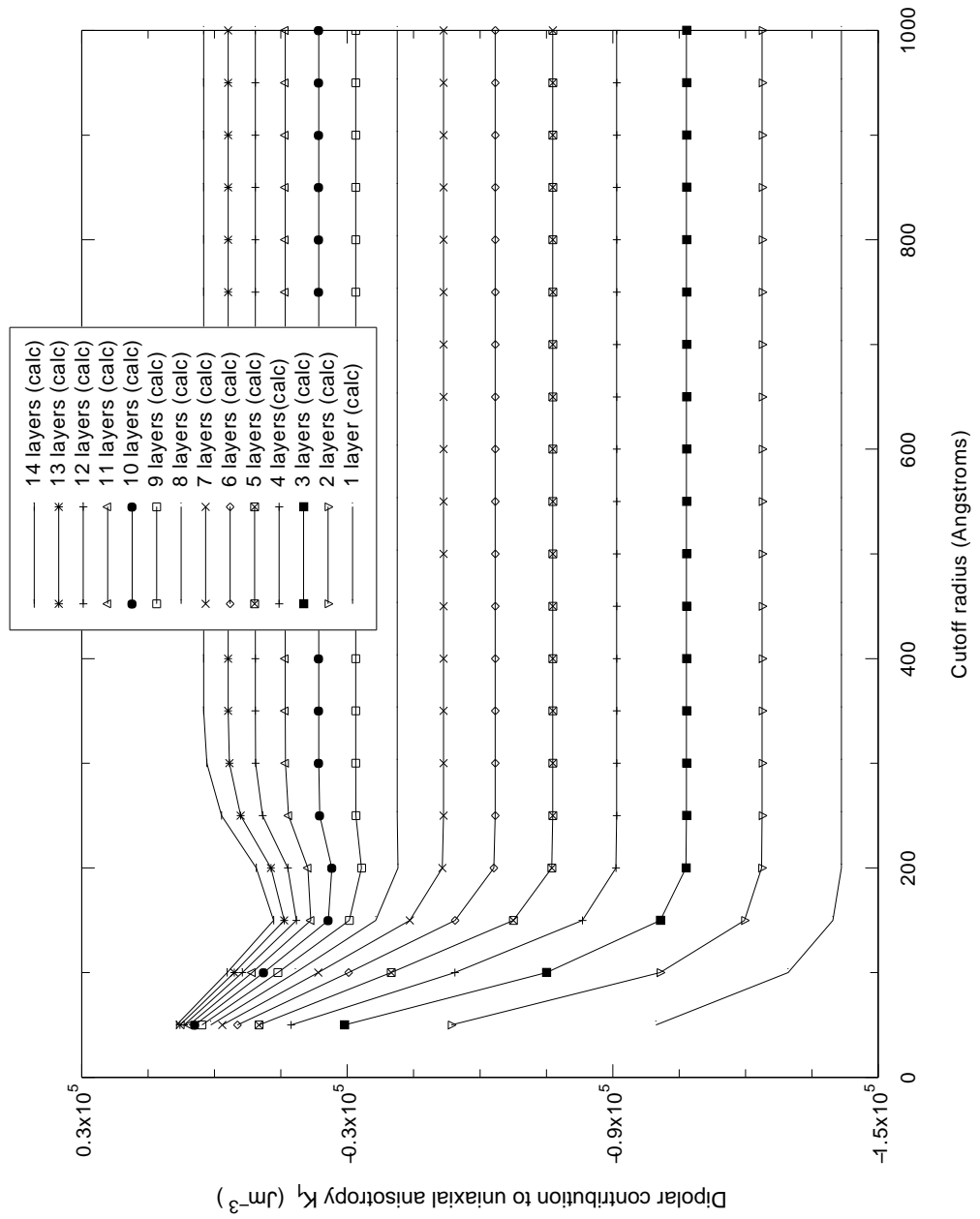


Figure 9.8: Dipolar anisotropy contributions for a finite slab and a range of slab thicknesses

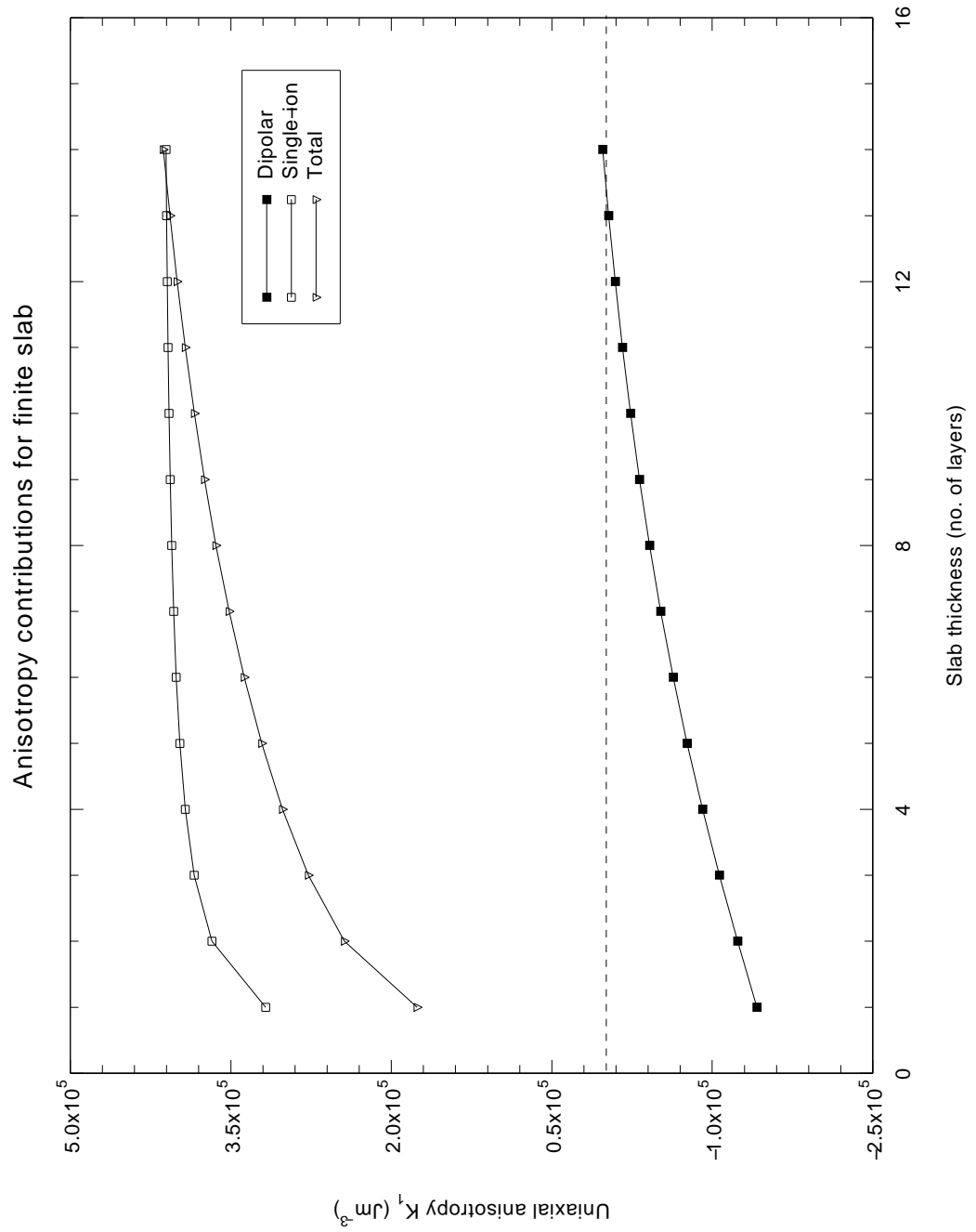


Figure 9.9: Individual and total anisotropy contributions over a range of slab thicknesses

dipolar contribution associated with the hexagonal crystal structure begins to dominate.

## **9.4 High-memory vs. low-memory: a comparison of strategies for large-scale anisotropy simulations**

The calculations of the single-ion and dipolar contributions to the uniaxial anisotropy can require substantial computational resources in cases where large systems (containing many magnetic ions) are simulated. It is therefore useful to ascertain the maximum size of model system which can be practically considered, given the finite constraints of computer memory and CPU time. Another issue which frequently arises when developing large computer simulations is whether intermediate results which may be needed more than once in a program run should be calculated once, stored and then recalled when required, or re-evaluated from scratch (possibly many times over) when necessary. Both of these strategies have benefits and drawbacks for the overall efficiency of the simulation, and the most efficient strategy will depend critically on the exact nature of the calculation and the relative speeds and capacities of the physical components of the computer on which the simulation is run. In anticipation of the application of the anisotropy calculation program KFILM to the results of large-scale thin film growth simulations performed by DEPOSIT, investigations into how these issues affect the calculation of the single-ion and dipolar anisotropy contributions were carried out and are described below.

### **9.4.1 Discussion of memory issues**

Two possible strategies for carrying out large-scale simulations (in which there are a large number of magnetic ions in the simulation cell) suggest

themselves. The first (here called the ‘high-memory’ strategy) is to precompute and store in arrays the position coordinates and total occupancies of every magnetic ion site in the simulation cell. These arrays can then be handed over to the subroutines which compute the single-ion and dipolar contributions, which use a single- and double (nested) loop over the sites respectively in their summations, and thus requiring execution times of  $O(N)$  and  $O(N^2)$  respectively. For large systems, these arrays will require a lot of memory to store, as there are four double-precision numbers associated with each site. In this case, very large simulations will incur large time overheads associated with ‘paging’ storage used by the program to a swap file once the storage needed exceeds the physical RAM capacity of the computer.

The alternative ‘low-memory’ strategy is not to store these vast arrays of site data all at once, but to only generate the details of the interacting site(s) when required, by replacing the loops over sites with loops over growth units plus small ‘inner’ subsidiary loops over all the sites in each growth unit. This obviously adds complexity to the program but, used in conjunction with the ‘mean-field’ model mentioned earlier, yields a calculation scheme which is much more economical on memory, making very large scale simulations feasible. The drawback with this strategy is that it requires more computer time, which is undesirable when results need to be correlated from a large number of different runs using many different sets of input data.

#### 9.4.2 Single-ion and dipolar strategy comparison

In order to investigate this trade-off between memory usage and run time, ‘high-memory’ and ‘low-memory’ versions of the KFILM program were constructed along the lines described above. The programs were compiled using as many of the optimization features of the compiler as possible. The execution time of the programs were compared using a set of film structure input files which contained known numbers of growth units. The results are shown in Figure 9.10, along with fitted curves of quadratic form.

The results fit the expected quadratic form very well. It can be seen that the run times for the ‘low-memory’ program are consistently a little under twice as long as for the ‘high-memory’ program with the same input data. A run-time limit of one CPU-week was chosen, which, when the fitted curves shown in the graph are extrapolated, gave maximum practical system sizes for the ‘high’ and ‘low’ memory strategies of around 2400 and 1500 growth units respectively. Since the ‘high-memory’ version of the program used in this test was dimensioned to allow a maximum of 2000 growth units to be considered, it is clear that the memory usage is not a significant barrier on the computer used for these calculations. The more scarce and critical resource is simply CPU time. For this reason, the ‘high-memory’ version of the program was chosen for future use in calculating the total anisotropy.

#### 9.4.3 Single-ion only strategy comparison

A similar test was carried out using high- and low-memory versions of the program which evaluated *only* the single-ion part of the anisotropy. The

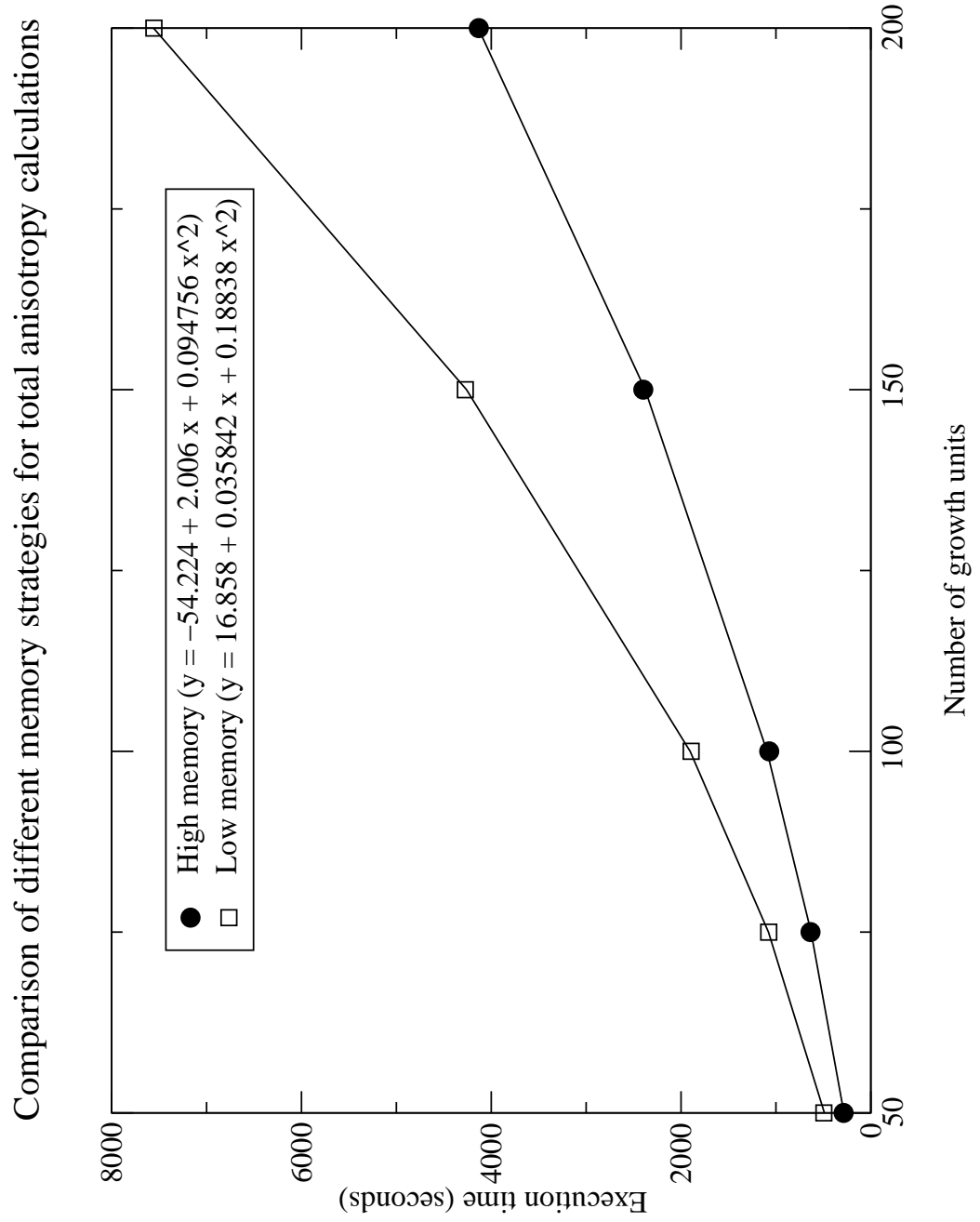


Figure 9.10: Execution time vs. system size for two computation schemes with differing memory requirements for the total anisotropy.

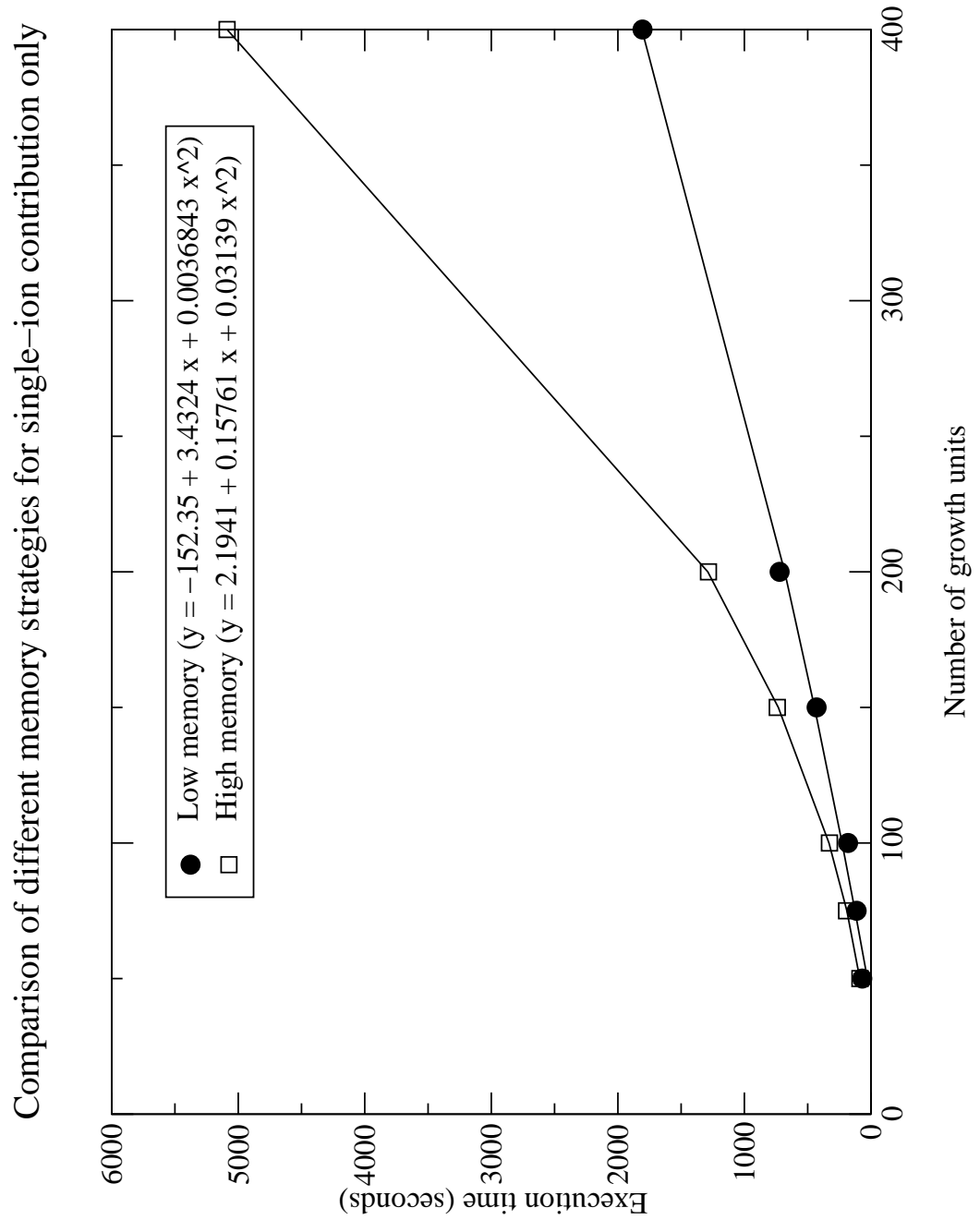


Figure 9.11: Execution time vs. system size for two computation schemes with differing memory requirements for the single-ion contribution only.

results are shown in Figure 9.11. It may be seen from this figure that in this case it is the 'low-memory' strategy which is the most efficient.

## 9.5 Structural aspects of simulated deposited films

A number of investigations were undertaken to establish the dependence of the structure of the simulated deposited film on the process parameters. The process parameters fall into the two distinct categories outlined below.

### 9.5.1 Time-related parameters

The first class of simulation parameters is those related to the passage of time in the deposition simulation. The simulations use an arbitrary unit of time (the ‘tick’), and the duration of deposition runs is specified using this unit. The prefactor  $\nu_0$  in the Arrhenius rate equation (7.1) corresponds to an attempt frequency for diffusion events. Experimental diffusion studies for single atoms on metal thin films [95] have suggested a value for this attempt frequency of around  $10^{12} - 10^{13}$  Hz - so far no such measurement has been performed for hexaferrite thin films. In light of the lack of experimental data, and in the interests of keeping the simulation parameters dimensionless, we have therefore set  $\nu_0 = 1$  in all our simulations.

The deposition flux  $F_{dep}$  corresponds to the rate per unit area at which new growth units are added to the simulation cell. The units used are the Number of discrete growth units added per gridcell surface area per tick. The overall deposition rate  $R_{dep}$  of new growth units is therefore calculated in the simulation using the formula

$$R_{dep} = N_a N_b F_{dep} \quad (9.11)$$

where  $N_a$  and  $N_b$  are the dimensions (in gridcells) of the simulation cell in

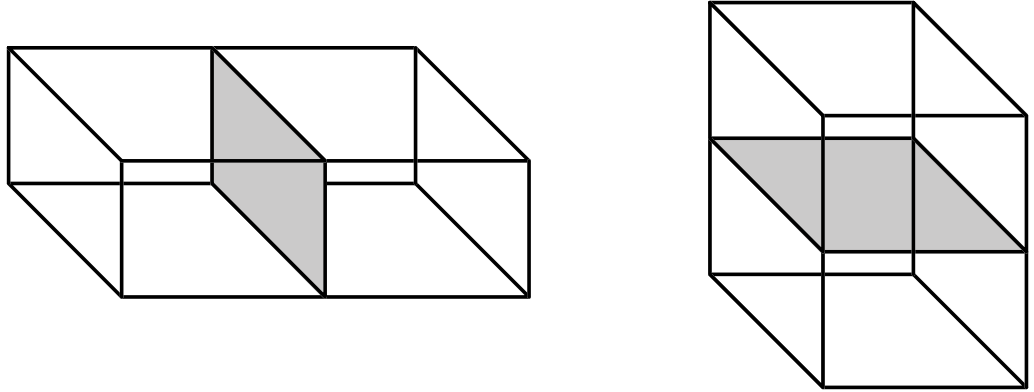


Figure 9.12: Geometry for evaluation of barrier energies  $E_{aa}$  and  $E_{cc}$ .

the a- and b-directions respectively.

### 9.5.2 Energy-related parameters

The second class of simulation parameters is those related to the barrier energies and the temperature of the system. The latter, which effectively corresponds to the temperature at which the substrate material is held during film growth, was assumed to be constant during each deposition run and uniform throughout the system. In the Arrhenius equation (7.1), this factor appears multiplied by the Boltzmann constant  $k_B$  in the denominator of the expression in the exponential. In all of the simulations considered, the value of  $k_B T$  was taken to be unity in the interests of simplicity.

Estimates of the magnitude of the energy barriers  $E_{aa}$  and  $E_{cc}$  were obtained by taking the structural data for the hexagonal unit cell of the ferrite and treating it as an assembly of point charges, each ion  $i$  being represented by a location  $\mathbf{r}_i = (x_i, y_i, z_i)$  in 3-D Cartesian coordinates and a corresponding charge  $q_i$  equal to the nominal charge state of that ion (i.e. for an  $\text{Fe}^{3+}$

ion,  $q = +3e$ , and for an  $O^{2-}$  ion,  $q = -2e$ , where  $e$  is the electronic charge). The overall electrostatic energy of an assembly of  $N_{\text{ions}}$  point charges was therefore calculated from the conventional Coulomb expression

$$E_{\text{electrostatic}} = \frac{1}{4\pi\epsilon_0} \sum_i^{N_{\text{ions}}} \sum_{j \neq i}^{N_{\text{ions}}} \frac{q_i q_j}{|\mathbf{r}_i - \mathbf{r}_j|^2}. \quad (9.12)$$

The following energies were calculated (see Figure 9.12):

$E_0$  - the electrostatic energy of the contents of a single isolated unit cell,

$E_{2a}$  - the electrostatic energy of two immediately neighbouring unit cells which are contiguous along the crystallographic  $a$ -direction (i.e. share a common  $\{100\}$  face),

$E_{2c}$  - the electrostatic energy of two immediately neighbouring unit cells which are contiguous along the crystallographic  $c$ -direction (i.e. share a common  $\{001\}$  face).

The energy barrier parameters  $E_{aa}$  and  $E_{cc}$  were therefore evaluated as

$$E_{aa} = 2E_0 - E_{2a} \quad (9.13)$$

$$E_{cc} = 2E_0 - E_{2c}. \quad (9.14)$$

The values obtained from these calculations were  $E_{aa} = 116.45$  eV and  $E_{cc} = 47.05$  eV, giving a ratio  $E_{aa}/E_{cc} = 2.48$ . While these calculated energies are probably not as accurate as those which could be provided by *ab initio* electronic structure codes, and are about two orders of magnitude larger than those measured for single metal atoms on perfect metal crystal surfaces (see,

e.g. [96]), we are more interested in the ratio of these energies than their absolute values, for reasons outlined below.

Allowance was made in the simulation program to substitute a different value  $E_{sub}$  for  $E_{cc}$  when the growth unit being considered is in the first layer, i.e. sitting directly on the substrate material, since there is a strong possibility that the diffusion rates for the first layer will be different from those in succeeding layers. This will be particularly true when the film is being grown on a different material to that being deposited. In all of the simulations considered here, however,  $E_{sub}$  was set equal to  $E_{cc}$ .

### 9.5.3 Choosing a realistic energy barrier ratio $p$

The energy barrier contributions  $E_{aa}$  and  $E_{cc}$  are effectively measures of the ‘stickiness’ of growth units when stacked on top of or beside each other. The overall energy barrier to diffusion is defined additively in terms of these values. The relative tendency of growth units to stick together in these two ways was therefore quantified using the ratio  $p = E_{aa}/E_{cc}$ . A number of tests were performed using various values of  $p$  and  $E_{cc} = 1.0$ , measuring the overall number of hopping and reorientation events in the course of a test simulation run. The deposition flux was set so that one new growth unit was deposited into the simulation cell per unit time. The results are shown in Figure 9.13. It can be seen from Figure 9.13 that the greatest part of the variation of the amount of diffusion and reorientation which takes place in the course of a simulation takes place in the range  $p = 0.1 \dots 10$ . This therefore defines a region in the phase space of the process parameters which

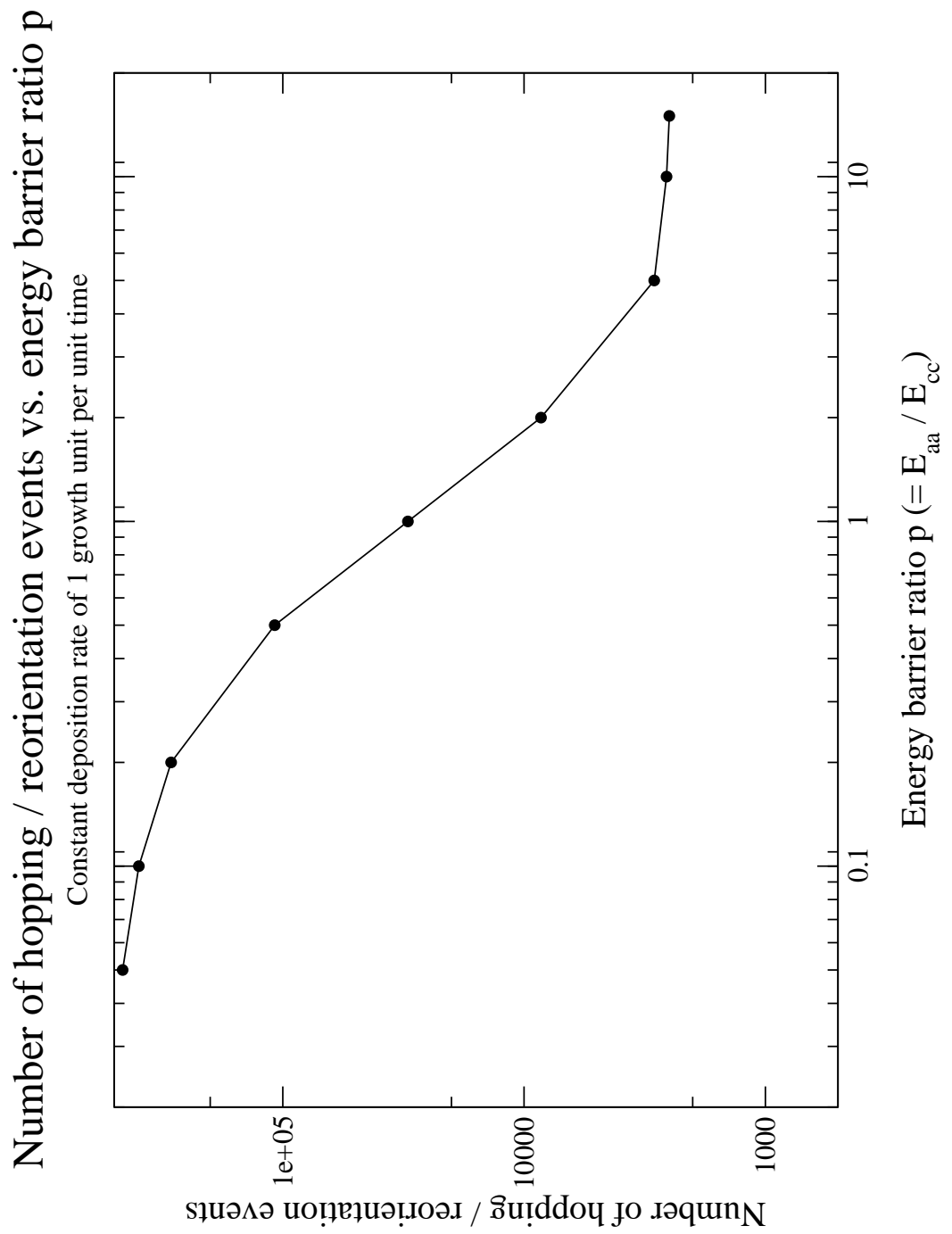


Figure 9.13: Variation of number of hopping/reorientation events with energy barrier ratio  $p$ .

is likely to provide the richest variation in film structure. The approximate Coulomb results mentioned in the previous section also lie in this range, and other workers in the field [97, 98] have used growth parameters lying within this range. Values of  $p < 0.1$  also correspond to prohibitively long program run times, while for  $p = 100$  no hopping or reorientation events were observed during the entire simulation run. Accordingly, values of  $p$  in the range  $p=0.1 \dots 10$  were used in all of the growth simulations described in later sections.

#### **9.5.4 Definition of the three test regimes for anisotropy simulation**

The variation of the magnetic properties with film structure (and hence with the film growth parameters) was investigated by choosing three test cases which were representative of three different growth regimes. The three test cases were calculated in a  $(10 \times 10 \times 25)$  simulation cell, and the incoming flux of deposited growth units was varied along with the deposition time so that the product (flux  $\times$  deposition time) was a constant, i.e. enough material to grow a film 10 layers thick. The flux was held constant during each deposition run, along with the energy barrier parameters which were set to  $p = 0.2$ ,  $E_{cc} = 5.0$ . Two realizations of each (deposited) test case were used - more were not attempted due to the very heavy demands placed by the anisotropy calculations on available computer processing time. The three test cases used were:

**‘Granular’ case** This case corresponded to a high input flux and short deposition time, which yielded a ‘granular’ film, with many voids and a rough surface, due to the evolving film not having enough time to re-order itself by diffusion processes.

**‘Smoother’ case** This case corresponded to a input flux 100 times lower than for the ‘granular’ case, with the deposition time larger by the same factor. This set of conditions permitted a much greater degree of re-ordering by diffusion, yielding a film with significant fewer voids and a less disordered surface.

**‘Perfect’ case** The test case was artificially constructed using a small supplementary computer program, rather than generated using DEPOSIT. In this case perfect crystalline layers of growth units with uniform orientation were laid down one by one, yielding a perfect crystalline film. Only one realization of this test case was necessary.

#### **9.5.5 Time evolution of the growth of the simulated films**

DEPOSIT runs were performed for the three test cases described above. For each case, the deposition simulation was halted at intervals approximately corresponding to the deposition of a monolayer. The program FILMSTAT was then used to compute a number of instantaneous statistical properties of the growing film before the deposition recommenced. The FILMSTAT results are described below.

**9.5.5.1 Time evolution of average thickness and roughness** A quantitative study was undertaken of the time dependence of average thickness (the thickness being defined at each point on the film as the z-coordinate of the highest growth unit) and average roughness (defined as the RMS deviation from the average thickness). A simulation cell of size  $(30 \times 30 \times 30)$  was used, and 15 layers deposited using a range of values for the deposition flux ( $F_{dep} = 1.0$  [‘granular’ test case] to  $F_{dep} = 10^{-5}$  [‘smoother’ test case]). The other process parameters used were  $E_{cc} = 5.00$  and  $p = 0.2$ . Thickness and roughness values (averaged over the whole film) were calculated at monolayer intervals and the resulting values were averaged over a maximum of 300 simulation runs for each set of process parameters. Fewer runs were used in cases where the computing time for 300 runs exceeded the available limit. The results are shown in Figures 9.14 and 9.15. It can be seen from Figure 9.14 that as the incoming flux is reduced, the density of the growing film increases due to increased diffusion. Figure 9.15 shows that there is a transition between growth regimes which takes place between  $F_{dep} = 10^{-3}$  and  $F_{dep} = 10^{-5}$  - the greater importance of diffusion is reflected in a reduction of surface roughness.

**9.5.5.2 Time evolution of layer coverage** Coverage data for each layer in the film is shown in Figures 9.16 and 9.17 as a function of process time for the ‘granular’ and ‘smoother’ test cases respectively. The figures show that the ‘granular’ films do not achieve total coverage on a layer-by-layer basis, as the rate of diffusion of growth units is considerably smaller

Ratio (average film thickness / no. of monolayers deposited) vs. number of monolayers deposited

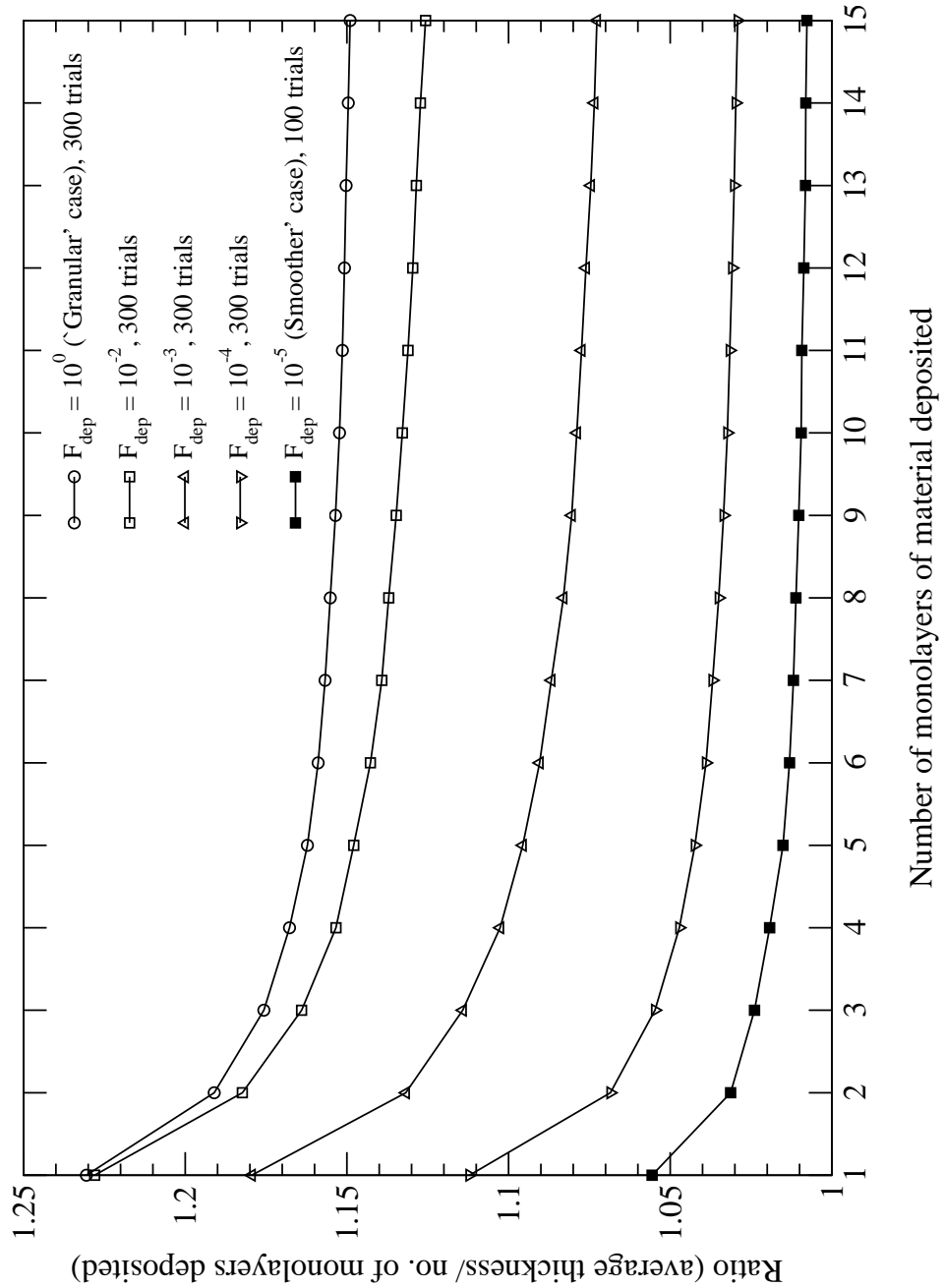


Figure 9.14: Ratio of average film thickness to number of monolayers deposited as a function of deposition time for a range of values of deposition flux  $F_{dep}$ . Results are averaged over 300 runs except where indicated.

Variation of average film roughness with average film thickness

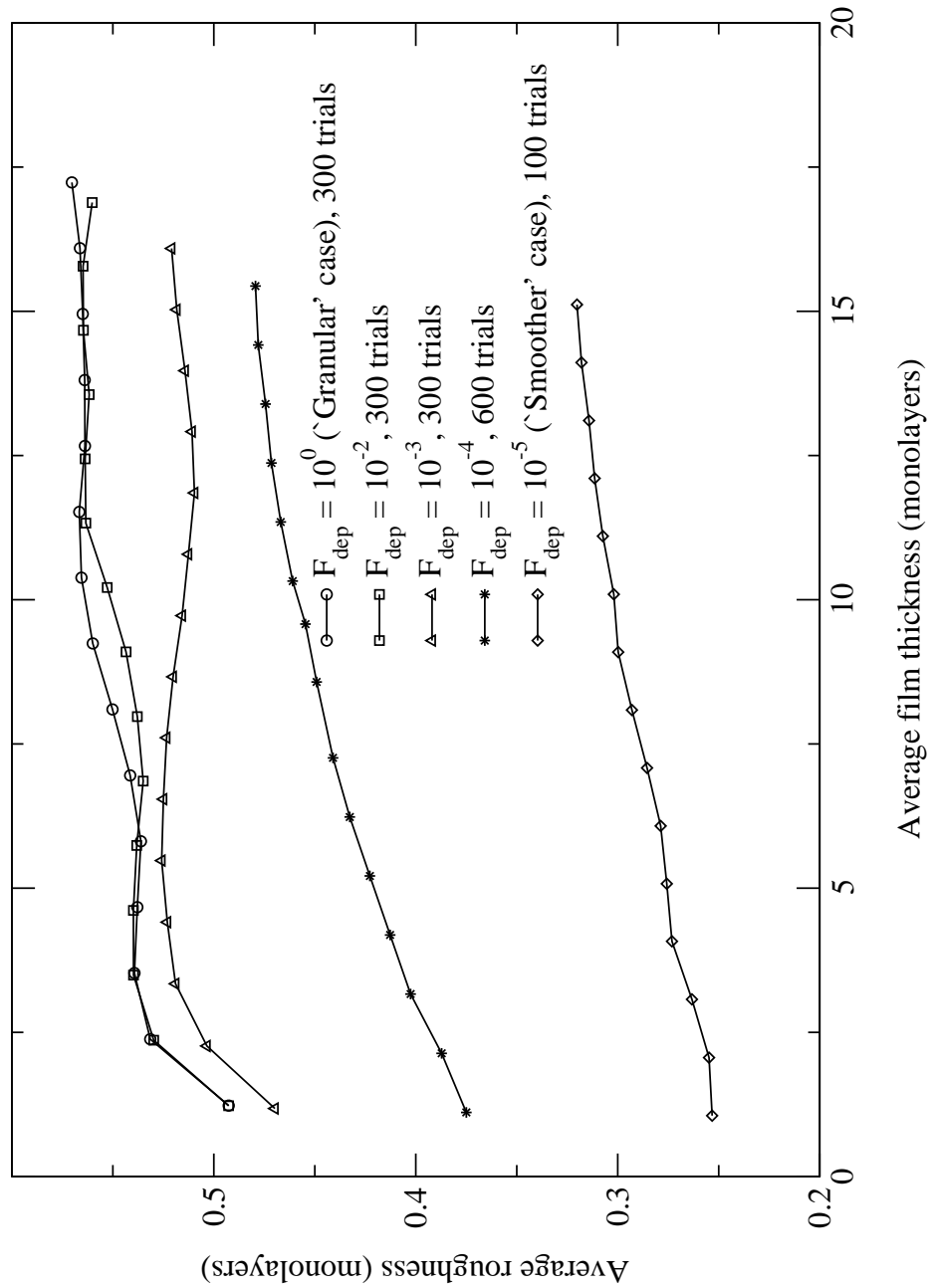


Figure 9.15: Average roughness as a function of average thickness for a range of values of deposition flux  $F_{dep}$ . Results are averaged over 300 runs except where indicated.

than the rate of deposition of new growth units. The ‘smoother’ film attains much higher layer coverages due to diffusion processes becoming more important. At the end of the deposition run, it can be seen that the ‘granular’ film has an approximately uniform density profile.

## **9.6 Comparison of simulated film with AFM measurements of a real film**

### **9.6.1 Description of model system, the heightfield output from FILMSTAT, and MATLAB script**

A very large model system was set up, using a simulation cell of size  $(170 \times 170 \times 25)$  (corresponding to a patch of film of side  $0.1\mu m$ ), and used as input to the deposition simulation. Two different sets of growth parameters were used, corresponding to the ‘granular’ and ‘smoother’ test cases defined earlier. The resulting film structures were processed using the FILMSTAT program to extract statistics and also create ‘height-field’ data sets. These height-fields consist of a large number of records (one per line of the data file), each record consisting of three numbers thus:

`X-coordinate Y-coordinate Height`

The X- and Y-coordinates correspond to a position in the plane of the film (the values being sampled on a square grid), and the height is the vertical coordinate of the uppermost growth unit at the corresponding position in the film plane. The height-fields were then visualized in a three-dimensional form using a specially-written MATLAB script.

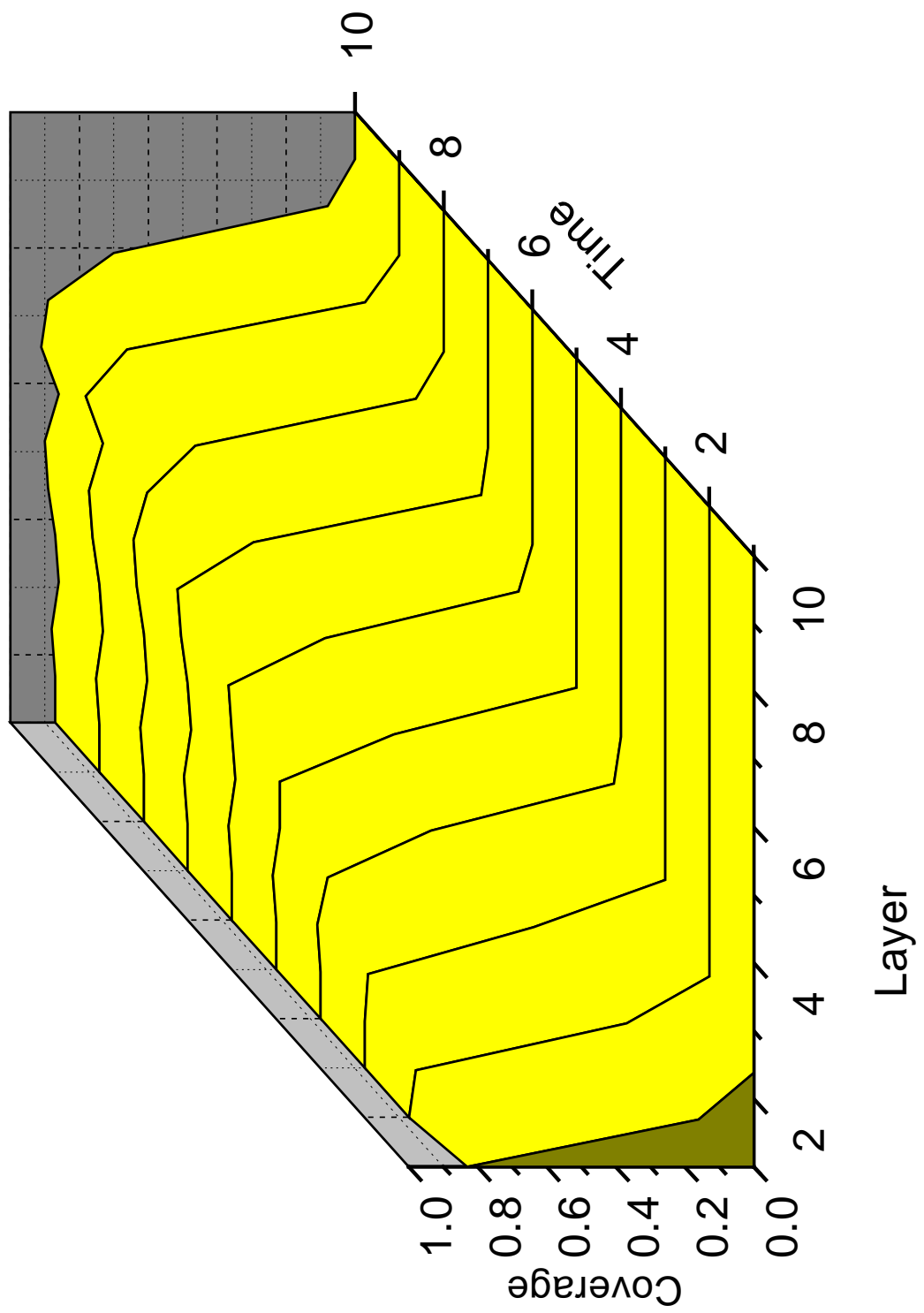


Figure 9.16: Time evolution of layer coverages for 'granular' test case

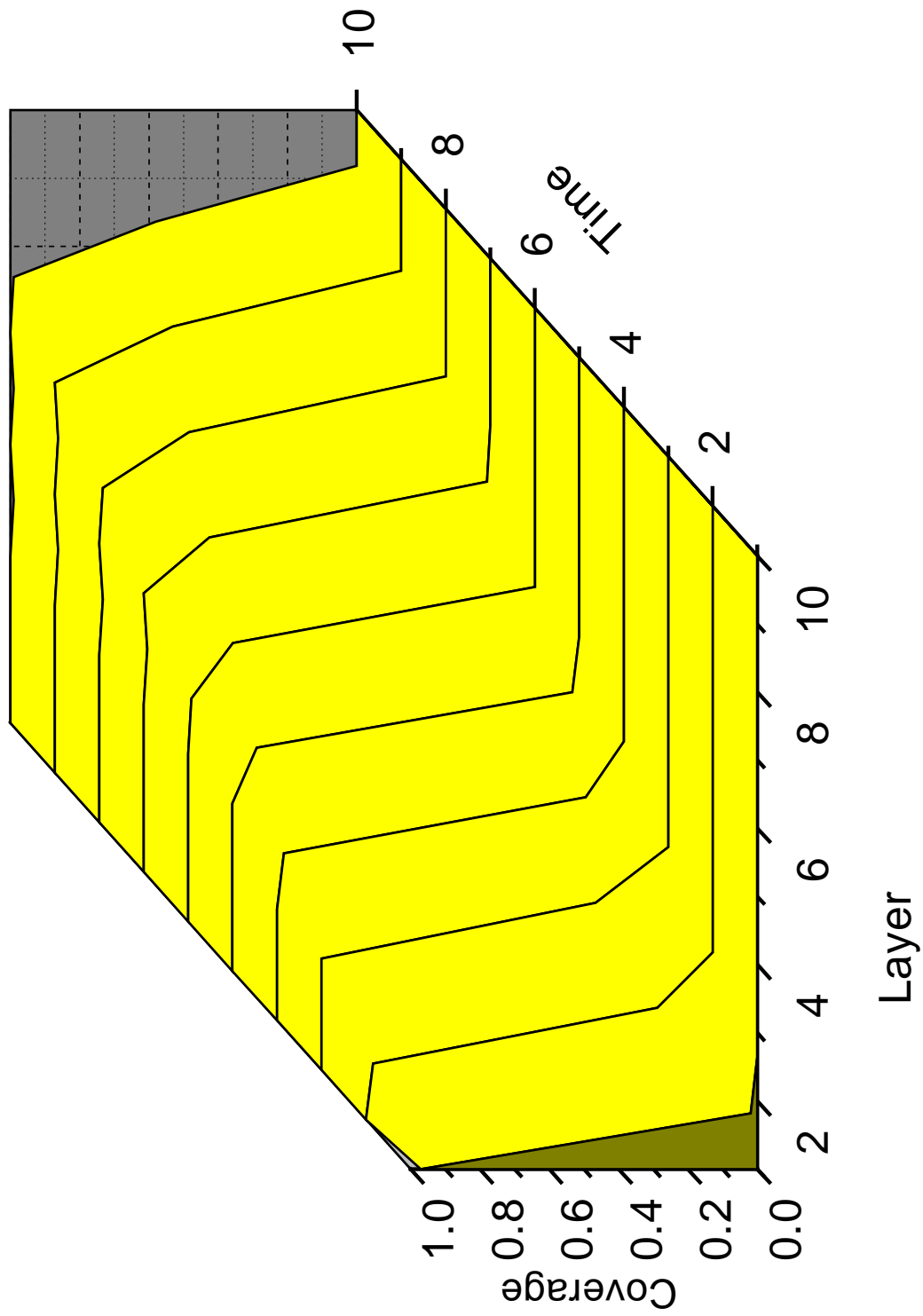


Figure 9.17: Time evolution of layer coverages for 'smoother' test case

### **9.6.2 Pictures and description of simulated films**

The results are shown in Figures 9.18 & 9.19. The former, corresponding to the ‘granular’ test case, clearly shows the highly disordered nature of the film, with many voids and a surface which is rough on very small length scales. The latter film, corresponding to the ‘smoother’ test case, consists of almost exactly the same number of growth units and can be seen to have a much more ‘compacted’ structure (compare the vertical length scales), with clearly visible islands sitting on a much more even surface.

### **9.6.3 Picture of experimental AFM data and comparison with simulations**

It is interesting to compare these views of the simulated films with topography data extracted from AFM (atomic force microscopy) measurements of a real film of M-type hexaferrite deposited using PLD techniques (see Figure 9.20). While the experimental data corresponds to a length scale in the film plane ten times larger ( $1\mu m$ ) than could be achieved in the simulations, the pictures are remarkably similar in character.

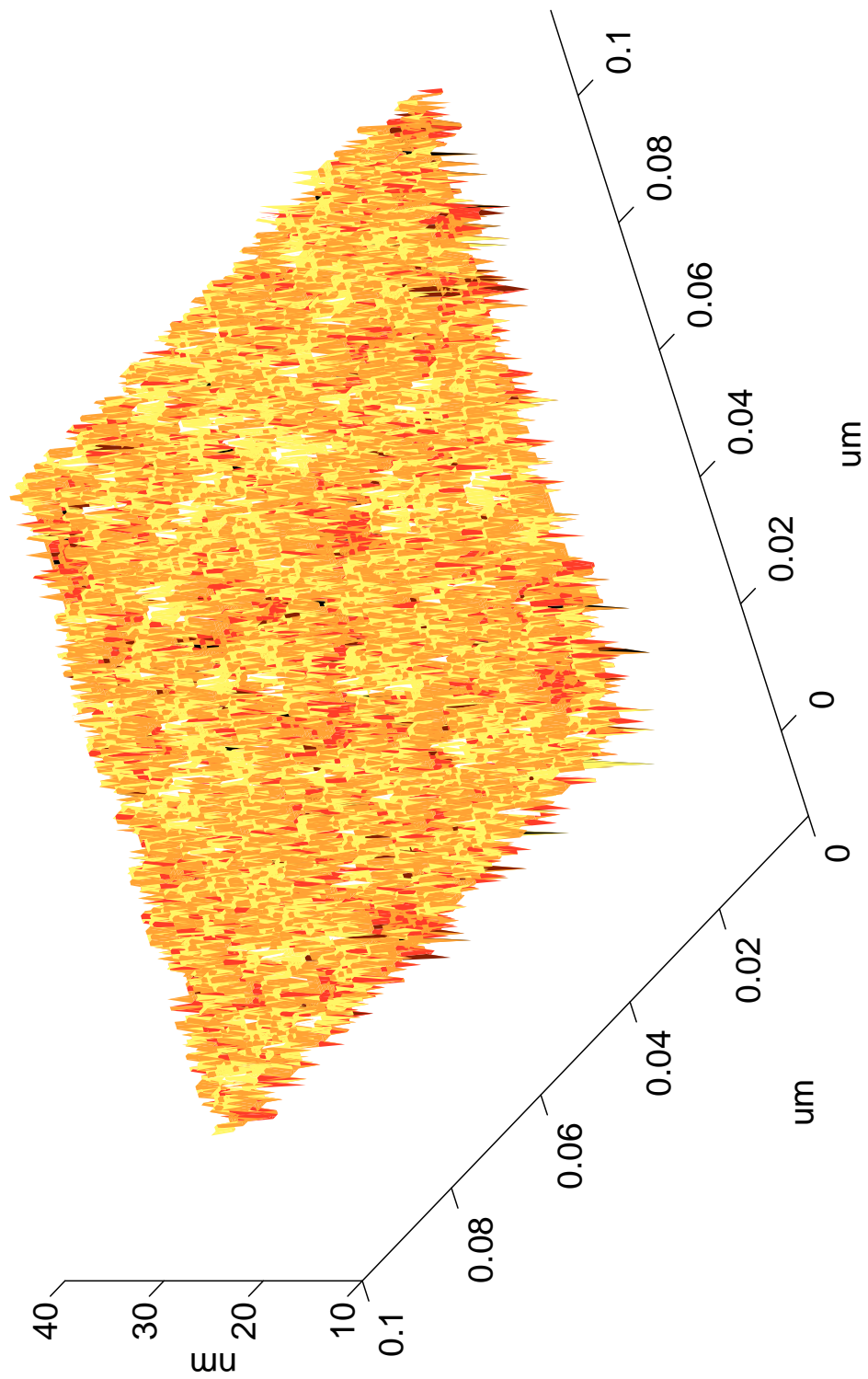


Figure 9.18: 3D view of heightfield corresponding to 'granular' test case

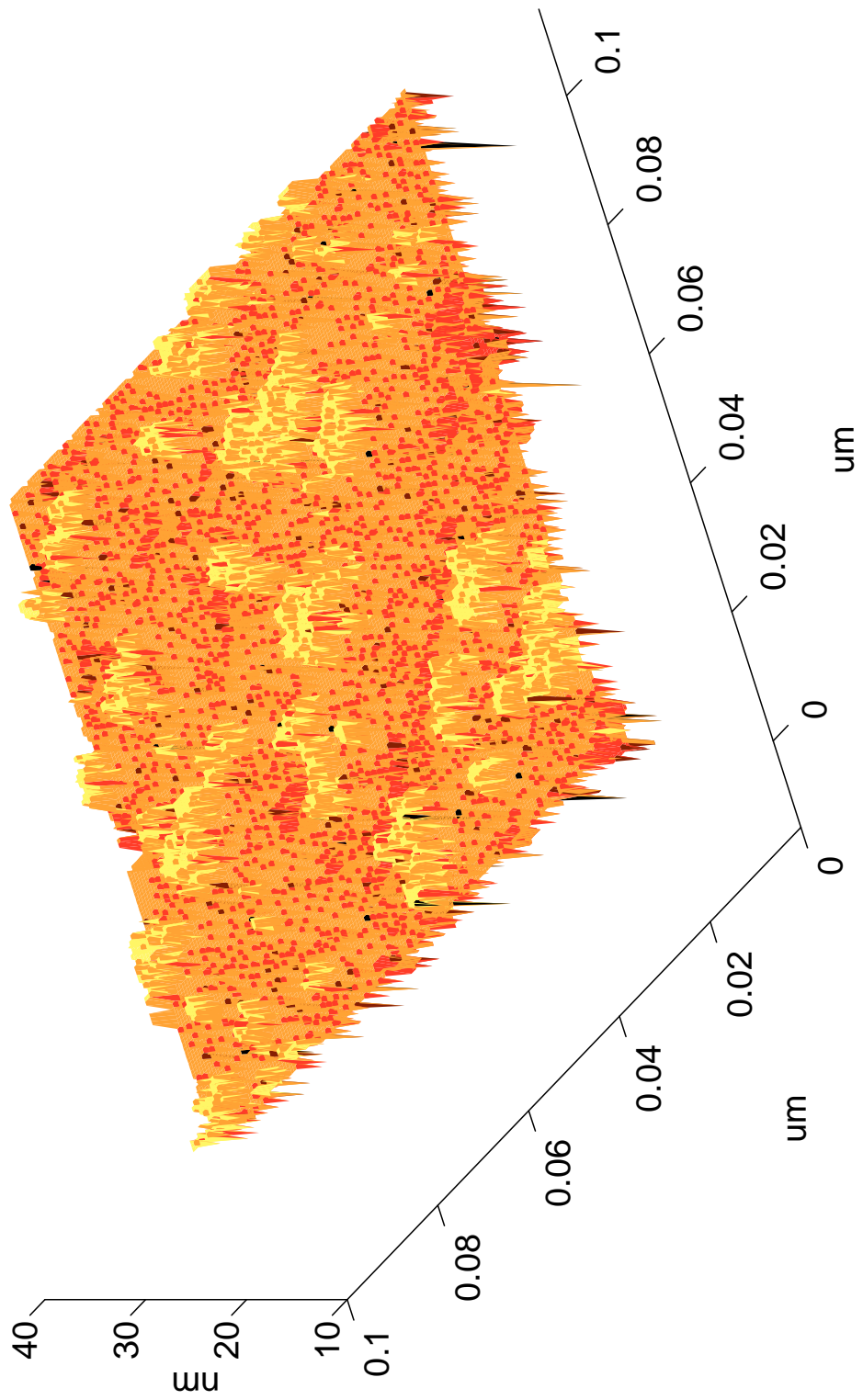


Figure 9.19: 3D view of heightfield corresponding to 'smoother' test case

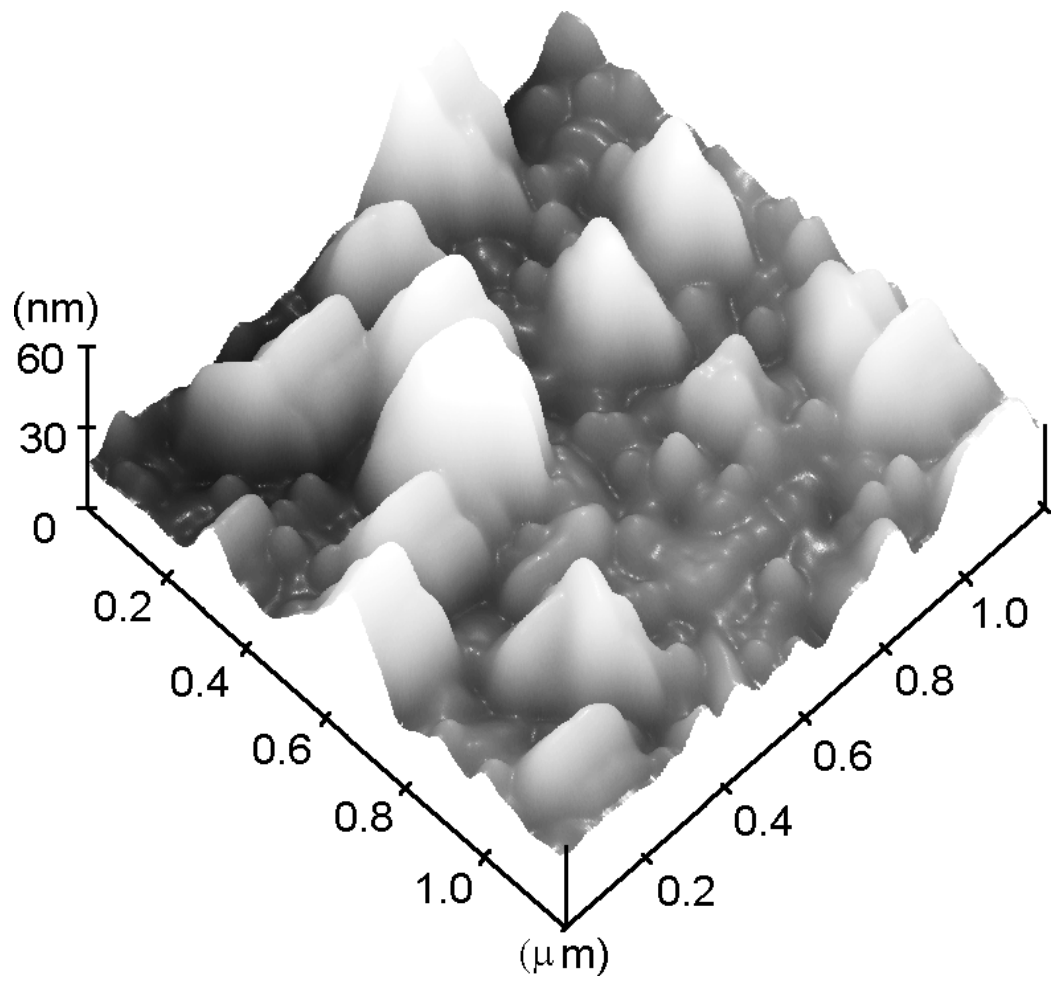


Figure 9.20: 3D view of heightfield data produced from AFM measurements of an M-type hexaferrite film grown using PLD techniques.

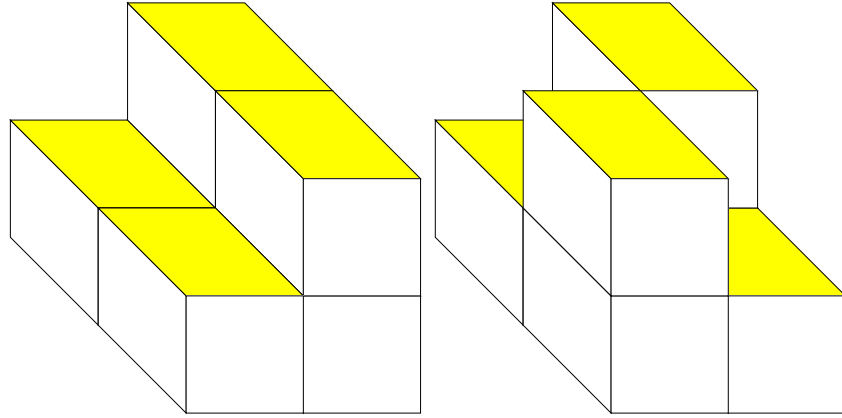
## **9.7 Application of the magnetic model to the simulated deposited films**

### **9.7.1 Methodology**

The deposition program DEPOSIT produces a file which contains all the structural details of the simulated film. This film is then read into the program KFILM in order to calculate the magnetic properties of the simulated film. The only other input required by KFILM is a value for the outer dipolar cutoff radius in Å, optional minimum and maximum values of  $x$ ,  $y$  and  $z$  if additional plane cutoffs are to be used, and some parameters which determine the verbosity of output in the results file.

### **9.7.2 Magnetic anisotropy of ‘patterned’ films**

Test cases were created in which the films had a pattern, using a  $(2 \times 2 \times 40)$  simulation cell. Two patterns were created, ‘stripe’ and ‘chessboard’, both of which effectively corresponded to a film thickness of exactly 1.5 layers (see Figure 9.21). Dipolar and single-ion contributions were calculated and the results are summarised in Table 9.3. The difference between the calculated total anisotropy values shows that surface patterning has a substantial effect in determining the overall anisotropy associated with the film.



(a) 'Stripe' pattern

(b) 'Chessboard' pattern

Figure 9.21: Repeating units for 'stripe' and 'chessboard' patterns.

	'Stripe '	'Chessboard'
Dipolar	-1.35673	-1.26881
Single-ion	2.17709	2.47764
Total	0.82035	1.20883

Table 9.3: Anisotropy contributions and total anisotropy for two different surface patterns for a simulated film of average thickness 1.5 monolayers. The anisotropy values are given in units of  $10^5 \text{ Jm}^{-3}$ .

	Single-ion contribution	Dipolar contribution	Total
Granular case	3.59	0.069	3.66
	3.62	0.047	3.66
Smoother case	4.18	0.231	4.41
	4.03	0.244	4.27
Perfect case	4.18	0.211	4.39

Table 9.4: Volume anisotropy for the three test cases in units of  $10^5 \text{ Jm}^{-3}$ .

### 9.7.3 Results for volume and surface anisotropies for the three regimes

For each test case, ten structure files were created, representing snapshots of the growing films after 1/10, 2/10, 3/10 etc. of the total deposition time had elapsed. Each of the film structure files created in this way were then used as input for the KFILM program to yield values for the single-ion and dipolar anisotropy contributions. The outer cutoff radius used in the calculation of the dipolar contribution was  $100 \text{ \AA}$ . The volume and surface anisotropies were then determined for each test case using the methods described earlier. The data for each test case are shown in Figures 9.22 – 9.26, and a summary of the derived values of volume and surface anisotropies are given in Tables 9.4 and 9.5.

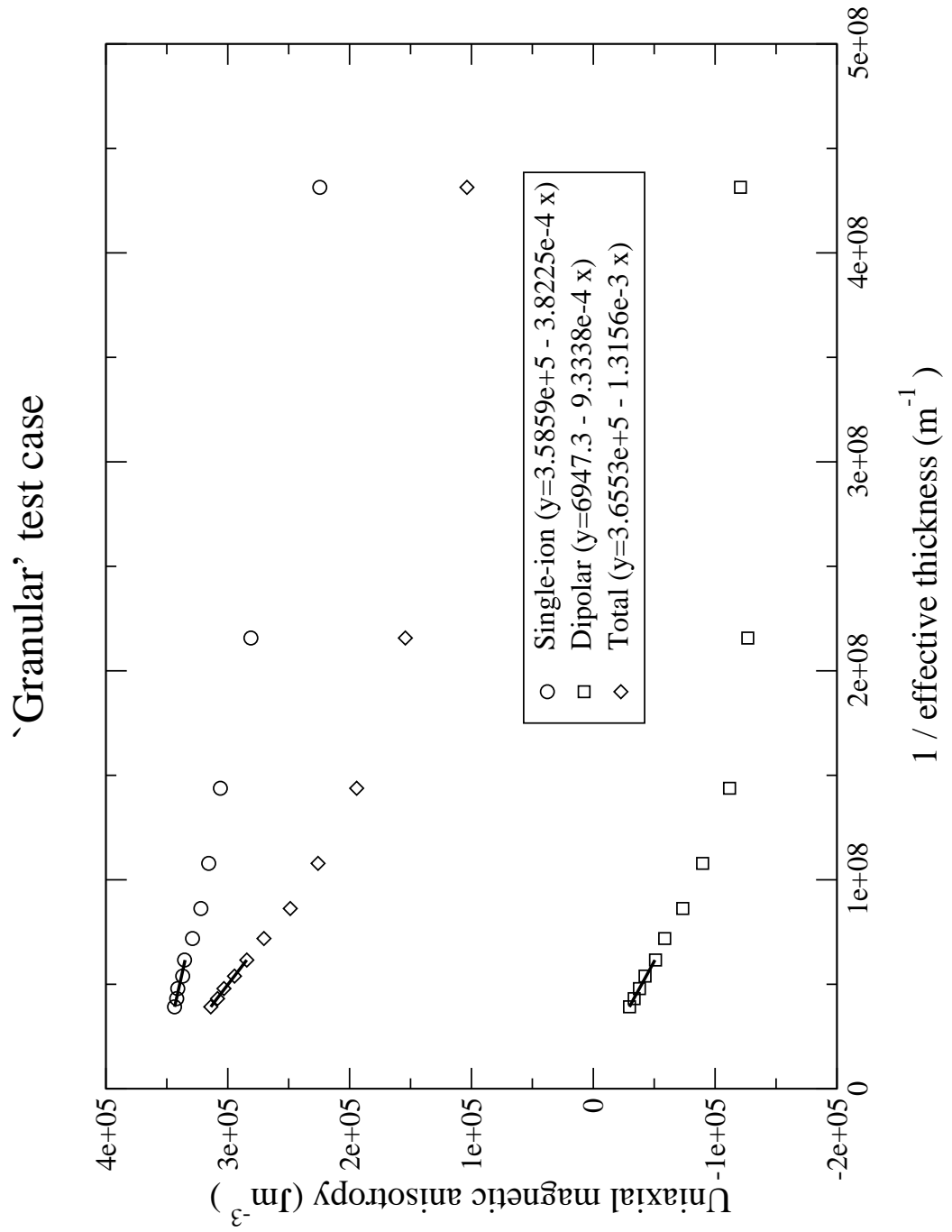


Figure 9.22: Surface and volume anisotropies for ‘granular’ test case

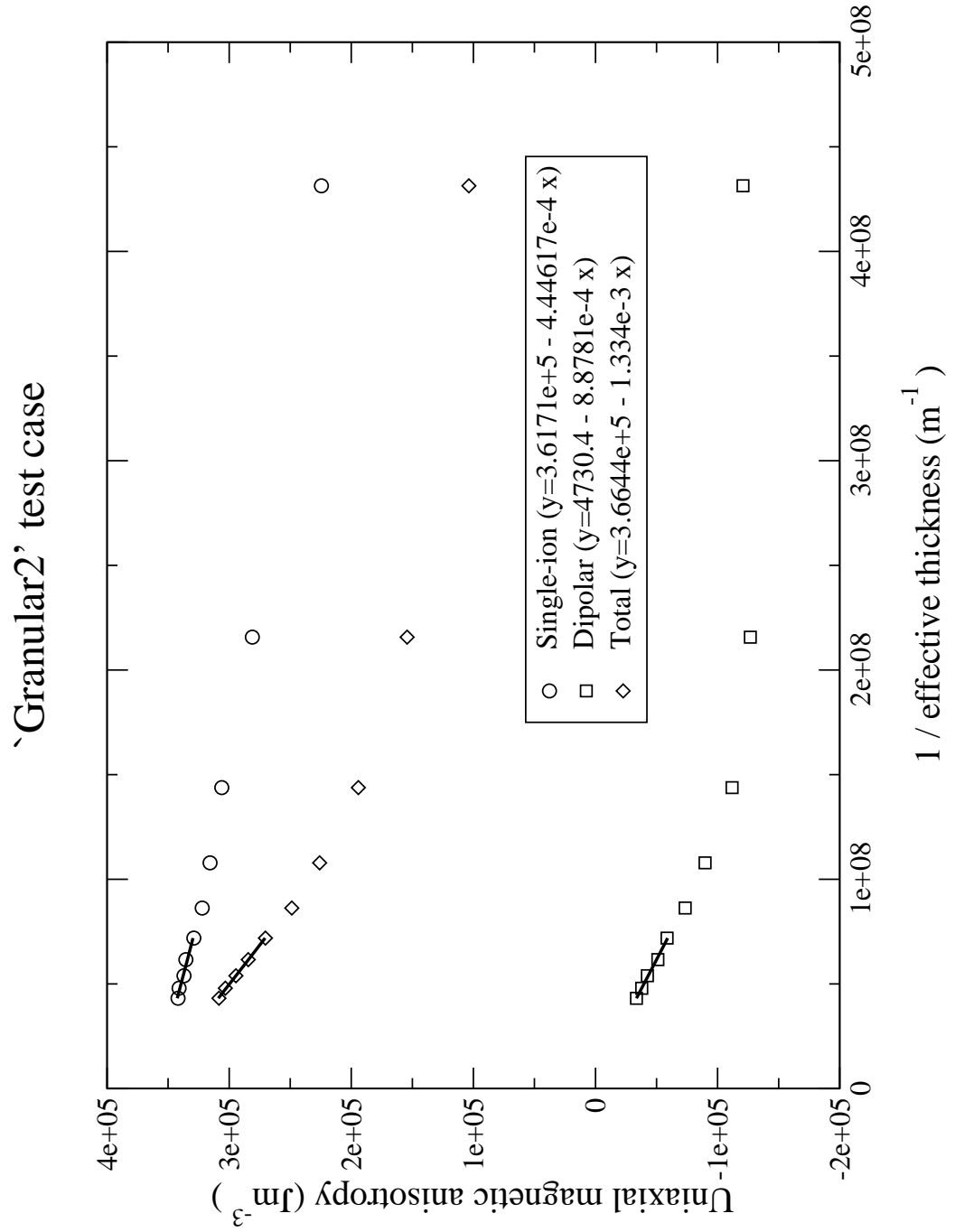


Figure 9.23: Surface and volume anisotropies for 'granular2' test case

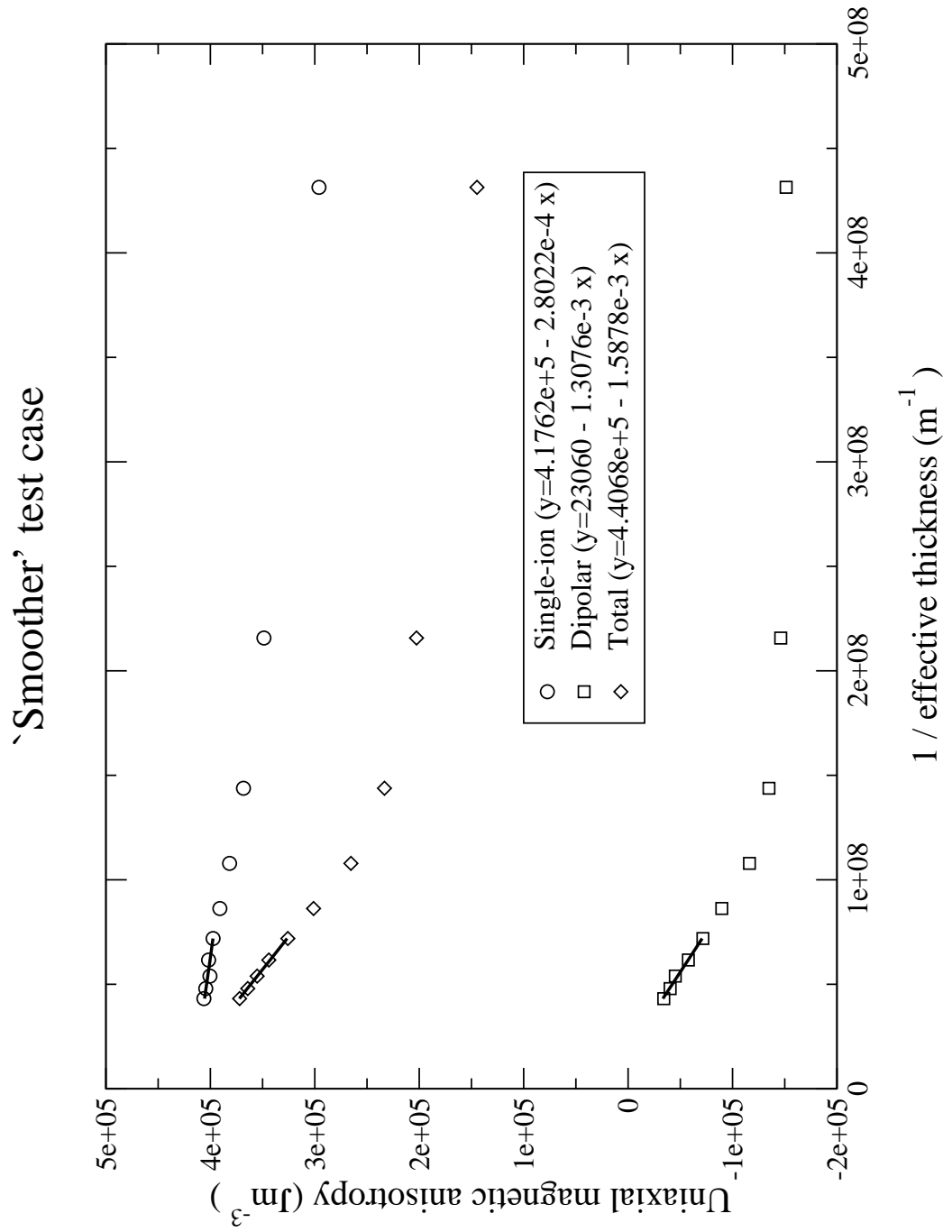


Figure 9.24: Surface and volume anisotropies for 'smoother' test case

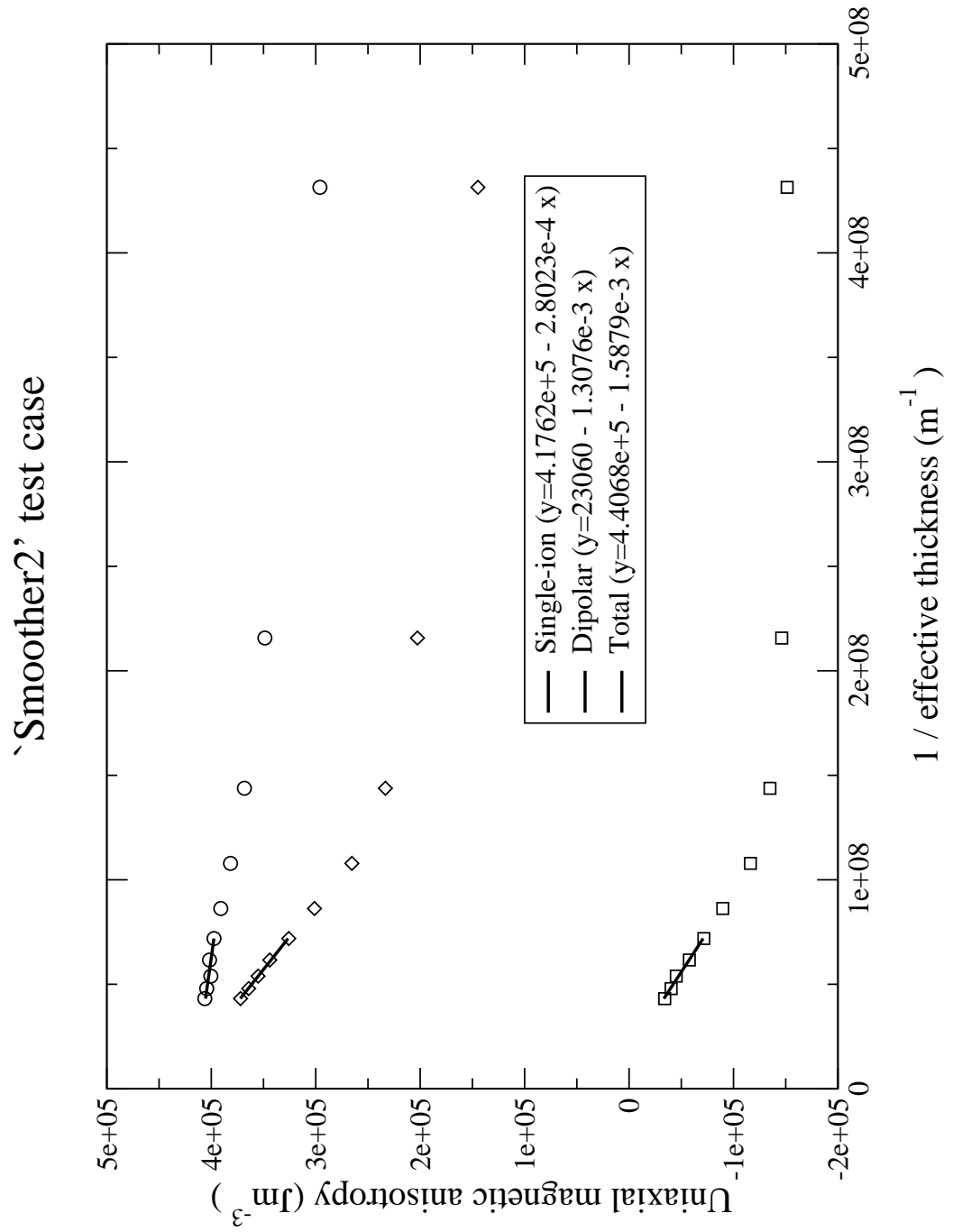


Figure 9.25: Surface and volume anisotropies for 'smoother2' test case

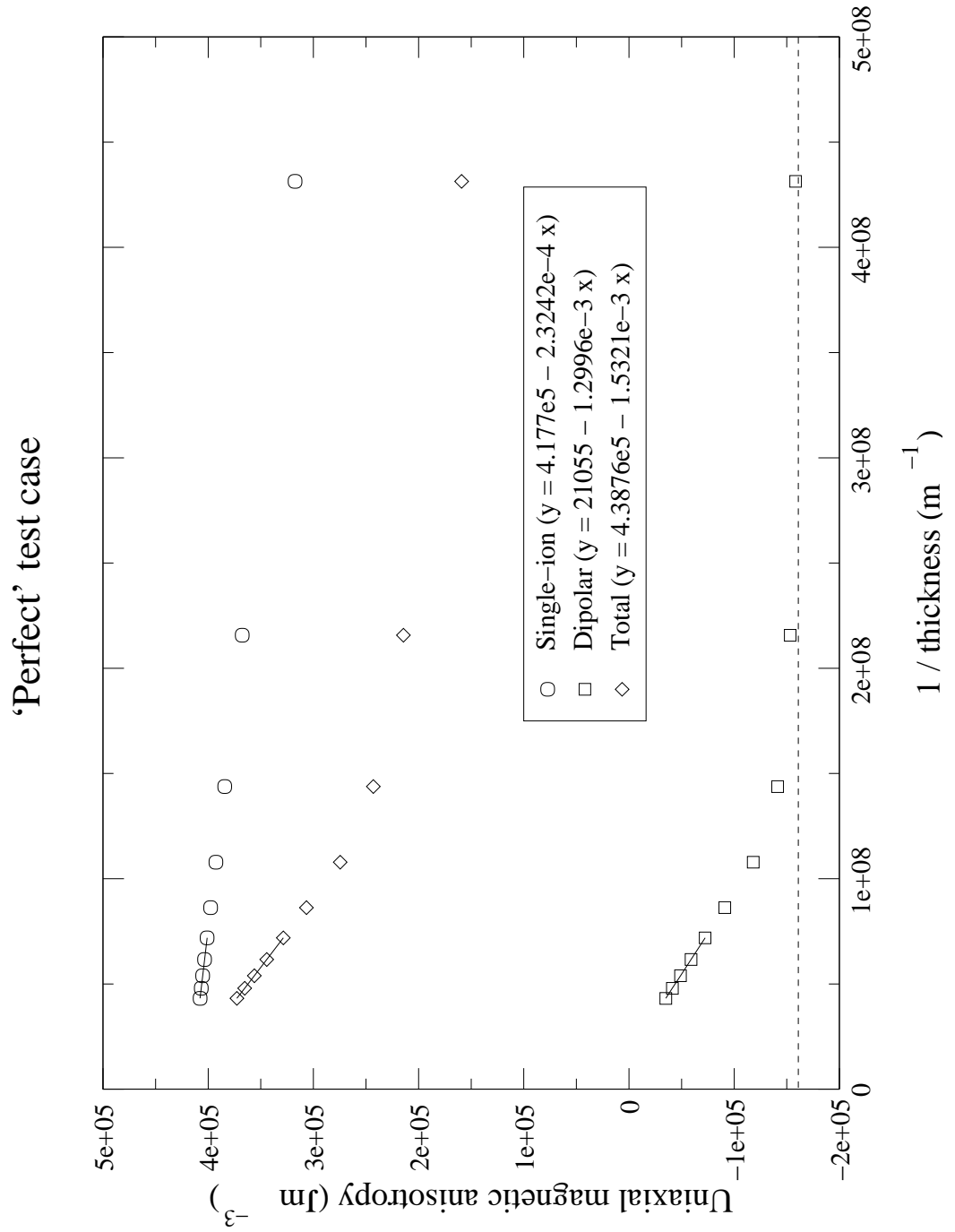


Figure 9.26: Surface and volume anisotropies for ‘perfect’ test case

	Single-ion contribution to surface anisotropy
Granular case	-19.41
	-22.23
Smoother case	-14.01
	-14.01
Perfect case	-11.62

Table 9.5: Extrapolated values for  $1/(\text{thickness}) \rightarrow 0$  of the single-ion contribution to the surface anisotropy for the three test cases in units of  $10^{-5} \text{ Jm}^{-2}$

## 10 Discussion of results

The main results of the calculations described in Section 9 have been summarized in Table 10.1. The results of the preliminary investigation into the effect of the detailed structure of the surface on the magnetic anisotropy carried out for the ‘patterned’ films indicated that different surface structures can be associated with substantially different magnetic anisotropies. This conclusion is borne out in the investigation of the magnetic anisotropy of the simulated grown thin films. It can be seen from Table 10.1 that the single-ion contribution to the volume anisotropy decreases with increasing disorder in the film - this can be attributed to the presence of voids in a disordered growing film. As the number of voids increases, the number of magnetic ions with missing ligands will also increase, so accounting for the decreased single-ion contribution. Similarly, the dipolar contribution to the anisotropy decreases dramatically with increasing disorder, as the perfect hexagonal crystal symmetry is broken by the large number of voids and the rough film surface.

The surface anisotropy associated with the single-ion contribution was seen to increase by a factor of 50 - 100 % from a perfectly flat film to a film with a rough surface. The significant effect of having different types of Fe ion site on the film surface has also been demonstrated - the surface anisotropies calculated for two situations of having 12k and 2b sites on the surface differ not only by an order of magnitude, but also by a change of sign.

The novel film growth model described in this thesis, although unable to replicate columnar growth so far, showed formations of monolayer-thick

	Single-ion volume anisotropy ( $\times 10^5 \text{ Jm}^{-3}$ )	Single-ion surface anisotropy ( $\times 10^{-5} \text{ Jm}^{-2}$ )	Dipolar anisotropy ( $\times 10^5 \text{ Jm}^{-3}$ )	Total: single-ion plus dipolar anisotropy ( $\times 10^5 \text{ Jm}^{-3}$ )
Bulk perfect	4.177	-	0.174	4.351
crystal	3.800 <sup>a</sup>	-	0.176	3.976
Infinite perfect		+1.893 <sup>b</sup>		
film	4.180	-11.59 <sup>c</sup>	-1.60	2.580
		-17.50 <sup>d</sup>		
Finite perfect	3.200 <sup>e</sup>	-	-1.410	1.790
crystal	4.180 <sup>f</sup>	-	+0.030	4.210
Simulated	3.586	-19.41	0.069	3.655
granular film	3.617	-22.23	0.047	3.664
Simulated	4.176	-14.01	0.231	4.407
smoother film	4.176	-14.01	0.231	4.407
Simulated	4.177	-11.62	0.211	4.388
perfect film				

<sup>a</sup>Bipyramidal Fe cations in 4e position

<sup>b</sup>Fe cations in 2b positions on the film surface

<sup>c</sup>Fe cations in 2a positions on the film surface

<sup>d</sup>Fe cations in 12k positions on the film surface

<sup>e</sup>Single layer thick film

<sup>f</sup>14-layer thick film

Table 10.1: Summary of *ab initio* calculated anisotropy contributions for perfect and simulated grown films of  $\text{BaFe}_{12}\text{O}_{19}$  at  $T=0\text{K}$ . Unless otherwise indicated, the results are shown for the bipyramidal Fe cations being in the 2b positions and the 12k sites on the corners of the unit cell.

‘platelets’ on a scale of nanometres. This is in reasonable agreement with AFM pictures of experimentally grown barium hexaferrite thin films [27, 99]. In any case, [100] seems to suggest that polycrystalline and columnar growth structures develop on longer length and time scales than the program is currently capable of handling in a reasonable time (the largest system which could have been investigated was  $0.1\mu m \times 0.1\mu m$ ). The model might possibly exhibit these features if large enough systems and long enough timescales could be investigated. A more detailed investigation of the statistical properties of the growth model might reveal regions in the phase space of process parameters which can be identified as corresponding to known experimental microstructures. A more detailed comparison with AFM experiments would be useful, particularly with regard to determination of surface diffusion rates. The model cannot fully replicate the observed microstructure, which is determined by the presence of screw dislocations (on more mismatched substrates) [27], but would perform better for substrates which give a smaller lattice mismatch.

The magnetic model used in these studies has also been demonstrated to provide excellent results. Uniaxial contributions of single-ion anisotropy to the total anisotropy were obtained by ab initio calculations for bulk material and various forms of thin films of barium hexaferrite. The results achieved are in good agreement with values determined by experiment [1, 51]. An expansion of the program to quantify cubic contributions might be possible. Modelling partial occupancies and missing ligands using the ‘mean-field’ model seems to give dependences of anisotropy on the presence of surfaces

and vacancies that are broadly in line with physical intuition. The influence of surface roughness on both single-ion and dipolar contributions to the anisotropy has been demonstrated, and we can supplement and confirm the conclusions, of e.g. [101], that dipolar contributions are as important on surfaces as contributions from other sources. Surface anisotropy contributions associated with different sublattices were quantified, and the unusual surface behaviour of bipyramidal sites was demonstrated. Also, the feasibility of performing an explicit dipolar summation to evaluate the dipolar contribution to the total anisotropy was demonstrated, and the method was demonstrated to give results consistent with experiment and macroscopic theory both in the bulk material and for thin films. The method may not be as good as Fourier- or Ewald summation-based methods for systems with periodicity e.g. [102], but it seems to be just as good as any other technique for non-periodic systems (e.g. isolated clusters). Two different computational strategies for the explicit summation were investigated and compared - the ‘high-memory’ strategy, in which the positions of all of the interacting ions are computed once and stored until needed, was demonstrated to be more efficient for calculating the dipolar contributions. This was in contrast to the single-ion contributions, for which the alternative ‘low-memory’ strategy was substantially more efficient.

## 11 Conclusions

This work has demonstrated the *ab initio* calculation of the magnetic anisotropy of the prototype M-type ferrite  $\text{BaFe}_{12}\text{O}_{19}$  in its bulk form and also in the form of thin films. The magnetic model has been applied both to perfect crystalline thin films, and also simulated grown films created using a novel growth model and an efficient Monte Carlo numerical technique. The effect of processing conditions on the structure of the grown film has been quantified and described, along with the resulting effects on the magnetic properties of the simulated film.

The ‘tailoring’ of the magnetic properties of thin films in a precise and reproducible manner is currently of great interest to the magnetic recording industry, and will increase in importance as the quest for ever-higher recording densities continues. Significant progress has recently been made in decreasing the time taken to change the magnetic state of a recorded domain [103, 104], which will allow higher data transfer rates, but the ability to accurately predict the effect of film structure on magnetic properties on nanometre scales will also be crucial for the future of the industry. This work contributes to that theoretical effort by demonstrating techniques for the calculation of volume and surface contributions to the magnetic anisotropy of simulated PLD deposited continuous thin films, but is also equally applicable to calculations of the properties of ‘patterned’ recording media [105], which show great potential for very high density magnetic recording.

## 11.1 Original achievements and developments in this thesis

- The development, implementation and partial characterisation of a novel ‘off-lattice’ Monte-Carlo growth model for the simulation of deposition of thin films of hexagonal materials, with provision for voids and interfacial strain energies.
- The development of a computer program to calculate the single-ion and dipolar contributions to the uniaxial anisotropy of an arbitrary assembly of identical magnetic ions in a variety of different local environments, with provision for infinite systems (using 2-D and 3-D periodic boundary conditions) and isolated clusters.
- The application of the above programs to the simulation of thin films of M-type hexaferrites, in particular a quantitative ab initio study of the relative magnitudes of the surface and volume contributions to the overall uniaxial anisotropy, and an investigation of the effects of film microstructure and roughness on the former.
- Obtaining for the first time values of volume and surface anisotropies of perfect and simulated barium hexaferrite films by ab initio calculations.

## 11.2 Suggestions for further work

- The novel growth model described in this thesis requires further investigation and refinement. In particular, the model needs to be run for larger systems and have more extensive study of ‘annealing’ behaviour, along with a thorough mapping of the dependence of simulated film structure on the model parameters.
- A theoretical determination of spin Hamiltonian parameters could be accomplished by comparing the total energies produced by an *ab initio* electron-structure code (taking into account spin and the effects of spin-orbit coupling) when the atomic moments are in turn parallel and perpendicular to the c-axis, but a method of distinguishing between contributions from different sublattices would be needed. The energy difference calculated in this way would probably not be very accurate, since it would represent a difference of two large and near-identical numbers.

The QTAIM theory (Quantum theory of Atoms in Molecules) due to Bader [106] might provide the answer to both of these difficulties. Based on the topology of the electron density, QTAIM provides a quantum-mechanically consistent scheme for defining the spatial boundaries of an atom within a molecule or crystal, the boundary being defined as the union of surfaces of zero electron flux surrounding each atom (so-called ‘interatomic surfaces’). The total energy of a *single* given atom or ion can then be calculated as a volume integral, evaluated over the region

enclosed by the boundaries. Given QTAIM and sufficiently good spin-dependent wavefunctions from an electron-structure code, the above scheme for evaluation on a site-by-site basis of the single-ion anisotropy contributions may well be feasible.

## References

- [1] H. Kojima. Fundamental properties of hexagonal ferrites with magnetoplumbite structure. In E.P. Wohlfarth, editor, *Ferromagnetic Materials*, volume 3, chapter 5, pages 305–391. North-Holland, 1982.
- [2] David Jiles. *Introduction to Magnetism and Magnetic Materials*. Chapman and Hall, 1991.
- [3] J. Smit and H.P.J. Wijn. *Ferrites*. Wiley, New York, 1959.
- [4] P. Novak. Superposition model analysis on the magnetocrystalline anisotropy of Ba-ferrite. *Czech J. Phys.*, 44(6):603–611, 1994.
- [5] Valdemar Poulsen. The telegraphone: A magnetic speech recorder. *The Electrician*, 1900. (See <http://histv2.free.fr/pls/poulsen2.htm>).
- [6] M.H. Kryder. Magnetic information storage. In R. Gerber, C.D. Wright, and G. Asti, editors, *Applied Magnetism*, volume 253 of *NATO ASI Series E: Applied Sciences*, chapter 2, pages 39–112. Kluwer Academic Publishers, Dordrecht, Netherlands, 1994.
- [7] S. Iwasaki and Y. Nakamura. *IEEE Trans. Magn.*, MAG-13:1272, 1977.
- [8] Kazuhiro Ouchi. Properties, preparation, advances and limitations of materials and media for perpendicular recording. *IEEE Transactions on Magnetism*, 26(1):24–29, 1990.
- [9] Yoshihisa Nakamura. Perpendicular magnetic recording - progress and prospects. *J. Mag. Magn. Mater.*, 200:634–648, 1999.

- [10] K. Ouchi and N. Honda. Overview of latest work on perpendicular recording media. *IEEE Trans. Magn.*, 36(1):16–22, 2000.
- [11] C.P. Bean and J.D. Livingston. Superparamagnetism. *J. Appl. Phys.*, 30:S120–9, 1959.
- [12] Jian-Gang Zhu and H. Neal Bertram. Study of noise sources in thin film media. *IEEE Trans. Magn.*, 26(5):2140–2142, 1990.
- [13] Jian-Gang Zhu. Micromagnetic modelling of thin film recording media. In T.C. Arnoldussen and L.L. Nunnally, editors, *Noise in digital recording*. World Scientific, 1992.
- [14] Michael Alex, Tadashi Yogi, Ian L. Sanders, and K. O’Grady. Interaction effects in film media with varying out-of-plane orientation. *IEEE Trans. Magn.*, 28(5):3264–3266, 1992.
- [15] Jim J. Miles, Michal Wdowin, John Oakley, and Barry K. Middleton. The effect of cluster size on thin film media noise. *IEEE Trans. Magn.*, 31(2):1013–1024, 1995.
- [16] Y. Kitamoto, F. Zhang, S. Kantake, F. Shirasaki, M. Abe, and M. Naoe. Intergranular coupling and activation volume of Co-Ni ferrite thin films with high coercivity above 3kOe. *IEEE Trans. Magn.*, 35(5):2694–2696, 1999.
- [17] S.J. Greaves, H. Muraoka, Y. Sugita, and Y. Nakamura. Intergranular exchange pinning effects in perpendicular recording media. *IEEE Trans. Magn.*, 35(5(2)):3772–3774, 1999.

- [18] T. Fujiwara. Barium ferrite media for perpendicular recording. *IEEE Trans. Magn.*, 21(5):1480–1485, 1985.
- [19] A. Morisako, M. Matsumoto, and M. Naoe. Ba-ferrite thin-film rigid disk for high-density perpendicular magnetic recording. *IEEE Trans. Magn.*, 22(5):1146–1148, 1986.
- [20] A. Morisako, M. Matsumoto, and M. Naoe. Sputtered hexagonal Ba-ferrite films for high-density magnetic recording media. *J. Appl. Phys.*, 79(8 (Part 2A)):4881–4883, 1996.
- [21] X.Y. Sui, M. Scherge, M.H. Kryder, J.E. Snyder, V.G. Harris, and N.C. Koon. Barium ferrite thin-film recording media. *J. Mag. Magn. Mater.*, 155((1-3)):132–139, 1996.
- [22] Yang-Ki Hong. Barium ferrite - an alternative to cobalt-based thin films. *Data Storage Magazine*, 5(10), 1998.
- [23] H.M. Smith and A.F. Turner. Vacuum deposited thin films using a ruby laser. *Appl. Optics*, 4:147, 1965.
- [24] J.T. Cheung and H. Sankur. *CRC Critical Review of Solid State Materials Science*, 15:63, 1989.
- [25] Hugh J. Masterson. *Pulsed Laser Deposition, Structure and Magneto-optical Characterisation of Ferrite, and  $Zn_{1-x}Mn_xTe$  Thin Films*. PhD thesis, Department of Pure and Applied Physics, Trinity College, University of Dublin, 1994.

- [26] P. Papakonstantinou. *Magnetic, Optical and Magneto-Optical Properties of Co/Ti Substituted Barium Hexaferrite*. PhD thesis, Department of Pure and Applied Physics, The Queen's University of Belfast, 1994.
- [27] P. Papakonstantinou, M. O'Neill, R. Atkinson, I.W. Salter, and R. Gerber. Substrate temperature and oxygen pressure dependence of pulsed laser-deposited Sr ferrite films. *J. Magnetism Magnetic Materials*, 152:401–410, 1996.
- [28] C.A. Carosella, D.B. Chrisey, P. Lubitz, J.S. Horwitz, P. Dorsey, R. Seed, and C. Vittoria. Pulsed laser deposition of epitaxial BaFe<sub>12</sub>O<sub>19</sub> thin films. *J. Appl. Phys.*, 71(10):5107–5110, 1992.
- [29] P.A. Gago-Sandoval, R. Carey, D.M. Newman, and B.W.J. Thomas. A comparative study of processes for the production of structured barium ferrite films. *IEEE Trans. Magn.*, 30(6):4824–4826, 1994.
- [30] A. Lisfi, M. Guyot, R. Krishnan, M. Porte, P. Rougier, and V. Cagan. Microstructure and magnetic properties of spinel and hexagonal ferrimagnetic films prepared by pulsed laser deposition. *J. Magnetism Magnetic Materials*, 157/158:258–259, 1996.
- [31] S.R. Shinde, S.E. Lofland, C.S. Ganpule, S.B. Ogale, S.M. Bhagat, T. Venkatesan, and R. Ramesh. Realization of epitaxial barium ferrite films of high crystalline quality with small resonance losses. *J. Appl. Phys.*, 85(10):7459–7466, 1999.

- [32] H.C. Fang, C.K. Ong, S.Y. Xu, K.L. Tan, S.L. Lim, Y Li, and J.M. Liu. Epitaxy barium ferrite thin films on LiTaO<sub>3</sub> substrate. *J. Appl. Phys.*, 86(4):2191–2195, 1999.
- [33] M.E. Koleva, S. Zotova, P.A. Atanasov, R. I. Tomov, C. Ritoscu, V. Nelea, C. Chiritescu, E. Gyorgy, C. Ghica, and I.N. Mihailescu. Sr-ferrite grown on sapphire by pulsed laser deposition. *Appl. Surf. Sci.*, 168:108–113, 2000.
- [34] D.J. Craik. *Magnetism: Principles and Applications*. John Wiley, New York, 1995.
- [35] Soshin Chikazumi. *Physics of Ferromagnetism*. International Series of Monographs on Physics. Clarendon Press, Oxford, 2nd edition, 1997.
- [36] R.R. Birss and G.J. Keeler. The advantages of using spherical harmonics to analyse data on magnetocrystalline anisotropy and other nonlinear anisotropic properties. *Phys. Status Solidi B*, 64:357 – 366, 1974.
- [37] L. Néel. Surface magnetic anisotropy and orientational superlattices. *J. Physique Radium*, 15:225–239, 1954.
- [38] Y.T. Millev, R. Skomski, and J. Kirschner. Higher-order and next-nearest-neighbour Néel anisotropies. *Physical Review B*, 58(10):6305–6315, 1998.

- [39] Amikam Aharoni. *Introduction to the Theory of Ferromagnetism*. Number 93 in International series of monographs on Physics. Clarendon Press, 1996.
- [40] V. Adelsköld. *Arkiv Kemi. Mineral. Geol. Series A*, 12:1, 1938.
- [41] R.W.G. Wyckoff. *Crystal Structures*, volume 3, page 497. John Wiley, New York, 1965.
- [42] X. Obradors, A. Collomb, M. Pernet, D. Samaras, and J.C. Joubert. X-ray analysis of the structural and dynamic properties of  $\text{BaFe}_{12}\text{O}_{19}$  hexagonal ferrite at room temperature. *J. Sol. State Chem.*, 56:171–181, 1985.
- [43] R. Gerber, Z. Simsa, and L. Jensovsky. A note on the magnetoplumbite crystal structure. *Czech J. Phys.*, 44(10):937–940, 1994.
- [44] V.M. Zhukovsky, O.V. Bushkova, V.M. Zainullina, G.I. Dontsov, L.I. Volosentseva, and A.S. Zhukovskaya. Diffusion transport in hexagonal ferrites with magnetoplumbite structure. *Solid State Ionics*, 119:15–17, 1999.
- [45] E.W. Gorter. *Proc. IEE B*, 104:255 S, 1957.
- [46] E.F. Bertaut, A. Deschamps, and R. Pauthenet. *J. Physique Radium*, 20:404, 1959.
- [47] B.T. Shirk and W.R. Buessem. *J. Appl. Phys.*, 40:1294, 1969.

- [48] G. Albanese, M. Carbicchio, and A. Deriu. Temperature dependence of the sublattice magnetizations in Al- and Ga- substituted M-type hexagonal ferrites. *Phys. Stat. Sol. (a)*, 23:351–358, 1974.
- [49] J. Feng, N. Matsushita, K. Watanabe, S. Nakagawa, and M. Naoe. Al substituted Ba ferrite films with high coercivity and excellent squareness for low noise perpendicular recording layer. *J. Appl. Phys.*, 85(8):6139–6141, 1999.
- [50] T.M. Clark, B.J. Evans, G.K. Thompson, and S. Freeman.  $^{57}\text{Fe}$  Mössbauer spectroscopic investigation of complex magnetic structures in Ga, Sc, and In substituted M-type hexagonal ferrites. *J. Appl. Phys.*, 85(8):5229–5230, 1999.
- [51] R. Gerber, T. Reid, R. Atkinson, P. Papakonstantinou, J. Simsova, M. Cernansky, R. Gemperle, K. Jurek, and V. Studnicka. Structural and magnetic properties of  $\text{BaCo}_x\text{Ti}_y\text{Fe}_{12-x-y}\text{O}_{19}$  films. *J. Magnetism Magnetic Materials*, 157/158:295–296, 1996.
- [52] Z. Šimša, S. Lego, R. Gerber, and E. Pollert. Cation distribution in Co-Ti-substituted barium hexaferrites: A consistent model. *J. Magnetism Magnetic Materials*, 140-144:2103–2104, 1995.
- [53] Z. Šimša, R. Gerber, R. Atkinson, and P. Papakonstantinou. Magnetic properties and cation distribution in Co- and Ti-substituted barium hexaferrite single crystals. In *Ferrites: Proceedings of the Sixth Inter-*

*national Conference on Ferrites (ICF 6)*, pages 730–733. The Japan Society of Powder and Powder Metallurgy, 1992.

- [54] M.V. Rane, D. Bahadur, and C.M. Srivastava. Fourier transform-infrared studies of non-stoichiometric Ni-Zr substituted barium ferrite. *J. Phys. D: Appl. Phys.*, 32:2001–2005, 1999.
- [55] E. Brando, H. Vincent, J.L. Soubeyroux, and P. Wolfers. Magnetic properties, X-ray and neutron diffraction analysis of new M-hexaferrites  $\text{BaFe}_{12-2x}\text{Ir}_x\text{Me}_x\text{O}_{19}$  (Me = Co, Zn). *J. Magnetism Magnetic Materials*, 157/158:465–466, 1996.
- [56] W. Heisenberg. Zur theorie des ferromagnetismus. *Zeitschr. f. Physik*, 49:619 – 636, 1928.
- [57] G. Winkler. *Magnetic Garnets*, volume 5 of *Vieweg tracts in pure and applied physics*. Braunschweig/Weisbaden, 1981.
- [58] J. Kanamori. Anisotropy and magnetostriction of ferromagnetic and antiferromagnetic materials. In G.T. Rado and H. Suhl, editors, *Magnetism*, volume 1, page 127. Academic Press, New York, London, 1963.
- [59] J.H. Van Vleck. On the anisotropy of cubic ferromagnetic crystals. *Phys. Rev.*, 52:1178–1198, 1937.
- [60] M.V. Eremin and I.I. Antonova. Charge transfer process contribution to the zero-field splitting of the S-state transition ions. *J. Phys.: Condens. Matter*, 10:5567–5575, 1998.

- [61] A. Abragam and B. Bleaney. *Electron Paramagnetic Resonance of Transition Ions*. Clarendon Press, 1970.
- [62] P. Novak and I. Veltrusky. *Phys. Stat. Solidii B*, 73:575, 1976.
- [63] W.L. Yu and C. Rudowicz. Comprehensive approach to the zero-field splitting of  ${}^6\text{S}$ -state ions -  $\text{Mn}^{2+}$  and  $\text{Fe}^{3+}$  in fluoroperovskites. *Phys. Rev. B*, 45(17):9736 – 9748, 1992.
- [64] Nobuko Fuchikami. Magnetic anisotropy of magnetoplumbite  $\text{BaFe}_{12}\text{O}_{19}$ . *J. Phys. Soc. Jap.*, 20(5):760–769, 1965.
- [65] J.H. Van Vleck. *Phys. Rev.*, 57(426), 1950.
- [66] M.H.L. Pryce. *Proc. Roy. Soc. A*, 63:25, 1950.
- [67] C. Rudowicz. Transformation relations for the conventional  $O_k^q$  and normalised  $O_k'^q$  Stevens operator equivalents with  $k=1$  to 6 and  $-k \leq q \leq k$ . *J. Phys. C: Solid State Physics*, 18(7):1415 – 1430, 1985.
- [68] C. Rudowicz. *J. Phys. C: Solid State Physics*, 18:3837, 1985. (erratum).
- [69] Czesław Rudowicz. Concept of Spin Hamiltonian, forms of zero field splitting and electronic Zeeman hamiltonians and relations between parameters used in EPR: A critical review. *Magnetic Resonance Review*, 13:1–89, 1987.
- [70] C. Rudowicz and S.B. Madhu. Orthorhombic standardization of Spin-Hamiltonian parameters for transition-metal centres in various crystals. *J. Phys.: Condens. Matter*, 11:273–287, 1999.

- [71] C. Rudowicz. On the relations between the zero-field splitting parameters in the extended Stevens operator notation and the conventional ones used in EMR for orthorhombic and lower symmetry. *J. Phys.: Condens. Matter*, 12:L417–L423, 2000.
- [72] W.P. Wolf. Effect of crystalline electric fields on ferromagnetic anisotropy. *Phys. Rev.*, 108(5):1152–1157, 1957.
- [73] D.J. Newman. Interpretation of S-state ion EPR spectra. *Adv. Phys.*, 24:793–843, 1975.
- [74] D.J. Newman and Betty Ng. The superposition model of crystal fields. *Rep. Prog. Phys.*, 52:699–763, 1989.
- [75] P. Novak and L. Vosika. Superposition model for zero-field splitting of  $\text{Fe}^{3+}$  and  $\text{Mn}^{2+}$  ions in garnets. *Czech J. Phys. B*, 33:1134–1147, 1983.
- [76] Y.Y. Yeung. *J. Phys. C: Solid State Physics*, 21:2453, 1988.
- [77] H.B.G. Casimir, J. Smit, U. Enz, J.F. Fast, H.P.J. Wijn, E.W. Gorter, A.J.W. Duyvestein, J.D. Fast, and J.J. Jong. Rapport sur quelques recherches dans la domaine du magnétisme aux laboratoires Philips. *Le Journal de Physique et le Radium*, t20:360–373, 1959.
- [78] F.K. Lotgering, P.R. Locher, and R.P. Van Staple. Anisotropy of hexagonal ferrites with M, W and Y structures containing  $\text{Fe}^{3+}$  and  $\text{Fe}^{2+}$ . *J. Phys. Chem. Solids*, 41:481–487, 1980.

- [79] A. Isalgue, X. Obradors, and J. Tejada. Dipolar magnetic anisotropy in some uniaxial hexagonal ferrites. *J. de Physique*, C6(t46):345–348, 1985.
- [80] A. Collomb, O. Abdelkader, A. Isalgue, and J.P. Mignot. Magnetic properties of hexagonal ferrites - BaMg<sub>2</sub>-W and BaCo<sub>2</sub>-W. *Phys. Stat. Sol. (A)*, 97:896–904, 1986.
- [81] G. Litsardakis. Dipolar energy anisotropy in hexagonal ferrites. *Journal de Physique*, 7(C1):341–342, 1997.
- [82] U. Gradmann. Surface magnetism. *Journal of Magnetism and Magnetic Materials*, 100:481–496, 1991.
- [83] P. Poulopoulos and K. Baberschke. Magnetism in thin films. *J. Phys.: Condens. Matter*, 11:9495–9515, 1999.
- [84] John A. Venables. *Introduction to Surface and Thin Film Processes*. Cambridge University Press, Cambridge, 2000. in preparation.
- [85] M. Kardar, G. Parisi, and Y. Zhang. Dynamic scaling of growing interfaces. *Phys. Rev. Lett.*, 56:889, 1986.
- [86] J.D. Weeks, G.H. Gilmer, and K.A. Jackson. Analytic theory of crystal growth. *J. Chem. Phys.*, 65(2):712 – 720, 1976.
- [87] J.D. Weeks and G.H. Gilmer. Dynamics of crystal growth. *Adv. Chem. Phys.*, 40:157 – 227, 1979.

- [88] Andrea C. Levi and Miroslav Kotrla. Theory and simulation of crystal growth. *J. Phys.: Condens. Matter*, 9(2):299–344, 1997.
- [89] P.A. Maksym. Fast Monte Carlo simulation of MBE growth. *Semiconductor Science and Technology*, 3:594–596, 1988.
- [90] James L. Blue, Isabel Beichl, and Francis Sullivan. Faster Monte Carlo simulations. *Phys. Rev. E*, 51(2):R867–R868, 1995.
- [91] G.M. Sheldrick. *SHELX76. Program for Crystal Structure Determination*. University of Cambridge, Cambridge, England, 1976.
- [92] M. Phillips, T. Munzner, and S. Levy. GEOMVIEW. Available by anonymous FTP from geom.umn.edu, 1995. See also the home page of the Geometry Centre at the University of Minnesota.
- [93] P. Novak, K. Idland, A.V. Zalesskij, V.G. Krivenko, and A.V. Kunevitch. Magnons and sublattice magnetizations in hexagonal Ba ferrite. *J. Phys.: Condens. Matter*, 1:8171–8179, 1989.
- [94] Kar W. Yung, P.B. Landecker, and D.D. Villani. An analytical solution for the force between two magnetic dipoles. *J. Mag. Electr. Sep.*, 9:39–52, 1998.
- [95] Harald Brune, G. Steven Bales, Joachim Jacobsen, Corrado Boragno, and Klaus Kern. Measuring surface diffusion from nucleation island densities. *Phys. Rev. B*, 60(8):5991–6006, 1999.

- [96] Martin Prutton. *Introduction to surface physics*, chapter 5, pages 147–151. Oxford University Press, 1994.
- [97] Pavel Šmilauer, Mark R. Wilby, and Dimitri D. Vvedensky. Reentrant layer-by-layer growth: A numerical study. *Phys. Rev. B*, 47(7):4119 – 4122, 1993.
- [98] Pavel Šmilauer and Dimitri D. Vvedensky. Coarsening and slope evolution during unstable epitaxial growth. *Phys. Rev. B*, 52(19):14263–14272, 1995.
- [99] R. Gerber, R. Atkinson, and Z. Šimša. Magnetism and magneto-optics of hexaferrite layers. *J. Mag. Magn. Mater.*, 175:79–89, 1997.
- [100] G.H. Gilmer, Hanchen Huang, and Christopher Roland. Thin film deposition: Fundamentals and modelling. *Computational Materials Science*, 12:354–380, 1998.
- [101] Dora Altbir, Miguel Kiwi, Ricardo Ramirez, and Ivan K. Schuller. Dipolar interaction and its interplay with interface roughness. *J. Magnetism Magnetic Materials*, 149:L246–L250, 1995. Letter to the Editor.
- [102] D.V. Berkov and N.L. Gorn. Numerical simulation of the magnetization structures in thin polycrystalline films with the random anisotropy and intergrain exchange. *J. Appl. Phys.*, 83(11):6350–6352, 1998.
- [103] C.H. Back, R. Allenspach, W. Weber, S.S.P. Parkin, D. Weller, E.L. Garwin, and H.C. Siegmann. Minimum field strength in precessional magnetization reversal. *Science*, 285:864–867, August 1999.

- [104] Y. Acremann, C.H. Back, M. Buess, O. Portmann, A. Vaterlaus, D. Pescia, and H. Melchior. Imaging precessional motion of the magnetization vector. *Science*, 290:492–495, October 2000.
- [105] Jian-Gang Zhu, Xiangdong Lin, Lijie Guan, and William Messner. Recording, noise and servo characteristics of patterned thin film media. *IEEE Trans. Magn.*, 36(1):23–29, 2000.
- [106] Richard F.W. Bader. *Atoms in molecules: a quantum theory*. Number 22 in International Series of Monographs on Chemistry. Clarendon Press, 1990.

## A Crystal structure data for BaM

The following is the crystal structure data for BaM used for the work carried out in this thesis. The format of the file is described in Section 8.2.2.

```
TITLFerrite supercell (partial occupancy)
CELL 0.0000 5.8920 5.8920 23.1830 90.0000 90.0000 120.0000
LATT -1
BA1 0 0.66670 0.33330 0.25000 1.00000 0.00000
BA2 0 0.33330 0.66670 0.75000 1.00000 0.00000
FE1 0 0.00000 0.00000 0.00000 0.12500 5.00000
FE1 0 1.00000 0.00000 0.00000 0.12500 5.00000
FE1 0 0.00000 1.00000 0.00000 0.12500 5.00000
FE1 0 0.00000 0.00000 1.00000 0.12500 5.00000
FE1 0 1.00000 1.00000 0.00000 0.12500 5.00000
FE1 0 1.00000 0.00000 1.00000 0.12500 5.00000
FE1 0 0.00000 1.00000 1.00000 0.12500 5.00000
FE1 0 1.00000 1.00000 1.00000 0.12500 5.00000
FE2 0 0.00000 0.00000 0.25000 0.25000 4.00000
FE2 0 0.00000 1.00000 0.25000 0.25000 4.00000
FE2 0 1.00000 0.00000 0.25000 0.25000 4.00000
FE2 0 1.00000 1.00000 0.25000 0.25000 4.00000
FE3 0 0.00000 0.00000 0.75000 0.25000 4.00000
FE3 0 0.00000 1.00000 0.75000 0.25000 4.00000
FE3 0 1.00000 0.00000 0.75000 0.25000 4.00000
FE3 0 1.00000 1.00000 0.75000 0.25000 4.00000
FE9 0 0.00000 0.00000 0.50000 0.25000 5.00000
FE9 0 0.00000 1.00000 0.50000 0.25000 5.00000
FE9 0 1.00000 0.00000 0.50000 0.25000 5.00000
FE9 0 1.00000 1.00000 0.50000 0.25000 5.00000
FE4 0 0.33330 0.66670 0.02713 1.00000 -3.00000
FE5 0 0.33330 0.66670 0.19030 1.00000 -2.00000
FE6 0 0.16868 0.33734 0.89175 1.00000 1.00000
FE7 0 0.66266 0.83134 0.89175 1.00000 1.00000
FE8 0 0.16866 0.83132 0.89175 1.00000 1.00000
FE10 0 0.66670 0.33330 0.52713 1.00000 -3.00000
FE11 0 0.66670 0.33330 0.69030 1.00000 -2.00000
FE12 0 0.83132 0.66266 0.39175 1.00000 1.00000
FE13 0 0.33734 0.16866 0.39175 1.00000 1.00000
FE14 0 0.83134 0.16868 0.39175 1.00000 1.00000
```

FE15	0	0.66670	0.33330	0.97287	1.00000	-3.00000
FE16	0	0.66670	0.33330	0.80970	1.00000	-2.00000
FE17	0	0.33734	0.16868	0.10825	1.00000	1.00000
FE18	0	0.83134	0.66266	0.10825	1.00000	1.00000
FE19	0	0.83132	0.16866	0.10825	1.00000	1.00000
FE20	0	0.33330	0.66670	0.47287	1.00000	-3.00000
FE21	0	0.33330	0.66670	0.30970	1.00000	-2.00000
FE22	0	0.66266	0.83132	0.60825	1.00000	1.00000
FE23	0	0.16866	0.33734	0.60825	1.00000	1.00000
FE24	0	0.16868	0.83134	0.60825	1.00000	1.00000
01	0	0.00000	0.00000	0.15094	0.25000	0.00000
01	0	0.00000	1.00000	0.15094	0.25000	0.00000
01	0	1.00000	0.00000	0.15094	0.25000	0.00000
01	0	1.00000	1.00000	0.15094	0.25000	0.00000
012	0	0.00000	0.00000	0.65094	0.25000	0.00000
012	0	0.00000	1.00000	0.65094	0.25000	0.00000
012	0	1.00000	0.00000	0.65094	0.25000	0.00000
012	0	1.00000	1.00000	0.65094	0.25000	0.00000
023	0	0.00000	0.00000	0.84906	0.25000	0.00000
023	0	0.00000	1.00000	0.84906	0.25000	0.00000
023	0	1.00000	0.00000	0.84906	0.25000	0.00000
023	0	1.00000	1.00000	0.84906	0.25000	0.00000
031	0	0.00000	0.00000	0.34906	0.25000	0.00000
031	0	0.00000	1.00000	0.34906	0.25000	0.00000
031	0	1.00000	0.00000	0.34906	0.25000	0.00000
031	0	1.00000	1.00000	0.34906	0.25000	0.00000
02	0	0.33330	0.66670	0.94546	1.00000	0.00000
03	0	0.18213	0.36426	0.25000	1.00000	0.00000
04	0	0.15647	0.31294	0.05192	1.00000	0.00000
05	0	0.50260	0.00520	0.14957	1.00000	0.00000
06	0	0.63574	0.81787	0.25000	1.00000	0.00000
07	0	0.68706	0.84353	0.05192	1.00000	0.00000
08	0	-0.00520	0.49740	0.14957	1.00000	0.00000
09	0	0.18213	0.81787	0.25000	1.00000	0.00000
010	0	0.15647	0.84353	0.05192	1.00000	0.00000
011	0	0.50260	0.49740	0.14957	1.00000	0.00000
013	0	0.66670	0.33330	0.44546	1.00000	0.00000
014	0	0.81787	0.63574	0.75000	1.00000	0.00000
015	0	0.84353	0.68706	0.55192	1.00000	0.00000
016	0	0.49740	-0.00520	0.64957	1.00000	0.00000
017	0	0.36426	0.18213	0.75000	1.00000	0.00000

018	0	0.31294	0.15647	0.55192	1.00000	0.00000
019	0	0.00520	0.50260	0.64957	1.00000	0.00000
020	0	0.81787	0.18213	0.75000	1.00000	0.00000
021	0	0.84353	0.15647	0.55192	1.00000	0.00000
022	0	0.49740	0.50260	0.64957	1.00000	0.00000
024	0	0.66670	0.33330	0.05454	1.00000	0.00000
025	0	0.31294	0.15647	0.94808	1.00000	0.00000
026	0	0.00520	0.50260	0.85043	1.00000	0.00000
027	0	0.84353	0.68706	0.94808	1.00000	0.00000
028	0	0.49740	-0.00520	0.85043	1.00000	0.00000
029	0	0.84353	0.15647	0.94808	1.00000	0.00000
030	0	0.49740	0.50260	0.85043	1.00000	0.00000
032	0	0.33330	0.66670	0.55454	1.00000	0.00000
033	0	0.68706	0.84353	0.44808	1.00000	0.00000
034	0	-0.00520	0.49740	0.35043	1.00000	0.00000
035	0	0.15647	0.31294	0.44808	1.00000	0.00000
036	0	0.50260	0.00520	0.35043	1.00000	0.00000
037	0	0.15647	0.84353	0.44808	1.00000	0.00000
038	0	0.50260	0.49740	0.35043	1.00000	0.00000

END

## **B Presentations and publications arising from this work**

- Poster at Condensed Matter and Materials Physics conference, Exeter, Dec 1997
- Presentation at visit of the Chair of the Magnetism Committee, Physics Department, Salford University
- A paper describing the novel growth model, and another on the investigation of the magnetic properties of the simulated grown films, are in preparation.

## C Pseudocode for DEPOSIT program

```
PROGRAM Deposit
{
  Declare variables.
  Initialize variables.
  Show introductory screen.
  Ask user for input and output film files, and
  open them for processing.
  Read input film file (RFILM).
  Ask user for process parameters.
  Build data structures for input data
  {
    Build group membership tables.
    Build black/red grid arrays.
  }
  Precalculate exponentials for efficiency.
  Build neighbour and hop rate arrays.
  Initialize process clock and set process start
  and end times.
  Initialize the PRNG (user choice of options).

  MAIN EVENT LOOP (until process end time reached)
  {
    Update cumulative hopping frequency tables.
    Build total cumulative process rate table.
    Advance clock and choose next event.
    If event chosen is a deposition
    {
      Increment deposition event counter.
      Add new unit to randomly-chosen group.
      Choose location (x,y) of landing point.
      Drop unit into simulation cell to give
      temporary landing point.
      Implement transient mobility.
      {
        Find adjacent unoccupied sites in
        this layer.
        Of these, find which have an unoccupied
        site underneath.
        Choose between these lower sites,
        exponentially favouring those with larger
```

```

        numbers of neighbouring units.
    }
}
otherwise event is a hop
{
    Increment hop event counter.
    Choose which group and unit are affected.
    Make a list of chosen unit's neighbours.
    Wipe current grid location of unit.
    Make a list of available adjacent positions.
    If any positions on this list have unoccupied
    sites underneath, make a list of those instead.
    Choose between sites on the current list,
    exponentially favouring those with larger
    numbers of neighbouring units.
}
Choose a tail position for the current unit.
Place unit in black/red grid arrays.
Update hopping probabilities for all units
in film.
If backup interval has been reached, write
checkpoint file and output current
film statistics.
}
END OF MAIN EVENT LOOP
Calculate film statistics.
Write out output film file and show
run-time statistics.
END OF PROGRAM

```

## D Pseudocode for KFILM program

```
PROGRAM Kfilm
{
  Declare variables
  Initialize variables
  Create intro screen
  Ask user for input film data file and read it
  Build film data structures
  Ask user for input unit cell data file and read it
  Show summary of unit cell data

  If this is a high-memory version of the program
  {
    Build master Fe and O position and occupation number arrays
    for entire film.
  }

  CALCULATE THE SINGLE-ION ANISOTROPY CONTRIBUTION
  {
    If this is the high-memory version of the program
    {
      Declare and initialize local variables
      Ask user for single-ion parameter file and open it
      Ask user to choose verbosity of output
      Loop over all the Fe ions in the simulation cell, whose
      positions and occupancies have been precalculated
      {
        Find this ion's closest O neighbours (i.e. ligands)
        Loop over this ion's ligands
        {
          Calculate the geometric term for this ligand
          Depending on the type of ligand, calculate the
          intrinsic term.
          Calculate the overall SI contribution of this
          ligand, weighted by the occupancies of both the Fe
          and O ions and add this to the ion's total SI
          contribution.
        }
        Add this ion's overall SI contribution to the running
        total for the film.
      }
    }
  }
}
```

```

    }
    Write out the total single-ion anisotropy for the whole
    film, along with a breakdown of the total by site type.
  }
  OTHERWISE this is the LOW-MEMORY version of the program
  {
    Declare and initialize local variables
    Ask user for single-ion parameter file and open it
    Ask user to choose verbosity of output
    Loop over all the growth units in the simulation cell
    {
      Loop over all the Fe ions in this simulation cell
      {
        Work out this ion's position and occupation number
        Work out the positions and occupation numbers of all
        possible O neighbours
        Find this ion's closest O neighbours (i.e. ligands)
        Loop over this ion's ligands
        {
          Calculate the geometric term for this ligand
          Depending on the type of ligand, calculate the
          intrinsic term
          Calculate the overall SI contribution of this
          ligand, weighted by the occupancies of both the
          Fe and O ions and add this to the ion's total SI
          contribution.
        }
        Add this ion's overall SI contribution to the
        running total for the film.
      }
    }
    Write out the total single-ion anisotropy for the whole
    film, along with a breakdown of the total by site type.
  }
}

```

#### CALCULATE THE DIPOLAR ANISOTROPY CONTRIBUTION

```

{
  If this is the high-memory version of the program
  {
    Declare and initialize local variables.
    Ask user for cutoff radius.
  }
}

```

```

If user wants to impose additional x,y,or z cutoffs, ask
for numerical maximum and minimum values.
Loop over all Fe ions in the film
{
  Loop over all other Fe ions in the film
  {
    Find all the periodic copies of this second Fe ion
    which lie within the cutoff radius and the
    additional x,y,z cutoffs (if any).
    Calculate the dipolar contribution from this second
    Fe ion AND all of its periodic copies, weighted by
    the occupancies of each ion.
  }
  Calculate the overall dipolar contribution from
  this Fe ion.
}
Calculate and display the total dipolar anisotropy for the
whole film, and also a breakdown by fractions of the
requested cutoff radius.

}
OTHERWISE this is the LOW-MEMORY version of the program
{
  Declare and initialize local variables
  Ask user for cutoff radius
  If user wants to impose additional x,y,or z cutoffs,
  ask for numerical maximum and minimum values.
  Loop over all the growth units in the simulation cell
  {
    Loop over all the Fe ions in this simulation cell
    {
      Work out this Fe ion's position and occupation
      number.
      Loop over all the growth units in the
      simulation cell.
      {
        Loop over all the Fe ions in this simulation cell
        {
          Work out this second Fe ion's position and
          occupancy.
          Find all the periodic copies of this second Fe
          ion which lie within the cutoff radius and the
          additional x,y,z cutoffs (if any).
        }
      }
    }
  }
}

```

```
        Calculate the dipolar contribution from this
        second Fe ion AND all of its periodic copies,
        weighted by the occupancies of each ion.
    }
}
    Calculate the overall dipolar contribution from
    this Fe ion.
}
}
    Calculate and display the total dipolar anisotropy for the
    whole film, and also a breakdown by fractions of the
    requested cutoff radius.
}
}
    Write out total calculated anisotropy for this film.
}
END OF PROGRAM
```